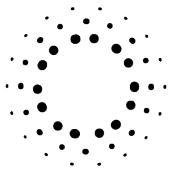

IFT - UNESP
INSTITUTO DE FÍSICA TEÓRICA

M. Sc. Thesis IFT–D.004/2022

Charged Particle Tracking Applied to a Search for Dark Matter in Collider Experiments

João Paulo de Souza Böger

Advisor

Thiago Rafael Fernandez Perez Tomei

Março de 2022

Böger, João Paulo de Souza
B674c Charged particle tracking applied to a search for dark matter in collider experiments / João Paulo de Souza Böger. – São Paulo, 2022
123 f.

Dissertação (mestrado) – Universidade Estadual Paulista (Unesp), Instituto de Física Teórica (IFT), São Paulo
Orientador: Thiago Rafael Fernandez Perez Tomei

1. Matéria escura (Astronomia). 2. Partículas (Física nuclear). 3. Aceleradores de partículas. I. Título

Sistema de geração automática de fichas catalográficas da Unesp. Biblioteca do Instituto de Física Teórica (IFT), São Paulo. Dados fornecidos pelo autor(a).

Dedico esta dissertação em memória de meu avô João "Catarina" e meu amigo "Quexo", e aos meus pais, Marlene Beckhauser de Souza e Valdair Roveda Böger.

Agradecimentos

Agradeço meus pais, Marlene e Valdair, pelo incentivo, apoio e inspiração que me deram desde sempre e em abundância.

Agradeço também minha irmã Clara pela companhia gentil e pelo belo coração que possui.

Agradeço meus avós (Albertina, Glória, Nida, João, Paulo e Neo), tias, tios, primos e primas por estarem comigo em toda essa trajetória e me ajudarem com tudo que puderam.

Agradeço profusamente minhas amigas e meus amigos que foram esteio nos momentos caudalosos, e fulcrais para as horas serenas: Sanson, Adolfo, Leo, Anthony, Juarez, Amanda, Gauche, Chico, Barbosa, Alisson, Diogo, Sabrina, Franck, Tirelli, Café, Jung, Helo, Valéria, Rhayra, Thiago, Zé, Rômulo, Remus, Ibarra, Igor, Krick, Portilho, Tadeu, Helcio, Greg, Kevin, Hamilton, Muryel, Kill, Calebe, Marina, Caio, Juninho, Marcelo, Mathias, Ricardo, Augusto e Guesser.

Agradeço meu psicoterapeuta Cris, e os músicos, escritores e artistas que me forneceram conforto e acolhimento em suas obras: Mutarelli, Dostoiévski, Bulgákov, Ferréz, Porca Veia, Albino Manique, Luciano Maia, João Gilberto, João Bosco e Yamandu Costa.

Agradeço meu orientador Professor Thiago Rafael Fernandez Perez Tomei por ser exemplo e inspiração profissional e pessoal, me ensinar tanto e apoiar nos conturbados momentos de pandemia.

Agradeço meus colegas de grupo Felipe, Breno, Isabela e Dener pelas discussões e os professores Sérgio, Sandra, Pedro, Eduardo e César por me auxiliarem em todo o projeto.

Agradeço os funcionários e professores do Instituto de Física Teórica (IFT) da Unesp e do Núcleo de Computação Científica (NCC) do IFT por tornarem possível o presente trabalho.

Agradeço o Conselho Nacional de Desenvolvimento Científico e Tecnológico (CNPq) (processo nº 132673/2020-7) e a Fundação de Amparo à Pesquisa do Estado de São Paulo (FAPESP) pelo financiamento desse projeto (processo nº 2020/00244-0), tornando-o viável.

"The All-Powerfull
made some of us out there ***real weirdos****,*
we shan't be shy:
why waste this blessing?"

Francisco Neubauer, *Weirdo's Manifesto*

Resumo

O seguinte projeto apresenta um estudo sobre a reconstrução de traços de partículas carregadas no detector de partículas CMS, localizado no LHC, e a viabilidade de detecção de partículas de matéria escura nesse. Nosso trabalho utiliza o modelo de Partículas Massivas de Interação Tênue (FIMPs), em que uma Partícula de Longa Vida (LLP), F, é predita e se acopla tenuemente a uma partícula carregada do Modelo Padrão (SM) e uma de Matéria Escura s: $F \rightarrow s + \text{SM}$. A partícula F decai no volume do CMS deixando uma assinatura de traço evanescente, isto é, o traço possui *hits* apenas das primeiras camadas do detector, dado que após F decair os produtos do decaimento não possuem energia suficiente, ou sequer interagem, com os elementos do detector. Um algoritmo de reconstrução de traços baseado na técnica de *Kalman Filter Combinatório* foi implementado em um detector simplificado, reconstruindo 40% dos traços de píons ($\pi^{\pm}$) corretamente. Em seguida, uma análise de eventos contendo charginos ($\tilde{\chi}^{\pm}$) como as partículas F do modelo de FIMP, gerados por simulações de Monte Carlo, foi realizada atingindo desempenho de 70% dos traços sendo reconstruídos apropriadamente, sugerindo que assinaturas de traços evanescentes podem ser detectadas no experimento CMS. Os resultados foram comparados e validados com uma análise da colaboração CMS.

Palavras Chaves: Detecção de Traços de Partículas; Matéria Escura; Física Experimental de Altas Energias; Física Além do Modelo Padrão; Aceleradores de Partículas.

Áreas do conhecimento: Física; Física de Partículas; Física de Altas Energias.

Abstract

This project presents the results of a study concerning charged particles tracking in the Compact Muon Solenoid (CMS) of the Large Hadron Collider (LHC) and the feasibility of detection of Dark Matter particles in the experiment. The work considers the Feebly Interacting Massive Particles (FIMPs) model, in which a charged Long-Lived Particle (LLP), F, is predicted to have tiny couplings with a charged Standard Model (SM) particle and a DM particle s: $F \rightarrow s + \text{SM}$. F is a LLP that decays within the CMS' volume, generating a disappearing track signature, a track with hits in the first layers only and no signals in the further subdetectors of CMS, since the decaying products are either too soft or do not interact the detector's material. A Combinatorial Kalman Filter (CKF) tracking reconstruction algorithm was developed within a toy model detector in this work, reconstructing 40% of pion ($\pi^{\pm}$) tracks properly. Then, an analysis of Monte Carlo simulated events containing charginos ($\tilde{\chi}^{\pm}$) as F particles - in the FIMP framework - was performed, reaching 70% of such particles' tracks properly reconstructed, pointing in the direction that disappearing tracks' signatures may be able to be detected in the CMS Experiment. Results were compared and validated with a CMS' tracking performance analysis.

Keywords: Particle Tracking; Dark Matter; Experimental High Energy Physics; Beyond Standard Model Physics; Particle Accelerators.

Knowledge Aread: Physics; Particle Physics; High Energy Physics.

Contents

Chapter 1

Introduction

Throughout the 20th century, the constant interplay between theory and experiment expanded highly the physical understanding of particles and its interactions, mainly within the framework of the Standard Model of particles and fields (SM) [1]. The SM was developed as a local gauge symmetric Quantum Field Theory based on the group $SU(3)_C \times SU(2)_L \times U(1)_Y$, describing the electroweak ($SU(2)_L \times U(1)_Y$) and strong ($SU(3)_C$) interactions. It is a largely tested and successful theory, its fundamental predicted particles were all discovered, the last one being the Higgs boson in 2012.

Although some compelling phenomena are still not explainable [2] by SM fundamental particles and interactions, such as the quantum description of gravity, and the existence of Dark Matter (DM), thought to be a type of matter that does not interact electromagnetically or through the strong force with the SM, but has numerous cosmological and astrophysical evidences [3, 4, 5] of its existence. Estimates of the abundance of DM in the universe reveal that from all the matter present in the universe, almost 85% of it is in the form of DM, however our knowledge concerning its origin and interactions is very incipient.

A hypothesis being considered and developed in the last decades, is that DM is composed of particles that do not interact through SM forces, or interact very weakly, explaining the absence of DM signals through telescopes and observatories so far. Depending on the interactions that could exist between SM particles and DM, particle detectors would detect signals of this new physics through some specific signals, allowing the study of physics Beyond the Standard Model (BSM) in already existing experiments, such as the Large Hadron Collider (LHC). Searches for signals of BSM physics have been conducted in LHC detectors' research groups, constraining many parameters of particle Dark Matter models and arousing new developments in the theoretical particle physics' fields [6].

In order to search for DM in particle colliders, the events are reconstructed in the LHC detectors and signatures of DM particles are searched. This thesis focuses on better understanding how such signatures can be found using the Compact

Muon Solenoid (CMS) detector at the LHC. A crucial aspect to accurate events' reconstruction is its tracking algorithms, responsible for reconstructing charged particles and determining their mass, momentum and energy. Thus, a search for a FIMP signature in the scope of CMS' Tracker System was performed.

In the following three chapters of this work - Chapters 2, 3, 4 -, there is a bibliographic revision of Standard Model, Dark Matter and the CMS Experiment at the LHC, respectively. In Chapter 5 the founding concepts of tracking reconstruction are defined and an implementation of Combinatorial Kalman Filter for charged particles tracks is presented. Finally, in Chapter 6, an analysis of CMS' tracking algorithm, using the software package `CMSSW` is performed. In order to evaluate its performance for FIMP's signatures detection, and the results are then compared with a CMS analysis. Chapter 7 presents the conclusions of this project.

Chapter 2

Standard Model and Particle Physics

Understanding how nature works and through which mechanisms it manifests itself has been a long-standing debate throughout the humanity history. A myriad answers and models were and are elaborated trying to grasp the subtleties that pervade the universe we live in. In the natural sciences' realm, the *Standard Model* of particles and fields (SM) is perhaps one of the most successful theories regarding answering, at least partially, some of these questions.

Through continual interchange and collaboration between theoretical and experimental researchers, the understanding of the origin and interaction of particles was highly developed in the 20th century, culminating in the elaboration of a descriptive model of these with excellent agreement with the experimental data.

Among the main steps given towards the SM model development, three ideas had a profound impact in the area at the time and guided the efforts of the physicists working in the area to construct these experimentally successful theories of interactions and forces between particles [7]. The first can be traced back to Gell-Mann and Zweig, when in 1964 both of them proposed independently the *quark model* [8, 9]. Up until then, it was a common reasoning in the particle physics area that protons, neutrons, mesons were all fundamental particles, not having an internal structure made of other constituents. Works of Fermi, Sakata, Ikeda, Ogawa [10, 11, 12] did hypothesize that they could have internal structures and be made of unknown fundamental particles.

Gell-Mann and Zweig, independently, correctly predicted that hadrons were composites of quarks and antiquarks, which made sense with the the growing number of hadrons being detected at the time. Another sustaining argument in favor of the quark model were experiments being conducted at SLAC [13, 14] that pointed in the direction of the existence of substructure in the atomic nucleus, since electrons were sometimes scattered with large angles from it, in a similar manner of the experiment conducted by Rutherford in 1919 [15].

The second important idea to advance the theories being constructed concerned *local* or *gauge symmetries*. In 1954 [16] Chen-Ning Yangand Robert Laurence Mills

formulated a gauge theory based on the group $SU(2)$ (more on Subsection 2.1.1) hoping that it could be used to describe the strong interaction. Yang-Mills theories had a profound impact on the Quantum Field Theories (QFT) progress and the description of the particles' interactions, being directly used to construct *Quantum Chromodynamics* (QCD) [17] and the unification of Electrodynamics and the Weak interaction into the *Electroweak Theory* [18, 19, 20]. One of the novel traits of the theory was that symmetry generates interactions, instead of the usual opposite path to construct theories, defining an interaction and seeking the symmetry implied by it.

The third of the distinguished ideas that contributed to the making of the SM was that of *spontaneously symmetry breaking* (Subsection 2.1.3). Using both concepts of local symmetry and spontaneous symmetry breakdown that Peter Higgs formulated in 1964 [21] the *Higgs Mechanism* (the Nambu-Goldstone theory was the basis of it), predicting a massive boson in conditions met by the electroweak interactions, the latter called *Higgs boson*.

To better understand the subtleties involved in the cited theories and the milestones achieved in the last decades regarding our knowledge about particles' origin and interaction, this chapter extends this discussion in further details.

2.1 Electroweak Interaction

Constructed through the efforts of Glashow [22, 19], Weinberg and Salam [18, 20], the Electroweak theory unified both Electrodynamics and the theory of Weak forces, first formulated as the β-decay theory by Fermi in 1934 [23], through the formalism of Yang-Mills gauge theory, based on the $SU(2)_L \otimes U(1)_Y$ group. The $SU(2)$ group is associated with the weak isospin and is mediated by the gauge bosons W^+, W^- and W^0, while the $U(1)_Y$ group is related to the weak hypercharge and requires the gauge boson B_0.

To understand the subtleties of these processes it is necessary that we study more deeply how symmetries, gauge theories, spontaneous symmetry breaking are intertwined in the context of the electroweak interaction.

2.1.1 Symmetries and Gauge Theories

The concept of symmetry played a very important role in physics, from Galilean transformations, to spacetime symmetries in the special relativity realm - both

examples of *global symmetries*. *Group theory* is the branch of mathematics that studies the structures underlying symmetries, and together with *representation theory* were important to particle physicists in the 20th century due to its fundamental applications in the physical theories being developed.

A group consists of a set of elements $G = \{g_i\}$ with a binary *closed* operation $(\cdot)$, meaning that

$$\forall\ \{g_1, g_2\} \in G,\ g_1 \cdot g_2 = g_3 \in G,$$

that satisfies

- Associativity: $(g_1 \cdot g_2) \cdot g_3 = g_1 \cdot (g_2 \cdot g_3)$,
- Existence of a unique identity: $\exists\ g_i \in G$ such that $g_i \cdot g_1 = g_1,\ \forall g_1 \in G$,
- Existence of inverse elements: $\forall\ g_1 \in G,\ \exists\ g_{-1} \in G$ such that $g_1 \cdot g_{-1} = g_i$.

As an example, we can consider the three-dimensional rotations in the Euclidean space. Any rotation in this space can be parametrized by three parameters, the Euler angles: (α, β, γ). One representation of the rotations is through orthogonal 3×3 matrices which determinant is 1 (special matrices) [24]. Using the multiplication of matrices as the binary operation between these rotation matrices, the special orthogonal 3×3 matrices form a group, thus satisfying all properties cited above, called the $SO(3)$ group. When a physical system in which 3D rotations do not alter its dynamics is encountered, it is said that the system has the $SO(3)$ symmetry.

In 1918 Emmy Noether proved a crucial theorem for the development of modern physics, Noether's theorem (or Noether's first theorem) [25]. It states that in a physical system with conservative forces, for every invariant group of transformations, or symmetry, there exists at least one associated conserved quantity, a constant of motion. The theorem establishes in this way a direct connection between symmetries and dynamics of a system, that would be present throughout the whole development of particle physics in the century.

Another imperative advance that was profoundly important to construct the further theories is the *gauge principle*, used in the development of Quantum electrodynamics (QED), Electroweak theory and QCD, all gauge theories, it is thus relevant that a brief explanation of such theories is given. Although it was not first formulated using this formalism, QED is a gauge theory based on $U(1)$ (*unitary* group, consisting of 1×1 unitary matrices, all complex numbers with absolute value 1) group and is a useful example to better understand these theories [24, 26].

In classical electrodynamics, we can define the electromagnetic interactions through two physical objects, the electric $\vec{E}$ and magnetic $\vec{B}$ fields. Both objects can be expressed by a scalar V and a vector potential $\vec{A}$ - which constitutes the four-vector potential in the Minkowski space $A^\mu = (\phi, \vec{A})$ - as

$$\vec{E} = -\vec{\nabla}\phi - \frac{\partial \vec{A}}{\partial t} \quad , \quad \vec{B} = \vec{\nabla} \times \vec{A}. \tag{2.1}$$

The potential fields can be transformed by what is called a *gauge transformation* through a scalar function χ while maintaining the description of the physical fields

$$\phi \to \phi' = \phi - \frac{\partial \chi}{\partial t} \quad , \quad \vec{A} \to \vec{A}' = \vec{A} + \vec{\nabla}\chi. \tag{2.2}$$

In the covariant formulation (manifestly invariant under Lorentz transformations) the gauge transformation can be written as

$$A_\mu \to A'_\mu = A_\mu + \partial_\mu \chi. \tag{2.3}$$

To describe the fermions' interaction with electromagnetism, so first we write the Dirac Lagrangian of a free fermion field ψ:

$$\mathcal{L}_{\text{Dirac}} = \bar{\psi} i\gamma^\mu \partial_\mu \psi - m\bar{\psi}\psi. \tag{2.4}$$

Notice that if we transform the fields by a global phase factor $\psi \to \psi' = e^{-i\alpha}\psi$ ($\bar{\psi} \to \bar{\psi}' = \bar{\psi}e^{i\alpha}$) the Dirac's Lagrangian is invariant: since the phase factors are complex numbers they commute with the derivatives and cancel each other. However, it would be desirable that, since the interactions and electromagnetic process have a local character, the theory is invariant under local transformations. One way of doing so is considering the phase factor as a function $\alpha(x^\mu)$, implying that

$$\begin{aligned}
\mathcal{L}_{\text{Dirac}}[\psi'] &= \bar{\psi}' i\gamma^\mu \partial_\mu \psi' - m\bar{\psi}'\psi \\
&= \bar{\psi}'[i\gamma^\mu \partial_\mu - m]\psi' \\
&= \bar{\psi}e^{i\alpha x^\nu}[i\gamma^\mu \partial_\mu - m]e^{-i\alpha x^\nu}\psi \\
&= \bar{\psi}e^{i\alpha x^\nu}[i\gamma^\mu(-i\partial_\mu \alpha(x^\nu))\psi + i\gamma^\mu(\partial_\mu \psi) - m\psi]e^{-i\alpha x^\nu} \\
&= \bar{\psi} i\gamma^\mu \partial_\mu \psi - m\bar{\psi}\psi + \bar{\psi}\gamma^\mu(\partial_\mu \alpha(x^\nu))\psi \\
&= \mathcal{L}_{\text{Dirac}}[\psi] + \bar{\psi}\gamma^\mu \psi(\partial_\mu \alpha(x^\nu))
\end{aligned}$$

the Dirac Lagrangian of a free fermion is not invariant under such symmetry, since a non-vanishing extra term appears when local transformations are applied to the Lagrangian.

A possible way out of this would be to introduce another term to the Lagrangian, for example adding a Lagrangian of interaction with an arbitrary field C_μ of the form

$$\mathcal{L}_{\text{Fermion}} = \mathcal{L}_{\text{Dirac}} + c_1 \bar{\psi} \gamma^\mu \psi C_\mu \tag{2.5}$$

taking c_1 as an arbitrary constant, that is invariant by symmetry transformations

$$\begin{aligned}\mathcal{L}_{\text{Arbitrary}}[\psi'] &= c_1 \bar{\psi}' \gamma^\mu \psi' C_\mu = c_1 \bar{\psi} e^{i\alpha(x^\mu)} \gamma^\mu e^{-i\alpha(x^\mu)} \psi C_\mu \\ &= c_1 \bar{\psi} \gamma^\mu e^{i\alpha(x^\mu)} e^{-i\alpha(x^\mu)} \psi C_\mu = c_1 \bar{\psi} \gamma^\mu \psi C_\mu = \mathcal{L}_{\text{Arbitrary}}[\psi].\end{aligned}$$

When transforming $\mathcal{L}_{\text{Fermion}}$ altogether we end up with

$$\mathcal{L}_{\text{Fermion}}[\psi', C_\mu] = \mathcal{L}_{\text{Dirac}}[\psi] + c_1 \bar{\psi} \gamma^\mu \psi \left(C_\mu + \frac{1}{c_1} \partial_\mu \alpha(x^\nu) \right),$$

and if we manage to transform our arbitrary field such that $C_\mu \to C'_\mu = C_\mu - \frac{1}{c_1} \partial_\mu \alpha(x^\nu)$ then $\mathcal{L}_{\text{Fermion}}$ becomes invariant under local transformations:

$$\begin{aligned}\mathcal{L}_{\text{Fermion}}[\psi', C'_\mu] &= \mathcal{L}_{\text{Dirac}}[\psi] + c_1 \bar{\psi} \gamma^\mu \psi \left(C'_\mu + \frac{1}{c_1} \partial_\mu \alpha(x^\nu) \right) \\ &= \mathcal{L}_{\text{Dirac}}[\psi] + c_1 \bar{\psi} \gamma^\mu \psi \left(C_\mu - \frac{1}{c_1} \partial_\mu \alpha(x^\nu) + \frac{1}{c_1} \partial_\mu \alpha(x^\nu) \right) \\ &= \mathcal{L}_{\text{Dirac}}[\psi] + c_1 \bar{\psi} \gamma^\mu \psi C_\mu = \mathcal{L}_{\text{Fermion}}[\psi, C_\mu].\end{aligned}$$

If we identify $C_\mu = A_\mu$ and $c_1 = e$ this new introduced Lagrangian will describe the interaction of fermions with electromagnetic fields. Notice by requiring that our theory respects a symmetry, we ended up creating the interaction of the particles. This idea was profoundly important to the development of the Quantum Field Theories' (QFTs) description of particles and fields. To satisfy the transformation of the field A_μ. In order to cancel the extra term from the Dirac Lagrangian, the gauge freedom (Equation 2.2) can be used as

$$\chi = -\frac{1}{e} \alpha(x^\nu) \implies A_\mu \to A'_\mu = A_\mu - \frac{1}{e} \partial_\mu \alpha(x^\nu)$$

$$\mathcal{L}_{\text{Int}} = e \bar{\psi} \gamma^\mu \psi A_\mu.$$

Thus, we have so far the description of Quantum Electrodynamics given by the Lagrangian

$$\mathcal{L}_{\text{Fermion}} = \bar{\psi} i\gamma^\mu \partial_\mu \psi - m\bar{\psi}\psi + e\bar{\psi}\gamma^\mu \psi A_\mu.$$

Since a Lagrangian must include all terms involving the fields that it is describing, the description of the electromagnetic field properties is missing. A natural choice could be the mass term $m_A A^\mu A_\mu$, but this term is not invariant under a local symmetry transformation of the A_μ:

$$m_A A'^\mu A'_\mu = m_A \left(A^\mu - \frac{1}{e}\partial^\mu \alpha(x_\nu) \right) \left(A_\mu - \frac{1}{e}\partial_\mu \alpha(x^\nu) \right)$$
$$= m_A A^\mu A_\mu + \frac{m_A}{e} \left[\frac{1}{e}\partial^\mu \alpha(x_\nu)\partial_\mu \alpha(x^\nu) - A^\mu \partial_\mu \alpha(x^\nu) - A_\mu \partial^\mu \alpha(x_\nu) \right].$$

Instead of using only the field term A_μ, a term involving its derivatives can be used in order to try to make it invariant. Consider for example an antisymmetric tensor given by

$$c_F F_{\mu\nu} = \partial_\mu A_\nu - \partial_\nu A_\mu, \tag{2.6}$$

with an arbitrary constant c_F. Contracting the indices of this tensor, we obtain an invariant term under local symmetry transformations, since the derivatives of $\alpha(x^\nu)$ commute $\partial_\mu \partial_\nu \alpha = \partial_\nu \partial_\mu \alpha$

$$c_F^2 F'^{\mu\nu} F'_{\mu\nu} = c_F^2 F^{\mu\nu} F_{\mu\nu},$$

thus we are now able to write the full Lagrangian describing QED. Choosing the constant $c_F^2 = -1/4$, $\mathcal{L}_{\text{EM}} = -\frac{1}{4} F^{\mu\nu} F_{\mu\nu}$, and then writing the local invariant Lagrangian:

$$\mathcal{L}[\psi', A'_\mu] = \mathcal{L}_{\text{EM}}[A_\mu] + \mathcal{L}_{\text{Int}}[\psi, A_\mu] + \mathcal{L}_{\text{Dirac}}[\psi] = \mathcal{L}[\psi, A_\mu]. \tag{2.7}$$

When dealing with groups and symmetries, transformations of the form $\psi \to \psi' = e^{-i\vec{G}\cdot\vec{\alpha}}\psi$ define the $\vec{G}$ operators as the *generators* of the transformation, usually represented by matrices. In our case we have a 1×1 unitary matrix as $\vec{G}$, thus it is said that this theory is invariant under a *local U(1) transformations with a gauge transformation*, a structure known as *U(1) gauge theory*, and the electromagnetic field is said to be the *gauge field*.

2.1.2 Electroweak Model as a Yang-Mills Theory

In 1933 Enrico Fermi formulated a theory [23] to describe β-decays in which, apparently, energy and momentum were not conserved, such as the reaction

$$^{14}_{6}\mathrm{C} \rightarrow {}^{14}_{7}\mathrm{N} + e^{-} \quad .$$

To solve this problem, Fermi postulated the existence of a light particle called *neutrino* (later determined to be an antineutrino) that is produced in such processes, and should account for the supposed "missing energy" and momentum. Although Fermi was correct in his rationale, it was later found that this theory, known as *Fermi's four-fermion* theory, described with high accuracy processes up to near a hundred GeV, being a limit of the broader, later developed, *Electroweak theory* (EW).

The formalism that allowed the construction of the EW theory was motivated by another open problem at the time, the description of hadrons. Neutrons and protons similar masses were seen as an indication of a deeper relation between the hadrons, merely differing in their electromagnetic charge, thus a theory describing their related properties was sought. As pointed by Yang and Mills [16]:

> [...] The difference between a neutron and a proton is then a purely arbitrary process. As usually conceived, however, this arbitrariness is subject to the following limitations: once one chooses what to call a proton, what a neutron, at one space time point, one is then not free to make any choices at other space time points.
>
> It seems that this is not consistent with the localized field concept that underlies the usual physical theories. In the present paper we wish to explore the possibility of requiring all interactions to be invariant under independent rotations of the isotopic spin at all space time points.

It was developing a non-Abelian (the operators corresponding to the gauge fields do not commute) $SU(2)$ theory with local invariance that Yang and Mills furnished the tools to construct the EW theory.

Similar to the electromagnetic case, where we can obtain the locally $U(1)$-invariant Lagrangian by replacing $\partial^{\mu} \rightarrow D^{\mu}$, the *covariant derivative*, defined as

$$D^{\mu} = \partial^{\mu} + iqA^{\mu}(x^{\nu}),$$

and transforming as

$$D^\mu \rightarrow D^{\mu\prime} = e^{iq\chi(x^\nu)} D^\mu,$$

using the notation of the last subsection, for a $SU(2)$ theory an analogous procedure can be made. Generalizing the covariant derivative to $SU(2)$[27] acting on t multiplets, where t represents the *weak isospin*[1],

$$D^\mu = \partial^\mu + ig\vec{T}^{(t)} \cdot \vec{W}^\mu(x^\nu)/2 \tag{2.8}$$

where g is a coupling constant, similar to the charge q in QED, $\vec{T}^{(t)}$ are $(2t+1) \times (2t+1)$ matrices satisfying

$$[T_i^{(t)}, T_j^{(t)}] = i\epsilon_{ijk} T_k^{(t)}, \quad \text{for } i,j,k \in \{1,2,3\}. \tag{2.9}$$

and $\vec{W}^\mu$ are the three *independent gauge fields* of the theory: $\vec{W}^\mu = (W_1^\mu, W_2^\mu, W_3^\mu)$.

Due to non-Abelian character of the theory, the field strength tensor is given by

$$\vec{F}^{\mu\nu} = \partial^\mu \vec{W}_i^\nu - \partial^\nu \vec{W}_i^\mu - g\vec{W}^\mu \times \vec{W}^\nu. \tag{2.10}$$

where $\times$ represents the cross product of the vectors. This non-Abelian $SU(2)$ was the starting point in the development of the Electroweak unification theory, using the Yang and Mills work to describe the weak interaction [1].

Before entering the discussion of the Electroweak theory, it is relevant to explain that in the Standard Model theory the fermionic matter (leptons, quarks and neutrinos) is organized in three families of particles

$$\begin{bmatrix} \nu_e & u \\ e^- & d' \end{bmatrix}, \quad \begin{bmatrix} \nu_\mu & c \\ \mu^- & s' \end{bmatrix}, \quad \begin{bmatrix} \nu_\tau & t \\ \tau^- & b' \end{bmatrix} \tag{2.11}$$

and each quark can have three colors (more on 2.2), and each family is treated within the structure of doublets (left-handed) and singlets (right-handed)

$$\begin{bmatrix} \nu_l & q_u \\ l^- & q_d \end{bmatrix} \equiv \begin{pmatrix} \nu_l \\ l^- \end{pmatrix}_L, \begin{pmatrix} q_u \\ q_d \end{pmatrix}_L, l_R^-, q_{uR}, q_{dR}. \tag{2.12}$$

An analogous structure stands for the antiparticles. These families of particles interact with identical properties, different among them only in mass and quantum

[1] In the Yang and Mills article the hadronic isospin was interpreted as t, but in the Electroweak framework we are dealing instead with the weak isospin.

numbers.

In order to describe the weak interaction between several fermionic flavors, including the nuances of treating left-handed and right-handed fermions in the doublets and singlets structure, together with the electromagnetic interaction of these particles the simplest symmetry group required [28] is

$$G \equiv SU(2)_L \otimes U(1)_Y, \tag{2.13}$$

where L indicates left-handed field and Y will be further explained and defined as the hypercharge.

In order to simplify the calculations it will be only considered one family of quarks or leptons, identified as

$$\psi_1(x) = \begin{pmatrix} u \\ d \end{pmatrix}_L \quad , \quad \psi_2(x) = u_R \quad , \quad \psi_3(x) = d_R \tag{2.14}$$

$$\psi_1(x) = \begin{pmatrix} \nu_e \\ e^- \end{pmatrix}_L \quad , \quad \psi_2(x) = \nu_{eR} \quad , \quad \psi_3(x) = e^-_R \tag{2.15}$$

abbreviating $x \equiv x^\mu$.

Similar to the QED case, we start with the free Lagrangian of the model:

$$\mathcal{L}_0 = \sum_{i=1}^{3} i\bar{\psi}_j(x)\gamma^\mu \partial_\mu \psi_j(x), \tag{2.16}$$

invariant under global symmetry group transformations given by

$$\begin{aligned} \psi_1(x) \to \psi_1' &\equiv e^{iy_1\beta} U_L \psi_1(x) \\ \psi_k(x) \to \psi_k' &\equiv e^{iy_k\beta} \psi_k(x), \text{ for } k \in \{2,3\} \\ U_L &= \exp\left[i\frac{\sigma_i}{2}\alpha^i\right], \text{ for } i \in \{1,2,3\}. \end{aligned} \tag{2.17}$$

where σ_i are the Pauli matrices. Unlike the previous subsection, and in the QCD in the next section, the free Weak Lagrangian does not contain mass terms for the fermions, a consequence of the symmetry $SU(2)_L$, a mass term would mix left and right-handed fields, breaking explicitly the symmetry. The mechanism through which the particles acquire mass is discussed in Section 2.1.3.

In order to to ensure symmetry invariance upon the local transformations, which gauge fields are $\{\alpha^i(x), \beta(x)\}$, we can transform the covariant derivatives

appropriately. In the current symmetry four gauge bosons will be necessary to do so ($\vec{W}_\mu(x), B_\mu(x)$):

$$\begin{aligned} D_\mu \psi_1(x) &\equiv \left[\partial_\mu + ig\tilde{\vec{W}}_\mu + ig' y_1 B_\mu(x)\right] \psi_1(x) \\ D_\mu \psi_k(x) &\equiv \left[\partial_\mu + ig' y_k B_\mu\right] \psi_k(x), \text{ for } k \in \{2,3\} \\ \tilde{\vec{W}}_\mu &= \frac{\vec{\sigma}}{2}\vec{W}_\mu, \end{aligned} \tag{2.18}$$

where $\tilde{\vec{W}}_\mu$ is a $SU(2)_L$ matrix field and g' is the coupling constant relative to the $U(1)_Y$ group interaction.

Finally, we use the gauge freedom to guarantee the $SU(2)_L \otimes U(1)_Y$-invariance of the free Lagrangian:

$$B_\mu(x) \to B'_\mu(x) = B_\mu(x) - \frac{1}{g'}\partial_\mu \beta(x), \tag{2.19}$$

$$\tilde{\vec{W}}_\mu \to \tilde{\vec{W}}'_\mu = U_L(x)\tilde{\vec{W}}_\mu U_L^\dagger(x) + \frac{i}{g}\partial_\mu U_L(x) U_L^\dagger(x), \tag{2.20}$$

where the B_μ gauge field transforms as the A_μ in the QED theory.

The free Lagrangian can be now written taking into account the Electroweak interactions and invariance under $SU(2)_L \otimes U(1)_Y$ transformations:

$$\mathcal{L} = \sum_{j=1}^{3} i\bar{\psi}_j(x)\gamma^\mu D_\mu \psi_j(x). \tag{2.21}$$

For the kinetic term of the theory, we must first define the field strengths relative to the gauge fields:

$$B_{\mu\nu} \equiv \partial_\mu B_\nu - \partial_\nu B_\mu \tag{2.22}$$

$$\tilde{\vec{W}}_{\mu\nu} \equiv \partial_\mu \tilde{\vec{W}}_\nu - \partial_\nu \tilde{\vec{W}}_\mu + ig[\tilde{\vec{W}}_\mu, \tilde{\vec{W}}_\nu] \tag{2.23}$$

$$\tilde{\vec{W}}_{\mu\nu} \equiv \frac{\vec{\sigma}}{2}\vec{W}_{\mu\nu}, \quad \vec{W}_{\mu\nu} = \partial_\mu \vec{W}_\nu - \partial_\nu \vec{W}_\mu - g\vec{W}_\mu \times \vec{W}_\nu. \tag{2.24}$$

The kinetic term of the Lagrangian can then be cast as

$$\mathcal{L}_{\text{Kin}} = -\frac{1}{4}B_{\mu\nu}B^{\mu\nu} - \frac{1}{4}\vec{W}_{\mu\nu} \cdot \vec{W}^{\mu\nu}, \tag{2.25}$$

where $\cdot$ represente the scalar product. Note that the second term of the Lagrangian will give rise to quadratic, cubic and quartic terms involving the bosons.

From the Lagrangian 2.21 we can obtain the interactions between fermions and gauge bosons, the ones responsible for particle decays which motivated the first works dealing with the weak interaction,

$$\mathcal{L} \supset -g\bar{\psi}_1\gamma^\mu\tilde{\vec{W}}_\mu\psi_1 - g'B_\mu\sum_{j=1}^{3} y_j\bar{\psi}_j\gamma^\mu\psi_j. \tag{2.26}$$

In particular, the first term, containing the $\tilde{\vec{W}}_\mu$ matrix encodes the interaction between the charged-current interactions of the boson fields $W^{\pm\dagger} = (W^1_\mu \pm W^2_\mu)/\sqrt{2}$. Thus, for a family of quarks and leptons the charged-current Lagrangian term is

$$\mathcal{L}_{\text{CC}} = -\frac{g}{2\sqrt{2}}\left\{W^{-\dagger}\left[\bar{u}\gamma^\mu(1-\gamma_5)d + \bar{\nu}_e\gamma^\mu(1-\gamma_5)e\right] + \text{h.c.}\right\}. \tag{2.27}$$

From Equation 2.26 a neutral-current can be retrieved involving the electromagnetically neutral fields W^3_μ and B_μ, we wish to identify them with the Z^0 and γ. B_μ can not be readily identified as the photon since from relations 2.18 this would imply that $y_1 = y_2 = y_3$ and $g'y_j = eQ_j$ are both true.

We can try to identify the desired bosons with the gauge fields with a linear combination of the latter:

$$\begin{pmatrix} W^3_\mu \\ B_\mu \end{pmatrix} \equiv \begin{pmatrix} \cos\theta_W & \sin\theta_W \\ -\sin\theta_W & \cos\theta_W \end{pmatrix}\begin{pmatrix} Z^0_\mu \\ A_\mu \end{pmatrix} \tag{2.28}$$

choosing an arbitrary to be determined angle θ_W. Then we write the Lagrangian term of the neutral-current

$$\begin{aligned}\mathcal{L}_{\text{NC}} = -\sum_j \bar{\psi}_j\gamma^\mu\Big\{ & A_\mu\left[g\frac{\sigma_3}{2}\sin\theta_W + g'y_j\cos\theta_W\right] \\ & + Z_\mu\left[g\frac{\sigma_3}{2}\cos\theta_W - g'y_j\sin\theta_W\right]\Big\}\psi_j.\end{aligned}$$

Identifying the terms with the QED desired terms we obtain

$$g\sin\theta_W = g'\cos\theta_W = e; \quad Y = Q - T_3, \quad \text{where } T_3 = \frac{\sigma_3}{2} \tag{2.29}$$

with Q being the charge operator defined as

$$Q_1 \equiv \begin{pmatrix} Q_{u/\nu} & 0 \\ 0 & Q_{d/e} \end{pmatrix}, \quad Q_2 = Q_{u/\nu}, \quad Q_3 = Q_{d/e}. \tag{2.30}$$

In this way, electromagnetism and the weak interaction have been unified and the hypercharges and weak isospin quantum numbers have been fixed by the conditions imposed 2.29. The y_j components for quarks and leptons turned out to be

$$\begin{aligned}
\text{Quarks: } y_1 &= Q_u - \frac{1}{2} = Q_d + \frac{1}{2} = \frac{1}{6} \\
y_2 &= Q_u = \frac{2}{3} \\
y_3 &= Q_d = -\frac{1}{3}, \\
\text{Leptons: } y_1 &= Q_\nu - \frac{1}{2} = Q_e + \frac{1}{2} = -\frac{1}{2} \\
y_2 &= Q_\nu = 0 \\
y_3 &= Q_e = -1.
\end{aligned}$$

From the relations 2.29 we can write the neutral-chard current term of the Lagrangian separating the QED and Z^0 contributions defining

$$\mathcal{L}_{\text{NC}} = \mathcal{L}_{\text{QED}} + \mathcal{L}_{\text{NC}}^{Z^0} \tag{2.31}$$

$$\mathcal{L}_{\text{QED}} = -eA_\mu \sum_j \bar{\psi}_j \gamma^\mu Q_j \psi_j \equiv -eA_\mu J^\mu_{\text{EM}} \tag{2.32}$$

$$\mathcal{L}_{\text{NC}}^{Z^0} = -\frac{e}{2\sin\theta_W \cos\theta_W} J^\mu_{Z^0} Z^0_\mu \tag{2.33}$$

in which the neutral fermionic current is

$$J^\mu_Z \equiv \sum_j \bar{\psi}_j \gamma^\mu \left(\sigma_3 - 2\sin^2\theta_W Q_j\right) \psi_j = J^\mu_3 - 2\sin^2\theta_W J^\mu_{\text{EM}}. \tag{2.34}$$

When discussing the kinetic Lagrangian of the theory it was pointed out that cubic and quartic terms of self-interaction of the gauge fields appear, they are explicitly:

$$\begin{aligned}
\mathcal{L}_3 = ie\cot\theta_W \Big\{ &\left(\partial^\mu W^{+\nu\dagger} - \partial^\nu W^{+\mu\dagger}\right) W^{-\dagger}_\mu Z_\nu - \left(\partial^\mu W^{-\nu\dagger} - \partial^\nu W^{-\mu\dagger}\right) W^{+\dagger}_\mu Z^0_\nu \\
&+ W^{+\dagger}_\mu W^{-\dagger}_\nu \left(\partial^\mu Z^{0\nu} - \partial^\nu Z^{0\mu}\right) \Big\} + ie \Big\{ \left(\partial^\mu W^{+\nu\dagger} - \partial^\nu W^{+\mu\dagger}\right) W^\dagger_{+\mu\dagger} A_\nu \\
&- \left(\partial^\mu W^{-\nu\dagger} - \partial^\nu W^{-\mu\dagger}\right) W_{+\mu\dagger} A_\nu + W^{+\dagger}_\mu W^{-\dagger}_\nu \left(\partial^\mu A^\nu - \partial^\nu A^\mu\right) \Big\}
\end{aligned} \tag{2.35}$$

$$\begin{aligned}\mathcal{L}_4 = &-\frac{e^2}{2\sin^2\theta_W}\left\{\left(W_\mu^{-\dagger}W^{+\mu\dagger}\right)^2 - W_\mu^{-\dagger}W^{-\mu\dagger}W_\nu^{+\dagger}W^{+\nu\dagger}\right\}\\ &- e^2\cot^2\theta_W\left\{W_\mu^{-\dagger}W^{+\mu\dagger}Z_\nu^0 Z^{0\nu} - W_\mu^{-\dagger}Z^{0\mu}W_\nu^{+\dagger}Z^{0\nu}\right\}\\ &- e^2\cot\theta_W\left\{2W_\mu^{-\dagger}W^{+\mu\dagger}Z_\nu^0 A^\nu - W_\mu^{-\dagger}Z^{0\mu}W_\nu^{+\dagger}A^\nu - W_\mu^{-\dagger}A^\mu W_\nu^{+\dagger}Z^{0\nu}\right\}\\ &- e^2\left\{W_\mu^{-\dagger}W^{+\mu\dagger}A_\nu A^\nu - W_\mu^{-\dagger}A^\mu W_\nu^{+\dagger}A^\nu\right\}.\end{aligned} \tag{2.36}$$

2.1.3 Spontaneous Symmetry Breaking

Since we can not simply add mass terms to the Electroweak Lagrangian, for they violate the $SU(2)_L \otimes U(1)_Y$ symmetry, we explore how to generate the gauge bosons $W^\pm, Z^0$ masses through a mechanism called *spontaneous symmetry breaking* (SSB). Consider a doublet of complex scalar fields in the $SU(2)_L$ group

$$\phi(x) = \begin{pmatrix}\phi^{(+)}(x)\\ \phi^{(0)}(x)\end{pmatrix}, \tag{2.37}$$

where $\phi^{(0)}(x)$ has no electric charge, but $\phi^{(+)}(x)$ does so.

As seen in the previous subsection, the following Lagrangian is invariant under the $SU(2)_L \otimes U(1)_Y$ symmetry

$$\mathcal{L}_S = (D_\mu\phi)^\dagger D^\mu\phi - \mu^2\phi^\dagger\phi - h\left(\phi^\dagger\phi\right)^2, \qquad (h>0, \mu^2<0) \tag{2.38}$$

$$D^\mu\phi = \left[\partial^\mu + ig\tilde{\vec{W}}^\mu + ig' y_\phi B^\mu\right]\phi, \qquad y_\phi = Q_\phi - T_3 = \frac{1}{2}. \tag{2.39}$$

The ground-state of the Lagrangian is actually a set of infinitely many degenerate states invariant under the $U(1)_{\text{QED}}$ group, a symmetry of the vacuum,

$$|\langle 0|\phi^{(0)}|0\rangle| = \sqrt{\frac{\mu^2}{2h}} = \frac{v}{\sqrt{2}}. \tag{2.40}$$

This way, when we choose one of the states as our vacuum state the $SU(2)_L \otimes U(1)_Y$ symmetry will be broken to the electromagnetic subgroup $U(1)_{\text{QED}}$.

However, if a local symmetry is spontaneously broken in the vacuum state, it is possible to reparametrize the Lagrangian describing the system such that instead of new particles appearing, the Goldstone boson's degrees of freedom become longitudinal components of the other particles of the Lagrangian, in the case of

EW theory, these components attribute mass to the $W^{\pm}$ and Z^0 bosons. In order to do so, we begin by parametrizing the scalar fields in the form

$$\phi(x) = \exp\left\{i\frac{\vec{\sigma}}{2}\cdot\vec{\theta}(x)\right\}\frac{1}{\sqrt{2}}\begin{pmatrix}0\\ v+H(x)\end{pmatrix} \tag{2.41}$$

containing the four real scalar fields $\{\theta^1(x), \theta^2(x), \theta^3(x), H(x)\}$. Through gauge fixing, we can reparametrize the Lagrangian in order to eliminate the $\vec{\theta}(x)$ dependence in Equation 2.41 (unitary gauge). Such fields are called *Goldstone bosons*, massless bosons generated by the symmetry breaking, and the number of such particles generated is equal to the number of degrees of freedom that were broken. This is the statement of the *Goldstone Theorem*[29, 30, 31] proven in the early 1960s.

It is precisely this procedure, setting the gauge fields to the unitary gauge, "absorb the gauge bosons", that turns out to generate mass terms in the Lagrangian for the weak bosons. The first term in the Lagrangian 2.38 becomes:

$$(D_\mu\phi)^\dagger D^\mu\phi \to \frac{1}{2}\partial_\mu H\partial^\mu H + (v+H)^2\left[\frac{g^2}{4}W_\mu^{-\dagger}W^{+\mu} + \frac{g^2}{8\cos^2\theta_W Z_\mu^0 Z^{0\mu}}\right]. \tag{2.42}$$

Through the degrees of freedom from the Goldstone bosons absorbed by the $W^{\pm}$ and Z^0 bosons, they now have masses related with each other by

$$M_Z\cos\theta_W = M_W = \frac{1}{2}vg. \tag{2.43}$$

According to the latest measurements [32] the $M_{Z^0} > M_W$

$$M_{Z^0} = 91.1876 \pm 0.0021\,\text{GeV}, \quad M_W = 80.379 \pm 0.012\,\text{GeV}, \tag{2.44}$$

$$M_H = 125.25 \pm 0.17\,\text{GeV}, \quad \alpha^{-1} = 137.035999084 \pm 0.000000021, \tag{2.45}$$

and the electroweak mixing angle can be determined:

$$\sin^2\theta_W = 1 - \frac{M_W^2}{M_{Z^0}^2} = 0.223 \quad . \tag{2.46}$$

It can also be estimated the electroweak scale considering, for example, the $\mu^- \to e^-\bar{\nu}_e\nu_\mu$. Since the momentum transfer $q^2 \ll M_W^2$ the W propagator can be

accurately approximated to the four-fermion interaction:

$$\frac{g^2}{M_W^2 - q^2} \approx \frac{g^2}{M_W^2} = \frac{4\pi\alpha}{\sin^2\theta_W M_W^2} \equiv 4\sqrt{2}G_F, \tag{2.47}$$

and using the measured value of Fermi constant

$$G_F = 1.1663787 \pm 0.000\,000\,6 \times 10^{-5}\text{GeV}^{-2}, \tag{2.48}$$

leads to

$$v = \left(\sqrt{2}G_F\right)^{-1/2} = 246\,\text{GeV}. \tag{2.49}$$

We can also write the following useful relations as function of the determined parameters:

$$\theta_W = \frac{1}{2}\arcsin\left(\frac{2v\sqrt{\alpha\pi}}{M_Z}\right), g = \frac{2\sqrt{\alpha\pi}}{\sin\theta_W}, g' = \frac{2\sqrt{\alpha\pi}}{\cos\theta_W}. \tag{2.50}$$

Through Yukawa-couplings we are able to generate the fermions masses as well, using arbitrary parameters $c_i, i \in \{1,2,3\}$

$$\mathcal{L}_Y = -\frac{1}{\sqrt{2}}(v+H)\left\{c_1\bar{d}d + c_2\bar{u}u + c_3\bar{e}e\right\}, \tag{2.51}$$

and the SSB mechanism generates its masses:

$$m_d = c_1\frac{v}{\sqrt{2}}, \quad m_u = c_2\frac{v}{\sqrt{2}}, \quad m_e = c_3\frac{v}{\sqrt{2}}. \tag{2.52}$$

It is interesting to note that all Yukawa couplings have the same coupling value in terms of the fermion masses:

$$\mathcal{L}_Y = -\left(1 + \frac{H}{v}\right)\left\{m_d\bar{d}d + m_u\bar{u}u + m_e\bar{e}e\right\}. \tag{2.53}$$

Summarizing, by adding the Lagrangian 2.38 invariant under $SU(2)_L \otimes U(1)_Y$ to our Electroweak Lagrangian four additional fields are created, three of which are the would-be Goldstone bosons, absorbed by the weak boson when SSB occurs. In 2012 an excitation of the Higgs Field was first observed, the Boson Higgs, by the ATLAS [33] and CMS [34] experiments. And through the Yukawa couplings, the SSB also generates the fermions' masses.

2.2 Strong Interaction

After using gauge invariance to describe successfully the weak and electromagnetic interaction between particles, a possible path is to try to model the strong interaction between quarks in the same framework. This is fact done by *quantum chromodynamics* (QCD), an $SU(3)_C$ non-Abelian gauge theory, describing the interaction through *gluons* of the quarks, based on the charge of QCD: the colors C. Like electric charge and weak isospin, the color is a property shared by quarks (leptons are color neutral) that governs their interaction through the mediating gluons. The fundamental representation of the $SU(3)_C$ elements is with 8 independent 3×3 matrices - can be thought as representations of gluons in the color space -, each one representing a gluon, that can act on each other, successive group transformations, or act on triplets vectors of the group, the quarks.

2.2.1 QCD Lagrangian

The $SU(3)_C$-invariant QCD Lagrangian is

$$\mathcal{L}_{\text{QCD}} = \bar{\psi}_q^i \left(i\gamma^\mu\right) \left(D_\mu\right)_{ij} \psi_q^j - m_q \bar{\psi}_q^i \psi_{qi} - \frac{1}{4} F_{\mu\nu}^a F^{a\mu\nu}, \tag{2.54}$$

where the fields ψ_q^i denote quark fields with color i, or $\vec{\psi}_q = (\psi_q^R . \psi_q^G, \psi_q^B)$, red, green and blue colors, respectively. The covariant derivative is given by

$$(D_\mu)_{ij} = \delta_{ij}\partial_\mu - i g_s t_{ij}^a A_\mu^a, \tag{2.55}$$

with g_s denoting the strong coupling constant, related to α_s through $\alpha_s = \frac{g_s^2}{4\pi}$; t_{ij}^a are defined as

$$t_{ij}^a = \frac{1}{2}\lambda_{ij}^a, \tag{2.56}$$

λ_{ij}^a are the Gell-Mann matrices, and obey the relation

$$[t^a, t^b] = i f^{abc} t_c \tag{2.57}$$

and f^{abc} are the structure constants of the theory. The upper index a denotes the generators of the $SU(3)_C$ group. And in the last term of the Lagrangian, similar to the electroweak theory, the field strengths are by definition

$$F_{\mu\nu}^a = \partial_\mu A_\nu^a - \partial_\nu A_\mu^a + g_s f^{abc} A_\mu^b A_\nu^c, \tag{2.58}$$

the first two terms similar are equal to field strengths of Abelian theories, although the last term comes from non-Abelian character of QCD. This term in the Lagrangian 2.54 will generate 3-gluon and 4-gluon vertices.

2.2.2 The Strong Coupling

The strong coupling definition is based on the β-function:

$$Q^2 \frac{\partial \alpha_s}{\partial Q^2} = \frac{\partial \alpha_s}{\partial \ln Q^2} = \beta(\alpha_s), \tag{2.59}$$

$$\beta(\alpha_s) = -\alpha_s^2(b_0 + b_1\alpha_s + b_2\alpha_s^2 + ...), \tag{2.60}$$

Q^2 denotes the energy scale. Considering only the first term of $\beta(\alpha_s)$, Leading-Order including 1-loop diagrams (of gluons) we obtain an expression for α_s

$$\frac{\partial \alpha_s}{\partial \ln Q^2} = -\alpha_s^2 \left[\frac{11n_C - 2n_f}{12\pi}\right], \tag{2.61}$$

n_C express the number of colors of the theory, and n_f the number of quarks' flavors (in the Standard Model $n_C = 3, n_f = 6$).

From Equation 2.61 we can derive one crucial property of the strong interactions that points to a possible explanation of the absence of observation of free quarks. If we consider processes of high-energy, high-values of Q^2, the strong coupling constant decreases, diminishing the strength of the strong force, thus in this limit the quarks can be treated as free particles, this property is known as *asymptotic freedom*. On the other hand, when examining low energy processes, the running coupling constant increases indefinitely, bounding quarks and gluons more strongly as the energy decreases, thus *confining* such particles, this is thought to be the reason why quarks and gluons were not detected alone so far. This novel property of the QCD theory brings difficulties to treat low energy processes, since the state-of-the-art perturbation techniques developed so far are not applicable to such limits, requiring new approaches to such scenarios. Confinement is also compatible with the observations of hadrons, since they are color neutral, thus we need high energy hadrons collisions to study the inner properties of QCD.

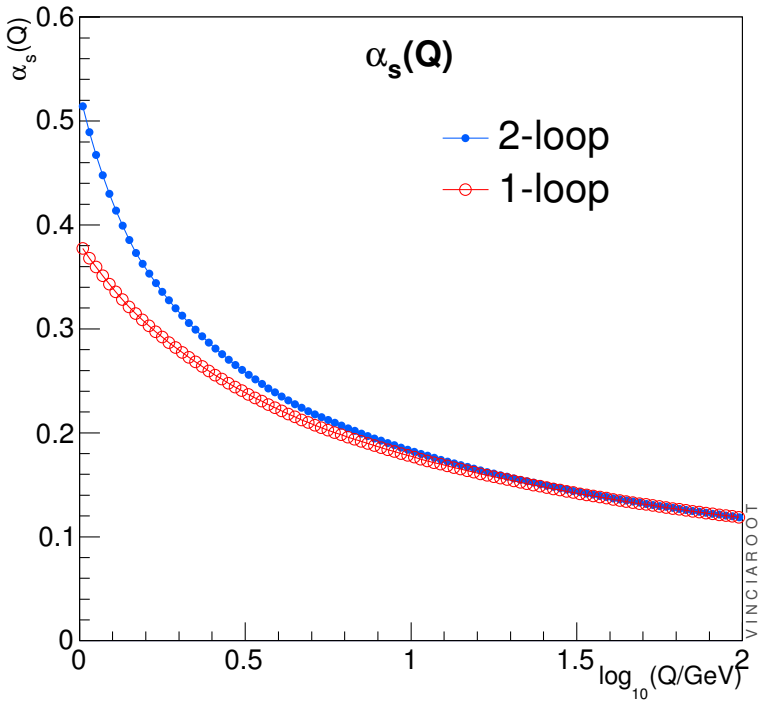

Figure 2.1: Running of the coupling constant α_S at the energy of the Z boson mass, $\alpha_S(M_|) = 0.12$, at 1-loop order (open circles) and 2-loop order (solid circles). From [17].

2.3 Brief History of Particle Physics

After the discovery of the proton by Rutherford in 1919 [15] as a constituent of the nucleus of atoms, the era of experimental particle physics started to flourish. The subsequent evidences of the neutron and positron at the beginning of the 1930s shed more light into the atoms' structure. At the time, the standard interpretation of such recently discovered particles was that they were fundamental particles, the proton and neutron being the fundamental constituents of atoms' nucleus. In 1934, Fermi [23] published his work with the weak interaction, predicting the existence of the neutrino [35]. Beyond its applications strictly to particle physics, the neutrino was in 1940 [36, 37] found to be a key process involved in stellar evolution, known as *Urca process*, by George Gamow and Mário Schenberg - Brazilian astrophysicist and art critic.

It was not until 1947 that the first evidence of a meson, π^-, was first found by Lattes, Occhialini and Powell [38], and in the following years, specially in the 1950's numerous particles were discovered: $\bar{p}, \bar{\nu}_e, \bar{n}, K^0, K^\pm, \Lambda^{++}, ...$ Along these years, a constant collaboration between theoretical and experimentalists exchang-

ing results, testing models was perceived, making such years an overflowing epoch of important advances in the development of theories to describe particles, and mathematical techniques of numerous applications, as well as motivating the formulation of new experiments to test such theories [26]. In 1954 Yang and Mills work [16] was a fundamental step into the construction of renormalizable non-Abelian gauge theories. 1957 several further theoretical developments regarding neutrinos were also published [39, 40, 41], requiring neutrinos to be left-handed or right-handed. In 1958 the first prediction of the Z boson was made by the Brazilian physicist José Leite Lopes [42].

Figure 2.2: César Lattes, Mário Schenberg and José Leite Lopes, from left to right, in a meeting at CNPq in 1958. Retrieved from the Museu de Astronomia e Ciências Afins' archive.

The 1960's were marked by fundamental steps given towards the construction of the Electroweak theory: Glashow in 1961 [22] first introduced the Z^0 boson mediator of the weak force, in 1964 works of Peter Higgs, Englert, Brout [21, 43] predicted the Higgs boson and in a field theory with spontaneous symmetry breakdown usinf the Goldstone bosons introduce massive weak bosons, the Higgs Mechanism. In 1967 Tom Kibble extended the Higgs mechanisms to non-abelian gauge field theories [44], used by Weinberg and Salam to finally construct, independently, the unification of electromagnetism and the weak interaction [18, 20]. Two years later Bjorken invented the Bjorken scaling behavior [13], which would soon be used in the developments that led to the QCD theory.

In the early 1970s, the asymptotic freedom property of interacting Yang-Mills theories was discovered [45], and soon after this work, Fritzsch, Gell-Mann and

Leutwyler invented the QCD Lagrangian(Equation 2.54) [46], enhancing the understanding and predictions regarding strong interactions. The next years were prolific in the establishment of new experiments searching for the predicted particles and even finding unpredicted ones, among the findings: $J/\psi(c\bar{c})$ [47, 48], τ lepton [49], $\Upsilon(b\bar{b})$ [50], evidences of gluon jets [51], $W^{\pm}$ [52], Z^0 [53].

It was also at this epoch that the first measurements of Electroweak and QCD parameters were first measured and compared to the theory of the Standard Model. Some remarkable successes of the SM were the existence of the massive $W^{\pm}$ and Z^0 bosons, gluons, $t$and$c$ quarks, Higgs boson, among many other particles and described its interactions precisely. On the other hand there are still failures of the model in this realm, for example the neutrinos' masses, which are predicted massless by the theory, but experiments show that they have mass, the difference in fermions' masses, the difference in matter and antimatter abundances in the universe, which motivate extensions of SM and the search for new theories. The SM does not explain the dark matter as well, this work will focus on this last issue, trying to enhance our understanding of such phenomena through its study in particle accelerators, in this case in the *Compact Muon Solenoid* (CMS) detector at the *Large Hadron Collider* (LHC).

Before the LHC was built, many high-energy particle colliders had been making numerous discoveries in the realm of particle physics, testing the theoretical advances and finding the predicted, and even unpredicted in many cases, particles. In 1976 the Super Proton Synchroton (SPS) [54, 55] at CERN, a synchroton particle accelerator housed in a tunnel of almost 7 km in circumference, reached operating energy of 400 GeV in its commissioning date. In 1983 the weak bosons $W^{\pm}$ [52] and Z^0 [53] were discovered in the SPS, and later in 1999 a direct detection of CP violation was discovered [56] in it as well. SPS has been used to accelerate beams of protons, antiprotons, electrons and positrons. It served as the injector of the Large Electron-Positron Collider (LEP) [57], a 27 km underground circular collider (passing through France and Switzerland) that provided electron-positron collisions up to $\sqrt{s} = 209$ GeV, the highest energies of such collisions in physics' history. LEP was active between 1989 and 2000, when it was shut down and its tunnel was used to construct the LHC, where CMS is located.

At the United States, the Tevatron [58, 59, 60] synchroton accelerator, located at Fermilab's facilities, was active from 1983 to 2011, colliding protons and antiprotons that were accelerated in a ~ 6 km ring resulting in up to $\sqrt{s} = 1$ TeV collisions. In 1995, the discovery of the top quark at Tevatron [61, 62] was announced, it was

the last fundamental fermion of the Standard Model to be discovered.

The CMS experiment design was motivated by understanding the mechanism of symmetry breaking in the electroweak theory through the Higgs boson, thus the need to detect and reconstruct all particles of an event (even when it does not interact with the detector, such as the neutrino). By doing so, it also tests the mathematical formulation and limits of the Standard Model of particles and fields, shedding light on the consistencies and inconsistencies of the model, and guiding further developments of our description of nature. Many theoretical alternatives have been proposed to solve issues encountered in the SM, such as the hierarchy problem, naturalness, stabilizing the mass of the Higgs, and in particular, searches for supersymmetric models have been conducted [63].

Supersymmetry (SUSY) models are theoretical extensions of the SM, predicting a superpartner particle for every SM particle, and have a myriad possible ways of introducing it: Minimal Supersymmetric Standard Model (MSSM) [64], Anomaly-Mediated Supersymmetry Breaking (AMSB) [65, 66, 67], string-SUSY [68]. An appealing characteristic of R-parity – a conserved quantity introduced by the SUSY models – conserving SUSY models (in MSSM, all SM particles have $R = 1$ while supersymetric particles have $R = -1$) is that its lightest supersymmetric particle (LSP) is stable, and thus can be treated as a dark matter candidate [69]. This is one of the possible ways that the CMS experiment can elucidate the search for physics beyond the standard model, in particular for dark matter, one of the major mysteries in cosmology, astrophysics and particle physics nowadays.

Chapter 3

Dark Matter

3.1 History of the Evidences of Dark Matter

The hypothesis of dark matter was first proposed in 1933 by the Swiss astronomer Fritz Zwicky [3, 70, 71]. In his paper, Zwicky was studying the redshift of extragalactic nebulae. He addresses the disagreement between measurements of the velocity dispersion of the Coma cluster, and the theoretical calculations based on the luminous matter observed. The astronomer suggests that one possible answer to the problem could be the existence of a dark (does not interact via electromagnetism), cold (meaning that dark matter in average has non-relativistic energy, or velocity), type of matter, and its density must be greater than the density of luminous matter in similar clusters.

Zwicky's reasoning on Coma cluster to conclude that an unknown type of matter was responsible for the discrepancies is based on calculations using well known classical mechanics tools. It begins with Newton's second law $\vec{F} = m\vec{a}$ (following the derivation in [72]), assuming a nebula located at $\vec{r}_i$ and of mass M_i and taking the scalar product of $\vec{r}_i$ with $\vec{F} = m\vec{a}$ we obtain

$$\vec{r}_i \cdot \left(M_i \frac{d^2\vec{r}_i}{dt^2} = \vec{F} \right) \quad , \tag{3.1}$$

and summing over all nebulae in the cluster

$$\begin{aligned}
\sum_i M_i \left(\vec{r}_i \frac{d^2\vec{r}_i}{dt^2} \cdot \right) &= \sum_i \vec{r}_i \cdot \vec{F}_i \\
\sum_i M_i \left(\frac{1}{2} \frac{d^2\vec{r}_i^2}{dt^2} - v_i^2 \right) &= \sum_i \vec{r}_i \cdot \vec{F}_i \\
\frac{1}{2} \frac{d^2\Theta^2}{dt^2} &= \mathrm{Vir} + 2K_T \quad ,
\end{aligned}$$

where v_i is the nebulae velocity, $\Theta = \sum_i M_i \vec{r}_i^{\,2}$ is the polar moment of inertia,

$K_T = \sum_i M_i \vec{v}_i^2$ is the total nebulae kinetic energy and $\text{Vir} = \sum_i \vec{r}_i \cdot \vec{F}_i$ is the *virial* of the cluster.

Supposing a stationary nebula, its polar moment of inertia fluctuates around a constant value, by definition, thus the time average of its derivative is zero (another way to argue is noting that the polar moment of inertia value is limited to the cluster size, but we can take the time average over arbitrarily large time window, vanishing the first term)

$$\overline{\text{Vir}} = -2\overline{K_T} \tag{3.2}$$

obtaining the *virial theorem*.

Then, assuming that Newton's inverse square law describes the gravitational interactions among nebulae the potential energy can be written as

$$\text{Vir} = U = -\sum_{i<j} G_N \frac{M_i M_j}{r_{ij}} \quad ,$$

G_N is Newton's gravitational constant and $r_{ij} = |\vec{r}_i - \vec{r}_j|$. The virial theorem then becomes

$$-\overline{U} = -2\sum_i \overline{M_i v_i^2} = -2\sum_i M_i \overline{v_i^2},$$

taking the average over the nebulae velocity (represented by the second bar) we have

$$U = 2\sum_i M_i \overline{v_i^2} = M_{\text{tot}} \overline{\overline{v^2}} \quad .$$

for a cluster mass of M_{tot}.

If, for simplicity, we assume an uniform spherical mass distribution of the cluster of radius R_{tot} and constant density ρ we get

$$\begin{aligned} U &= -G_N \int_0^{R_{\text{tot}}} \frac{(\frac{4}{3}\pi r^3 \rho)(4\pi r^2 \rho dr)}{r} \\ U &= -G_N \frac{16}{15}\pi^2 \rho^2 R_{\text{tot}}^5 \\ U &= -G_N \frac{3M_{\text{tot}}^2}{5R_{\text{tot}}} \quad , \end{aligned} \tag{3.3}$$

giving an estimate of the total mass

$$M_{\text{tot}} = \frac{5R_{\text{tot}}\overline{\overline{v^2}}}{3G_N} \quad . \tag{3.4}$$

Although, if we consider the cluster mass distributed between nebulae two or three nebulae of masses $M_{\text{tot}}/2$ and $M_{\text{tot}}/3$ equally separated by a distance of R_{tot} and $\sqrt{3}R_{\text{tot}}$ respectively, the potential energy becomes

$$U = -\frac{1}{2}G_N\frac{M_{\text{tot}}^2}{R_{\text{tot}}} \text{ and } U = -\frac{\sqrt{3}}{9}G_N\frac{M_{\text{tot}}^2}{R_{\text{tot}}}$$

respectively, only changing the constant multiplying it. Zwicky proceeded using, rather arbitrarily, $U = -5G_N\frac{M_{\text{tot}}^2}{R_{\text{tot}}}$ to get

$$M_{\text{tot}} \gtrsim \frac{R_{\text{tot}}\overline{\overline{v^2}}}{5G_N},$$

using the observed average velocity squared along the line of sight,

$$\overline{\overline{v_s^2}} \approx 5 \times 10^{15}\text{cm}^2\text{s}^{-2}.$$

By the isotropic distribution of the average velocity $v_s^2 = \overline{\overline{v^2}}/3$ and therefore the limit is $M_{\text{tot}} > 4.5 \times 10^{13}M_\odot$.

At the time, based on observations, it was thought that an average nebula had a mass close to $8.5 \times 10^7 M_\odot$, leading Zwicky to conclude that unobserved *dark matter* was responsible for the missing mass. With all the approximations used by the astronomer, the mass-to-light ratio in the Coma cluster was around 500, today this number is set near 400 for galaxy clusters.

On the course of the twentieth century many other evidences of dark matter were observed, bringing it more credibility and attention from the scientific community and establishing it as a promising candidate for BSM physics. Experiments devoted to detect and study dark matter properties have been proposed and performed [73, 74, 75]. In order to understand how this area has been developing, it's important to first understand the evidences that support studying dark matter.

Through radio telescope experiments it became possible to measure the angular velocity of galaxies as a function of their radii. Albeit uniform spheres are not a good approximation for galaxies' modeling, when we consider them as disks we find reasonable results for their velocity distribution. The galaxies' velocity profile

as a function of radius would show an almost linear increase in the bulge, followed by a subsequent decrease that behaves roughly as a Keplerian falloff ($r^{-1/2}$). When compared to the data we find a huge disagreement, with no Keplerian falloff observed in any case. This observation favors the hypothesis of the existence of non-luminous matter in high densities inside galaxies. Under this assumption, theorists calculated the effects of a spherically symmetric dark halo (halo formed of dark matter) around the galaxy. The descriptions given by this hypothesis of the angular velocity as a function of the galaxies' radii reproduces more accurately the observations [4, 76, 77]. Figure 3.1 presents a study of the rotation curves of the galaxy NGC3198 conducted by van Albada showing the agreement of the model of an exponential disk galaxy with a halo of matter encompassing it, while tackling the problem of stability of flattened galaxies pointed by Ostriker and Peebles [78]. The spherical symmetry is a direct consequence of the collisionless property of particle dark matter, meaning that DM does not interact with itself, or interact very feebly, reflecting in its distribution dictated by the gravitational forces.

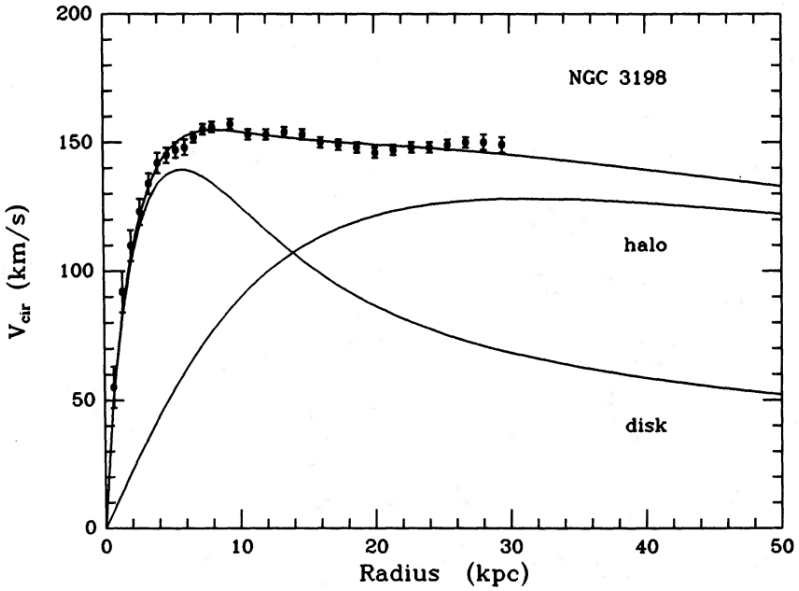

Figure 3.1: Fitting of the rotation curves data (points with error bars) from galaxy NGC3198 with an exponential disk (**disk**), a hypothetical halo of non-observed matter (**halo**) and the upper curve combining an exponential disk with a halo, fitting accurately the data. Taken from [79].

It is relevant to clarify that we are presenting different issues that can be solved introducing DM, although these are inconsistencies in very different scales: galaxies, clusters of galaxies, the Cosmic Microwave Background observations covering the whole sky. In principle, there is no indication that all these problems

have a common cause and solution, albeit some models of particle dark matter, such as the WIMP model, solve theoretically the disagreements of the observations with general relativity and cosmology without DM.

Another evidence that sustains the dark matter searches came from X-ray telescope data. The importance of X-ray data comes from the fact that *in a cluster of galaxies most of the baryonic matter is on the form of gas, and not in stars*. That being said, a hot gas in a gravitational potential well emits Bremsstrahlung radiation, and these photons are in the X-ray frequency. So if we can detect X-ray halos, we can pinpoint the location of the gas in a cluster. Figure 3.2 shows the Bullet Cluster [80]. The color pink represents the cluster locations in which X-ray sources were detected, thus where the gas is, and consequently where the majority of the baryonic matter is. On the other hand, from general relativity we can calculate the effect of gravity bending light trajectories, in what is known as *gravitational lensing* [81, 82]. From those measurements we can also estimate the matter distribution in the galaxy cluster. For the Bullet Cluster this lead to another incompatibility: the lensing indicates that there is a large quantity of matter, in fact more than the baryonic fraction, which were mostly concentrated where no X-ray halos were found. Figure 3.2 shows the different estimations of the matter distribution in the Bullet Cluster, with the final panel showing the merge of the two results: in pink the X-ray halos, and in blue, what is thought to be dark matter.

There are also cosmological evidences for dark matter. From measurements of the CMB (Cosmic Microwave Background), the model of BBN (Big Bang Nucleosynthesis), and measurements of mass-to-light ratio, we can estimate how much of the matter content of the universe. The current estimate of the content of the universe [83] is that 68.3% is composed of dark energy, thought to be responsible for the expansion of the universe, 26.8% is formed by dark matter and 4.9% by baryonic matter, photons, neutrinos, in other words, all the matter that we directly observe and interact with. Since 68.3% of the universe is dark energy, only 31.7% is in the form of matter. Concerning the matter in the universe, almost 85% of it is present as dark matter, implying that "normal matter" sums up to approximately 15% of all the matter.

The term *dark* present in *dark matter* is a consequence of its lack of electromagnetic interaction [84, 85, 86], telescopes and experiments trying to observe DM so far could only find evidence of it through its gravitational interaction. Thus *dark*, since light passes freely through it, at least until today, and none electromagnetic radiation or interaction with charged particles was registered so far.

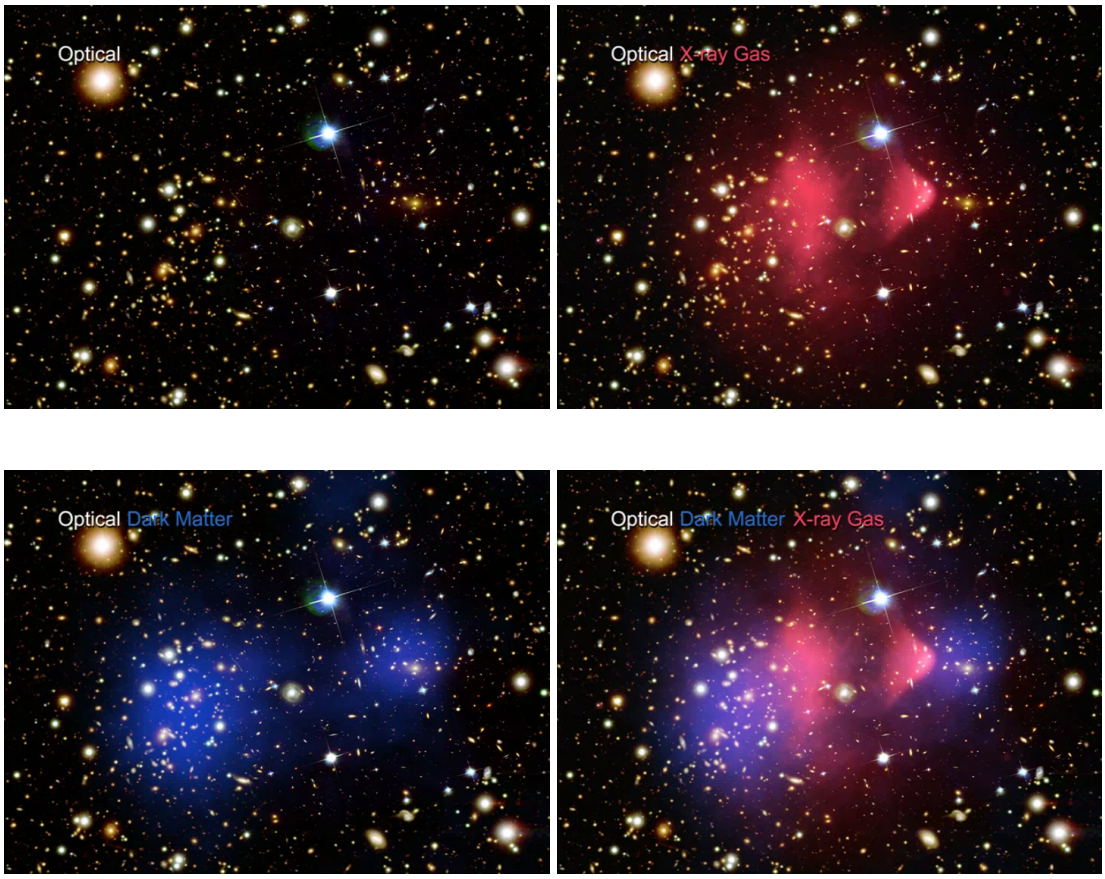

Figure 3.2: Different observations of the Bullet Cluster [5]. Top left: optical only. Top right: optical + matter distribution from X-ray halos (pink). Bottom left: optical + matter distribution from lensing (blue). Bottom right: optical + matter distribution from both X-ray halos and lensing. Since the two methods for measuring the matter distribution disagree, we conclude that a large fraction of the bullet cluster mass is not in the form of hot gas. That assumption is that it is composed of dark matter instead.

The CMB evidence of DM is deeply related to the great revolution of General Relativity started by Einstein and the recent state-of-the-art astrophysics experiments such as *Planck* [83, 87, 88]. A brief review of CMB origin and its relation with DM will be made based on [89]. At the early stage of the universe, until $\sim 10^{-6}$s after the Big Bang, the universe was composed of quarks, leptons and photons in a hot, dense and homogeneous plasma state. As the universe expanded and temperature cooled, the formation of hadrons was possible, binding quarks together. This plasma was "opaque" to photons due to the electromagnetic interaction (Thomson scattering of the radiation), such high density of free electron entailed a very short mean free path for the photons.

With the temperature gradually cooling off, about 4×10^5 years after the Big

Bang (temperature near 1 eV, $T = E/k_B$), most of the hydrogen atoms were not ionized anymore, substantially decreasing the amount of free electrons in the universe. As a consequence, the radiation was not "trapped" anymore to the interactions with electrons, this moment known as *decoupling* (or *recombination*, even though the hydrogens atoms were never combined before) marks the creation of the CMB radiation.

The observations of the CMB [90, 83], Figure 3.3, disclose it as a fairly homogeneous, similar to a perfect black-body radiation at temperature $T = 2.725\,\mathrm{K}$. It also shows small, but consistent fluctuations of the radiation (in the order of 10^{-5} of the background temperature). Since the dominant type of matter at the time of recombination was DM, the irregularities seen in Figure 3.3 are from the distribution of DM itself. Beyond showing that these small "seeds of inhomogeneity" were responsible for the formation of the large cosmological structures observed today, the simulations also show that the velocity of the dark matter particles must be small in order to trap baryonic gas in potential wells. This is why dark matter is thought to be *cold* (its energy is not relativistic), giving rise to the standard cosmological model called ΛCDM: cold dark matter with a cosmological constant.

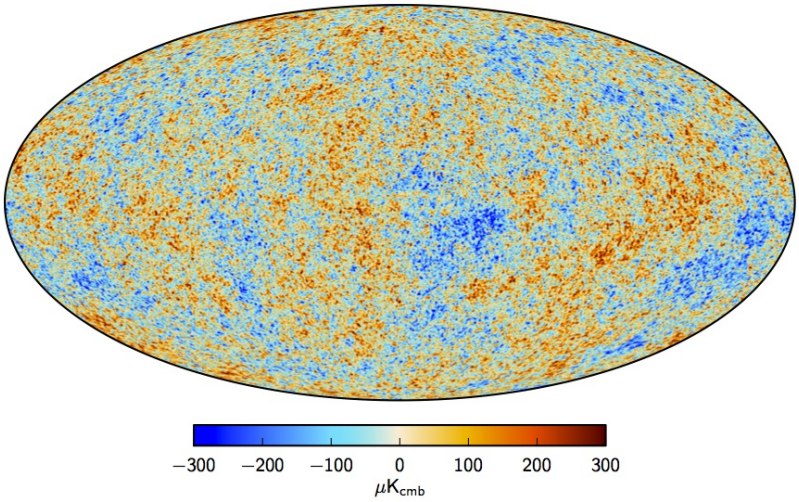

Figure 3.3: The Cosmic Microwave Background Radiation as observed by the Planck satellite. Temperature is given in μK scale, and fluctuations are observed of the order of $\pm 300\,\mu$K [83].

Gravitation models, alternatives to the theory of general relativity, were proposed in order to explain the discrepancies outlined above. These models usually fail to describe the formation of galaxy clusters when considering a universe made only of baryon matter. The disagreements affect the degree of homogeneity of the

CMB, and usually require a time greater than the age of the universe to form the structures that we observe today. Thus, dark matter seeds of inhomogeneity are again the best candidates to explain this evolution. Cosmological simulations are essential to these studies, since through them different cosmology theories can be tested. A simulation of the formation and evolution of clusters and filaments in the ΛCDM model, performed by Kavtsov and Klypin at the National Center for Supercomputer Applications [91], reproduces consistently the observations of these structures in the universe. Figure 3.4 shows their results.

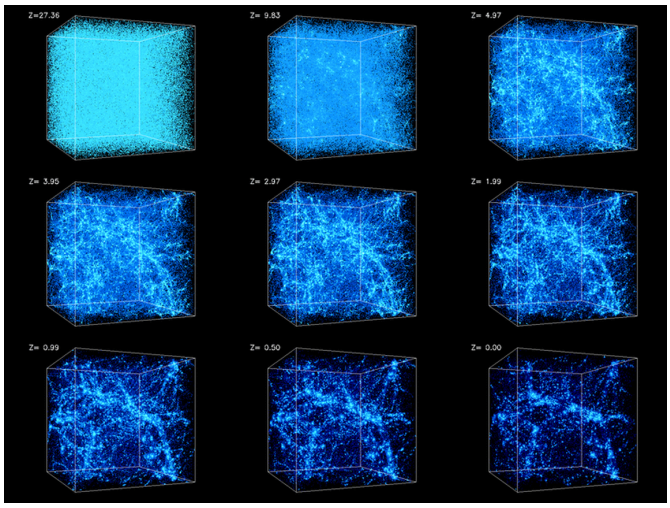

Figure 3.4: Formation of clusters and galactic filaments in cold dark matter model with dark energy. Frames have sides of 140 million of light years, the first one with redshift $z = 30.0$ evolving until today, $z = 0.0$, in the last frame [91].

Gathering the evidences and information known so far, we can infer some characteristics to guide us on constructing models for particle dark matter. The hypothesis that DM is composed of particles is connected to the evidences so far indicating properties of interaction and distribution compatible with developed models of particle dark matter. Also, since all the matter we know can be interpreted as particles, it is convenient to consider DM as particles with different properties. First it must have *neutral charge*, dark, so it doesn't interact with light. A consequence of it is that the particle dark matter will be *frictionless* (does not loose energy through electromagnetic interaction), since baryons cool down through electromagnetic interaction. Having neutral charge, DM does not interact electromagnetically, thus does not have this interaction through which it could lose energy and thus cool its temperature. And since dark matter does not interact with baryonic matter through electromagnetism, the evidences of its existence were observed due to gravitational interaction. On this wise, we expect dark

matter to be *massive*.

So far to build our particle dark matter model we have a great range of possible masses, few constraints in regard to its self interaction and interaction with baryonic matter and some knowledge about its density and distribution on galaxies and galaxy clusters as well as on a cosmological scale of its abundance. In order to look for indications that will reveal the limits of the aforementioned theories, to explain the evidences, and contradictions of the current established theories, experiments are needed. In their very nature and methodology of search, we can identify three distinct groups of *indirect* and *direct detection* experiments [92], and collider experiments.

As the name suggests, indirect detection searches are focused to detect incoming signs of dark matter from observations of the universe. These signs come from the detection of electromagnetic radiation, so it's obvious now why it is not a direct detection of dark matter, because it doesn't interact through electromagnetism. Instead, indirect searches look for signs such as flux of positrons, γ-rays, neutrinos in regions of space with high density of dark matter (could be linked to annihilation during freeze-out) [93, 94].

Direct detection is concerned with detecting dark matter particles through scattering, detecting the recoil of standard model particles. There's a high level of complexity to execute such experiments in order to get rid of the background such that we have a relevant signal of dark matter, since these interactions are expected to happen very rarely. The signals can appear through energy deposits in calorimeters, scintillation light and ionisation, and a wide range of materials can be used to do it: Ge, Xe, NaI [95, 96].

3.2 Outlines of Dark Matter Models

In the last decades, one of the most common frameworks used to develop and explore models of particle dark matter, both theoretical and experimentally, was the *thermal relic* paradigm. Through an interdisciplinary combination of statistical mechanics, general relativity and nuclear and particle physics, these models suggest a history of the origin of dark matter particles, its interaction with the SM (if any) and predict astrophysical observations in order to verify its validity. Since a deep understanding of many physics' areas are needed to grasp the subtleties of such models, I will glance through some core concepts embedded in them. The interested reader can consult the following works for further details

and deeper discussions [72, 97, 98, 99].

3.2.1 Thermal Decoupling

The assumption made by the thermal relic framework is that in the early stage of the universe, an epoch of high energy (or temperature $T = E/k_B$) the species (photons, quarks, nuclei...) were in "thermal equilibrium" in the statistical mechanics' sense, which kept its abundance stable. With the increasing expansion rate of the universe (the Hubble parameter is parametrized by the scale factor $a(t)$ as $H(t) = \dot{a}(t)/a(t)$ at an arbitrary defined time t), its temperature kept cooling off, eventually decreasing the density of the species until its rate of production is surpassed by the universe's rate of expansion. At the time at which the rate of production of the species Γ approaches the value of H, we consider that thermal decoupling takes place, "freezing-out" the number density of the considered particles since from this time on. Since for every t we have an associated temperature T that can be used to parametrize $H(T)$, and the inverse of the latter represents the time at which the expansion had this value, we can estimate the time at which the *freeze-out* happened $t_{\text{f.o.}}$ and temperature $T_{\text{f.o.}}$ satisfying $\Gamma \sim H(t_{\text{f.o.}}) = H(T_{\text{f.o.}})$.

The freeze-out of the relics occur because from this point onwards, as the rate of expansion of the universe grows and enters the regime of $\Gamma \ll H$, this represents that on average the time for the production or annihilation of the particles takes more time than the age of the universe. The species' density is only "redshifted" as the universe expansion continues.

Many processes can vary the relic abundance of a particle species, but here the focus is on three of them:

- Elastic Scattering: $\chi + \text{SM} \leftrightarrow \chi + \text{SM}$.
- Annihilation: $\chi\chi \leftrightarrow \text{SM} + \text{SM}$.
- Self-Annihilation: $\chi\chi \leftrightarrow \overbrace{\chi...\chi}^{n}$ for $n \geq 3$.

More formally, we can analyze the freeze-out of DM using the formalism of Boltzmann's equation, I follow the presentation and reasoning present in [100, 101, 102, 103]. From the assumption that a particle species is in thermal equilibrium early on, we can describe its evolution through its phase-space density $f(\vec{p}, \vec{x}, t)$ with the Boltzmann equation, which can be cast as

$$L[f] = C[f] \tag{3.5}$$

where $L[f]$ is the *Liouville operator*, controlling the evolution of the phase-space density with time, and $C[f]$ the *collision operator*, giving the change in the number of particles per volume of the phase-space per time. Consider the production of a DM particle χ and its annihilation to some SM particle X (lepton, quark, photon ...)

$$\chi\bar{\chi} \leftrightarrow X\bar{X} \quad ,$$

the bar indicates antiparticle. Additionally, we consider that

- The process can happen in both directions. When the rate is the same in both directions, the process is in "chemical equilibrium" and thus $\mu_\chi + \mu_{\bar{\chi}} = \mu_X + \mu_{\bar{X}}$.
- X and $\bar{X}$ have thermal distributions with $\mu_X, \mu_{\bar{X}} \approx 0$.
- For particles and its antiparticles $f_X = f_{\bar{X}}$.
- Distribution functions can be approximated by the Maxwell-Boltzmann distribution functions:

$$f(\vec{p}, T) \simeq e^{-[E(\vec{p})-\mu]/T} \quad .$$

- The scattering process of DM enforces its kinetic and thermal equilibrium, even after decoupling and out of chemical equilibrium, and the phase-space distribution functions satisfy

$$f_\chi(E, T) = \frac{n_\chi(T)}{n_\chi^{EQ}} f_\chi^{EQ}(E, T),$$

where $f_\chi^{EQ}(E, T)$ is the thermal Maxwell-Boltzmann equilibrium distribution function for zero chemical potential and

$$f_\chi(E, T) = e^{(-E+\mu_\chi)/T} = e^{\mu_\chi/T} f_\chi^{EQ}(E, T)$$
$$n_\chi(T) = g_\chi e^{\mu_\chi/T} \int \frac{d^3\vec{p}_\chi}{(2\pi)^3} f_\chi^{EQ}(E) = e^{\mu_\chi/T} n_\chi^{EQ}(T).$$

Now, we want to obtain the evolution of χ's number density n_χ, considering the annihilation process, integrating over Equation 3.5, the Liouville term

becomes [100, 101]

$$g_\chi \int L[f_\chi] \frac{d^3\vec{p}_\chi}{(2\pi)^3} = \frac{1}{a^3}\frac{d}{dt}(a^3 n_\chi) = \dot{n_\chi} + 3Hn_\chi \tag{3.6}$$

and the collision term

$$g_\chi \int C[f_\chi] \frac{d^3\vec{p}_\chi}{(2\pi)^3} = -\int \sigma v (dn_\chi dn_{\bar{\chi}} - dn_\chi^{eq} dn_{\bar{\chi}}^{eq}) \tag{3.7}$$

where $\sigma = \sigma_{\chi\bar{\chi}\to X\bar{X}}$ and $v = \frac{\sqrt{(\vec{p}_\chi \cdot \vec{p}_{\bar{\chi}})^2 - m_\chi^2 m_{\bar{\chi}}^2}}{E_\chi E_{\bar{\chi}}}$, also called the Møller velocity [104], and by its definition a Lorentz invariant when multiplied by $n_\chi n_{\bar{\chi}}$. In our case, it is defined in the *cosmic comoving frame*, or simply *comoving frame*, which is the coordinate system moving with the Hubble's space expansion, where if we measure the CMBR it will be isotropic. Also, in this frame the *comoving distance* is defined if considering 2 comoving objects, their comoving distance will remain constant, factoring out the universe expansion, and the *comoving time* as the elapsed time since the Big Bang in a clock moving in the comoving frame.

From the assumptions regarding thermal and kinetic equilibrium before and after the collision, we can recast Equation 3.7 as [102]:

$$g_\chi \int C[f_\chi] \frac{d^3\vec{p}_\chi}{(2\pi)^3} = -\langle \sigma v \rangle \left(n_\chi n_{\bar{\chi}} - n_\chi^{eq} n_{\bar{\chi}}^{eq}\right) \tag{3.8}$$

where the thermal average $\langle \sigma v \rangle$ is defined as

$$\langle \sigma v \rangle = \frac{\int \sigma v dn_\chi^{eq} dn_{\bar{\chi}}^{eq}}{\int dn_\chi^{eq} dn_{\bar{\chi}}^{eq}} \quad . \tag{3.9}$$

Finally we can write Equation 3.5 as

$$\dot{n_\chi} + 3Hn_\chi = -\langle \sigma v \rangle \left(n_\chi n_{\bar{\chi}} - n_\chi^{eq} n_{\bar{\chi}}^{eq}\right) \quad . \tag{3.10}$$

In order to better understand the implications of Equation 3.10 we can define a new variable $Y = n_\chi / s$, where s is the entropy density, and using the

approximation that $sa^3 = \text{const.}$, a^3 being the comoving volume, we get

$$\frac{d}{dt}(sa^3) = 0 \rightarrow \frac{\dot{s}}{s} = -3H$$
$$\dot{Y}_\chi = \frac{1}{s}\left(\dot{n_\chi} - n_\chi \frac{\dot{s}}{s}\right) = \frac{1}{s}\left(\dot{n_\chi} + 3Hn_\chi\right)$$

and rewrite the Boltzmann equation as

$$s\dot{Y}_\chi = -\langle\sigma v\rangle (Y_\chi^{eq})^2 s^2 \left[\left(\frac{Y_\chi}{Y_\chi^{eq}}\right)^2 - 1\right]$$
$$\frac{\dot{Y}_\chi}{Y_\chi^{eq}} = -n_\chi^{eq}\langle\sigma v\rangle \left[\left(\frac{Y_\chi}{Y_\chi^{eq}}\right)^2 - 1\right]$$
$$\frac{\dot{Y}_\chi}{Y_\chi^{eq}} = -\Gamma \left[\left(\frac{Y_\chi}{Y_\chi^{eq}}\right)^2 - 1\right]$$

where the rate of production of χ is by definition $\Gamma = n_\chi^{eq}\langle\sigma v\rangle$. Lastly, using $x = m/T$ and from the relation between time and temperature in the radiation-dominated era of the universe $dt = \frac{1}{H}\frac{dx}{x}$ we arrive at the expression

$$\frac{x}{Y_\chi^{eq}}\frac{dY_\chi}{dx} = -\frac{\Gamma}{H}\left[\left(\frac{Y_\chi}{Y_\chi^{eq}}\right)^2 - 1\right] \quad . \tag{3.11}$$

Writing in this form, we can see that the deviation of the variable Y_χ from its equilibrium value Y_χ^{eq} is determined by the ratio Γ/H. When $\Gamma \ll H$ it does not change and the density number of χ in the co-moving volume is constant, the annihilation of $\chi\bar{\chi}$ stops. On the other hand, for $\Gamma \gg H$ the value of Y_χ tends to the equilibrium value, thus we define the freeze-out when $\Gamma \sim H$.

3.2.2 WIMPs

The *thermal decoupling* framework has been broadly applied in cosmology to estimate the abundance of particles we observe today in the universe, such as electrons, neutrinos, hadrons, helium, etc. Among its predictions, it encompasses the results of CMB and BBN, that have been sustained by numerous astrophysical experiments' measurements and observations, establishing it in high credibility in the physics community. In this manner, in order to develop a model of DM and

explain its abundance, behavior and understand the subtitles of its interactions, the thermal relic scheme has been used in a myriad approaches, one of the most studied and put to test hitherto has been the model of *Weakly Interacting Massive Particles* (WIMPs).

The observed abundance of DM in the universe is often expressed as $\Omega_{\rm DM} = \rho_{\rm DM}/\rho_{\rm cr}$ times h^2 (h is the Hubble expansion rate today expressed in units of 100 km/s/Mpc, the current estimate is about $h \sim 0.7$) where $\rho_{\rm DM}$ is the density of the thermal relic, and $\rho_{\rm cr}$ is the universe critical density defined as

$$\rho_{\rm cr} = \frac{3H^2}{8\pi G_N}. \tag{3.12}$$

The critical density is called this way since, from the Friedmann equations [72], we can write

$$\Omega - 1 = \frac{k}{H^2 a},$$

k being the *curvature* (can be normalized to 0 in the case of a flat, $+1$ for closed and -1 to an open universe). Thus, the curvature value is determined by Ω, the CMB observations point to $\Omega \sim 1$, implying a flat universe.

The DM density can be expressed as function of the comoving DM density as $\Omega_{\rm DM} = \frac{m_\chi n_\chi}{\rho_{\rm cr}} = \frac{m_\chi Y_0^\chi s_0}{\rho_{\rm cr}}$ with $Y_0^\chi = Y^\chi(T_0)$ indicating the DM density at the present time (and temperature T_0), as well as s_0 the entropy density. Gondolo and Gelmini derived an expression for $\Omega_{\rm DM}$ to be numerically estimated [100] supposing the freeze-out scenario of DM

$$\Omega_{\rm DM} h^2 \approx 8.76 \times 10^{-11} {\rm GeV}^{-2} \left[\int_{T_0}^{T_f} g_\star^{1/2} \langle \sigma v \rangle \frac{dT}{m_\chi} \right]^{-1} , \tag{3.13}$$

with $g_\star^{1/2}$ representing the spin degrees of freedom of χ. Cosmological evidences [83, 87] observe the DM density at $\Omega_{\rm DM} h^2 \approx 0.12$, impelling physicists to develop DM particle models in which $\langle \sigma v \rangle$ and m_χ satisfy the observed abundance, or at least a lesser value, if the hypothesis of more than one type of DM is assumed.

Figure 3.5 shows the relation between Y_χ and x in the freeze-out scheme. At the early universe of high temperature, lower values of x, the behavior of Y_χ is independent of the annihilation cross-section since the DM particles are in thermal equilibrium, thus with constant n_χ in average. As the temperature drops, and the rate of annihilation approximates to the universe expansion's the thermal

decoupling starts, represented by the colored lines in the graph. Lower values of $\sigma_{\chi\bar{\chi}\to X\bar{X}}$ will decouple sooner, as $\Gamma \propto \langle\sigma v\rangle$, and increase the abundance of DM nowadays, since the annihilation stopped earlier, $\Omega_{\rm DM} \propto 1/\langle\sigma v\rangle$.

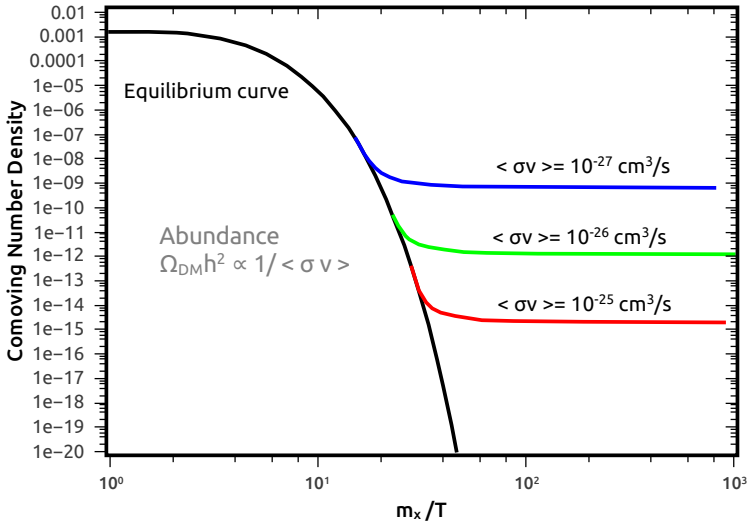

Figure 3.5: Plot showing the profile of the variable $x = m_\chi/T$ as function of the comoving number density $Y_\chi = n_\chi/s$ during the freeze-out scenario. Since the abundance is proportional to the inverse of $\langle\sigma v\rangle$, modelling the annihilation cross-section of the particle DM has a profound importance.

By the end of the 1980s - when the conclusion that the universe was majorly composed of cold and nonbaryonic matter was widely accepted between astrophysicists and particle physicists - a broad range of particle models were being devised: from spontaneously broken gauge theories [105], to quark nuggets resulting from a first-order QCD phase transition [106] and models of universe with higher dimensions [107]. In order to match the observations of DM abundance in the freeze-out paradigm to become a cold thermal relic, there is a lower limit on the order of $1 - 100\,\text{keV}$.

The electroweak interactions of the SM are a natural path to search for new physics given the unsolved problems such as naturalness and hierarchy. Supposing that DM is related to such inconsistencies a model in this scale can be constructed, setting the mass of the particle DM to the electroweak's scale $m_\chi \sim E_{\rm EW} \sim 200\,\text{GeV}$. Further, Figure 3.5 shows that even changing some orders of magnitude the freeze-out temperatures remain close to $x \sim 20$, thus obtaining in this scenario $\langle\sigma v\rangle \approx 10^{-26}\text{cm}^3/\text{s}$. Calculating the abundance of such model of DM today, the result matches the cosmological observations, the so-called *WIMP miracle*. This fact motivated for decades the development of the WIMP model, to

refine its predictions and devise ways to observe it, such as in particle accelerators (Subsection 3.4).

Although, notice that this particular choice of the model parameters (m_χ, $\langle\sigma v\rangle$) is not unique to satisfy the observed Ω_{DM}, such that many other alternative DM particle models have been developed alongside dealing with some caveats of the WIMP model [98].

3.2.3 The WIMPless Miracle

As said before, the WIMP model is by no means the only possible particle DM model which satisfies the particle physics and cosmology requirements, there are a myriad models with masses and interactions that differ from those of electroweak-scale while predicting the cosmological needs. SUSY models with gauge-mediated SUSY breaking [108, 109], for example, devise other particle DM candidates that are not WIMPs.

On the opposite direction of the WIMP particles' interaction, models of *strongly-interacting-massive-particles* (SIMPs) [110] points to dark matter masses in the sub-GeV scale. Instead of the usual $2 \to 2$ process, the SIMP model suggests the annihilation of dark matter via $3 \to 2$ ($m_\chi \sim 100\,\text{MeV}$), also $4 \to 2$ ($m_\chi \sim 100\,\text{keV}$) in the case of DM charged under Z_2 symmetry, but this implies in the heat up of DM, substantially altering the structure formation of halos of dark matter. To overcome this issue, a small coupling to SM is introduced that keeps the DM in thermal equilibrium with the photon bath. This way, the scattering of DM with SM particles allows the heat to flow from the former, maintaining the freeze-out mechanism integrity while maintaining the abundance consistent with the cosmological data.

In a similar fashion, the *ELastically DEcoupling Relic* [111] (ELDER) introduces strongly interacting particles and particularly the self-annihilation process $3 \to 2$ to explain the dark matter thermal relic's evolution. In the ELDER scheme, however, it is the elastic scattering, $\chi + \text{SM} \leftrightarrow \chi + \text{SM}$, that decouples initially from the thermal equilibrium between the two sectors, while the self-annihilation process continues for a period of time, the so-called *Cannibalization*. Since self-annihilation releases energy, the temperature is kept somewhat constant while the universe keeps expanding and the coupling with the SM no longer exists, thus continuing to reduce the number of DM particles. A direct consequence of this framework is allowing lower masses particles or elastic scattering cross-sections, since in the

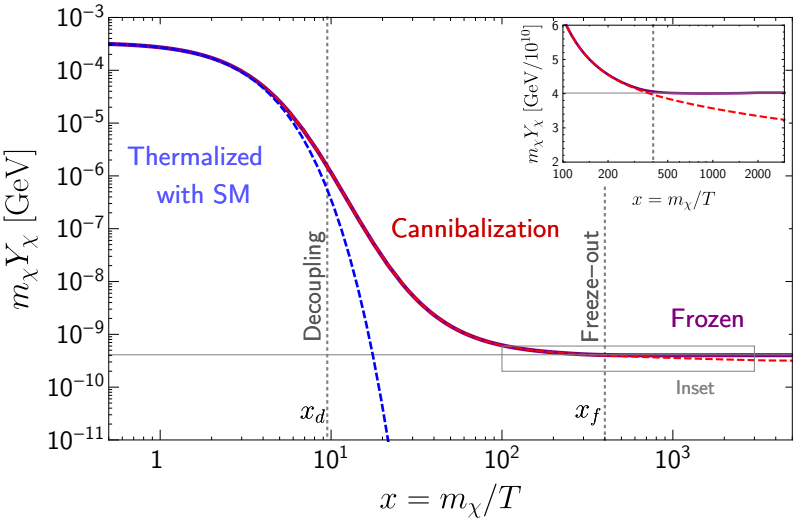

Figure 3.6: Dark matter comoving number density behavior as function of the SM plasma temperature. The blue dashed line represents the DM and SM in thermal equilibrium, the red dashed line DM in chemical equilibrium with itself after decoupling and the purple solid line elastically decoupling dark matter with $m_\chi = 10\,\text{MeV}$. Retrieved from [111].

WIMP model for example lower limits were applied in order to not exceed the observed relic's abundance.

In Figure 3.6 this process is represented with the evolution of x as function of mT, first the decoupling of the two sectors, where the ELDER now is in thermal equilibrium but not with SM. Following the cannibalization epoch, where the self-annihilation process reduces its abundance, and finally the freeze-out.

3.3 Feebly Interacting Massive Particle

Due to the lack of signals found so far that indicates the existence of DM produced via freeze-out mechanism, such as the WIMP, different approaches to explain the DM yield have flourished. Still in the thermal relics' paradigm, the *freeze-in* [112] models have been standing out as an alternate explanation.

Instead of thinking of a particle species in thermal equilibrium with the SM in the early stage of the universe, the freeze-in scheme supposes the existence of a BSM particle Ξ with very low abundance in this epoch. Further, it is supposed that this particle is feebly coupled to the SM particles bath, such coupling is responsible for producing Ξ particles, increasing its number density. Thus, Ξ are called *Feebly Interacting Massive Particles* (FIMPs). The nomenclature *feebly interaction*

instead of what would be more common, *weak interaction*, intends to avoid the confusion with the SM *weak force* interaction. Thus, in the context of FIMPs, unless explicitly stated, weak interactions are referring only to the magnitude of the associated coupling, not the SM weak force. The process of production stops when the universe temperature drops below the mediator mass, "freezing-in" the Ξ abundance. Figure 3.7 illustrate the difference of the evolution of the thermal relics produced within the freeze-out (solid lines) and freeze-in schemes (dashed lines), instead of reducing the particle species abundance as the universe expands, the freeze-in models augment it.

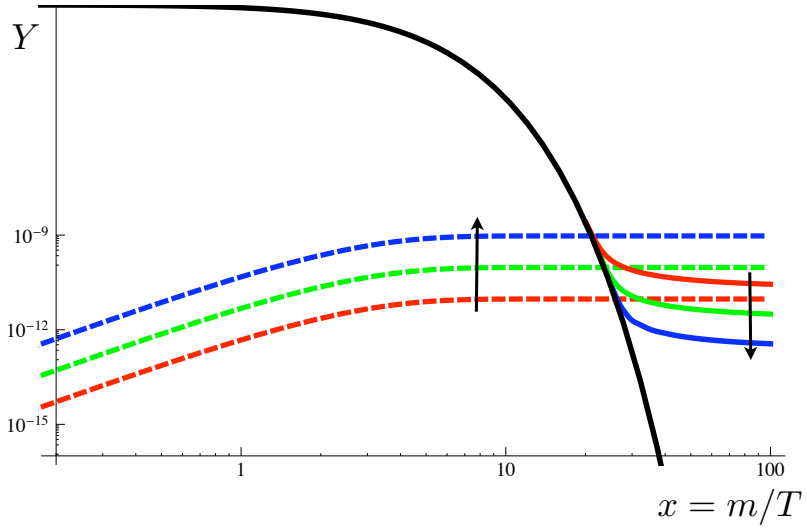

Figure 3.7: Comparison of the evolution of the comoving density number of thermal relics due to SM particles' bath temperature $x = m/T$ in the freeze-in (FI), dashed lines, and the freeze-out (FO) models, solid lines. The arrows indicate the direction in which the processes responsible for the production (FI) or annihilation (FO) of BSM particles have its $\langle \sigma v \rangle$ augmented. Plot from [112].

In particular, we are interested in a FIMP model with a particle $\Xi = F$ coupled to the SM (feebly through a coupling y_Ξ), with a thermal evolution described by the freeze-in framework, which decays through $F \to \text{SM} + s$ into a SM particle and a DM particle s [113]. Formally the SM is extended introducing a real scalar DM s, neutral to $SU(3)_c \times SU(2)_L \times U(1)_Y$ (neutral to strong nuclear interaction and electroweak forces), and a vector-like fermion F satisfying $m_s < m_F$. The coupling to SM is made with the left-handed component of the vector fermion $\bar{F}$ and right-handed SM fermions: up-type quarks, down-type quarks and charged

leptons through Yukawa-type terms:

$$\mathcal{L} = \mathcal{L}_{\text{SM}} + \partial_\mu s \partial^\mu s - \frac{\mu_s^2}{2} s^2 + \frac{\lambda_s}{4} s^4 + \lambda_{sh} s^2 \left(H^\dagger H\right) + \bar{F}(i\not{D})F - m_F \bar{F} F - \sum_f y_s^f \left[s\bar{F} \left(\frac{1+\gamma^5}{2} \right) f + \text{h.c.} \right], \tag{3.14}$$

where $f = \{e, \mu, \tau\}, \{u, c, t\}, \{d, s, b\}$ depending on the model being used for the transformations of F. The model is defined by a set of seven free parameters

$$m_s, m_F, \lambda_{sh}, \lambda_s, \{y_s^f\} \tag{3.15}$$

being the mass of the scalar DM particle, the mass of the vector particle, the coupling of Higgs particles to DM, the DM quartic self-coupling and a set of parameters defining the interaction of DM particle, respectively. Our target, based on [113] analysis, FIMP model being is not focused on the Higgs portal to DM, and the low self-coupling assumed implies in setting $\lambda_{sh} = \lambda_s = 0$.

The set of three parameters $\{y_s^f\}$ describes the interaction of the DM particle s with the visible sector, due to the freeze-in mechanism assumed, the coupling between s and SM is very small. Figure 3.8 represents the FIMP reaction which is a signal we are interested in detecting at CMS, the disappearing track.

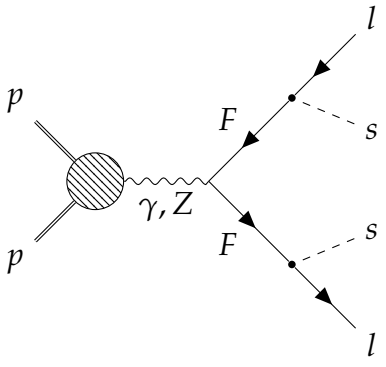

Figure 3.8: Diagram of the FIMP dark matter production at the LHC, from which a disappearing track signal is searched for. Retrieved from [113].

The signal we search in the CMS experiment is possible since the coupling between F and the SM is feeble, implying that the mean lifetime of the introduced particle is increased, allowing it to travel enough to be detected by the CMS detector. If such particle leaves signals in the detector, and decays inside the CMS Tracking System, when reconstructing the particle track a disappearing track will

be found, with inital hits of a charged track followed by its decay with no more hits from a certain layer onwards.

3.4 Search for Dark Matter at the CMS Experiment

At particle detectors we can not detect dark matter directly, since they don't interact neither through electromagnetism nor by nuclear interactions (at least not enough to generate a distinct signal in the detectors of the LHC, but dedicated experiments of direct detection search for these signals), and as consequence are not detected. It's relevant to note that the expected flux of dark matter being produced at the LHC is more than 10^{10} - Chapter 5 - times smaller than the flux coming from outer space, so it' hopeless to expect direct detection coming from the proton collisions.

On the other hand, to search for signs of dark matter at a detector such as CMS we can look for missing transverse momentum (p_T^{miss}). The great accuracy of calibration and alignment of LHC and its detectors allows it to have the beams of colliding protons highly colimated, such that the total momentum carried by the beams can be considered in the z direction, $\vec{p}^{\,\text{beam}} = \vec{p}_z^{\,\text{beam}}$, and null momentum in the transverse plane $\vec{p}_T^{\,\text{beam}} = 0$. Thus, using the conservation of momentum of the collision, we expect that after the collision, if we sum all the reconstructed particles, supposing that all of them are correctly reconstructed, we get

$$\vec{p}_T^{\,\text{beam}} = -\sum_i \vec{p}_T^{\,i} = \vec{0}$$

$\vec{p}_T^{\,i}$ stands for the transverse momentum of the particle i, and the sum is over all final particles. So, if after reconstructing an event we do not obtain 0, we call the difference $\vec{p}_T^{\,\text{miss}}$ – a schematic representation of $\vec{p}_T^{\,\text{miss}}$ in the CMS detector is shown in Figure 3.9. A fraction of the missing energy is expected in the framework of the SM due to neutrinos, and this estimate is made using on the relation between the number of Z bosons decaying to leptons and to neutrinos. Thus counting the number of Z decaying to leptons, the number of neutrinos generated can be estimated. It is through specific signals containing missing momentum, or analogously the missing energy E_T^{miss}, that the analysis search for DM produced in the collider.

The topologies of BSM physics signals are varied, since a myriad models of the particles are possible, thus many parameters such as mass, momentum, the

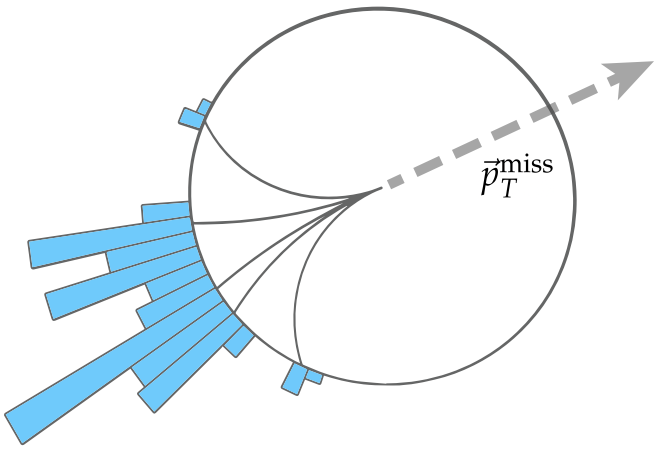

Figure 3.9: Schematic representation of how missing transverse momentum are reconstructed in the CMS detector.

presence or not of SM in the process, the number of exotic particles in the decaying channel. In particular, for DM searches, recently simplified models [114] have been widely used to interpret the collider signals, such models are able to describe the kinetic of DM production and search for a large imbalance in the transverse momentum. The missing momentum searched recoils against some initial state radiation (X), and these searches are called mono-X, where X can be a jet - from the hadronization of quarks and gluons [115] or the decay products of the bosons $W^{\pm}$ [116] or Z [117] - or a photon [118].

In this project, we search specifically for dark matter produced together with long-lived particles (LLP) (meaning that the particle travels a distance that allows it to be detected before it decays) in the framework of the FIMP model. One sign of a dark matter + charged LLP signature can be a reconstructed charged particle (a track) recoiling against undetected particles in the detector; another possible signature that can be related to dark matter + LLP is the detection of a displaced vertex, representing the decay of a neutral LLP, since the vertex is at a considerable distance from the primary vertex. Figure 3.10 shows different topologies of signals containing LLP in the CMS detector's Trigger System. These are the events we are looking forward to detecting in CMS, and in particular in the Tracker system. Therefore, a good understanding of how the particle tracks are reconstructed is essential to our work. In the following three chapters, the reconstruction of charged particle tracks will be studied, firs introducing the CMS detector - Chapter

4 - in which we search for disappearing tracks, then from the basic concepts and a toy model implementation using combinatorial Kalman filter (CKF) - Chapter 5 -, to an analysis of events containing charginos ($\tilde{\chi}^{\pm}$) and its tracking performance using CMS' software package, `CMSSW`- Chapter 6.

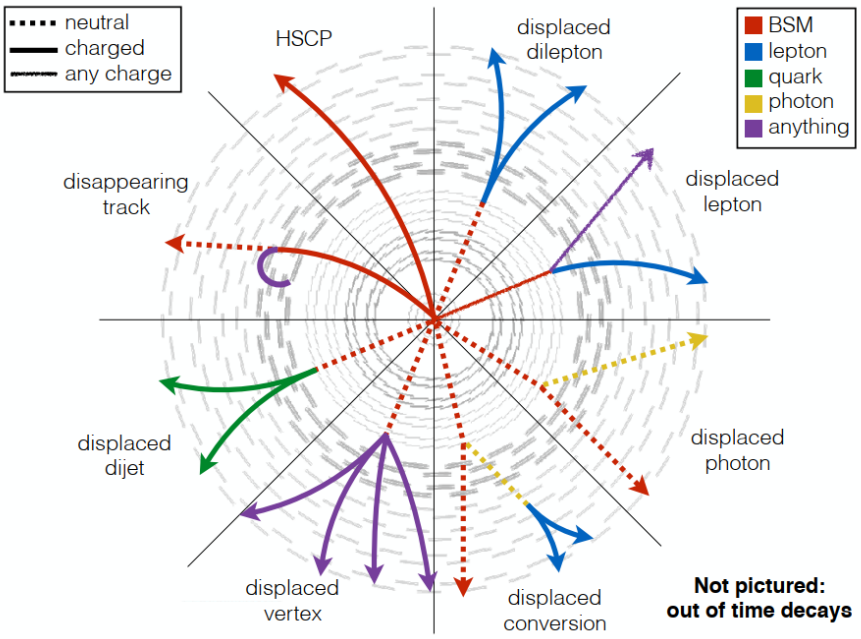

Figure 3.10: Schematic representation of possible signals from LLP in the CMS Tracker System.

Chapter 4

The CMS Experiment

The LHC is a particle accelerator at CERN where pp, pPb and PbPb collisions take place, reaching the highest center of mass energy in the history of physics, $\sqrt{s} = 13\,\text{TeV}$ for pp collisions. The CMS detector [119] is a multipurpose experiment of the LHC, first designed to elucidate our knowledge about particle physics, testing many aspects of the Electroweak theory, such as the Higgs boson prediction, and the limits of the Standard Model, including more recently searching for signs of *Beyond Standard Model* (BSM) theories. The LHC facilities comprises three more detectors: ATLAS [33], ALICE [120] and LHCb [121].

At the LHC the protons[1] bunches are accelerated in a 27 km radius collision ring, reaching up to a luminosity of $2 \times 10^{34}\text{cm}^{-2}\text{s}^{-1}$ (Figure 4.1 shows the increasing values of luminosity over the time of operation of CMS), when they collide in the CMS detector. Collisions at the CMS detector take place every 25 ns, or at a frequency of 40 MHz, and since the bunches are collimated and composed of $\sim 10^{11}$ protons many pp interactions happen in a collision, the number of such interacions is known as *pileup*. In order to be able to differentiate which particles being produced belong to each specific hadrons' collision, a detector with high granularity, low occupancy and fast and efficient reconstruction of the particle tracks and parameters is required. The CMS detector is described in the coordinate system shown in Figure 4.2 by (ρ, η, ϕ), where η is the pseudorapidity, defined as $\eta = -\ln\left(\tan\left(\frac{\theta}{2}\right)\right)$ and the CMS solenoid magnetic field points in the $+z$ direction.

To retrieve as much information about the processes taking place at the collisions as possible, the CMS detector is composed of several components, each one dedicated to specific tasks of the events' reconstruction. The detector is embedded in a magnetic field of 3.8 T which bends the charged particle tracks, aiding the identification and momentum reconstruction of these. The innermost subdetector is the *Tracker System*, responsible for identifying charged particle tracks from the

[1] This project focuses on pp collisions, however collisions with Pb ions also take place at LHC and are investigated by all its experiments.

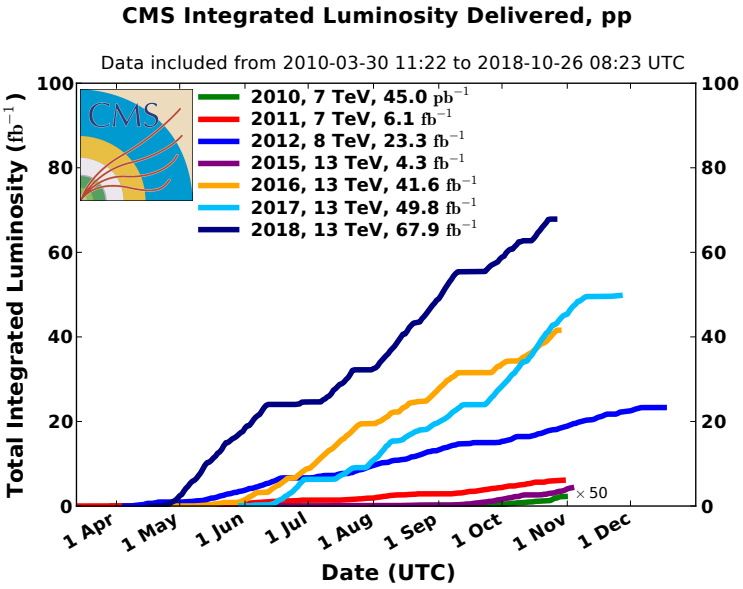

Figure 4.1: CMS integrated luminosity delivered from runs of 2010 to 2018. Retrieved from CMS Public Results.

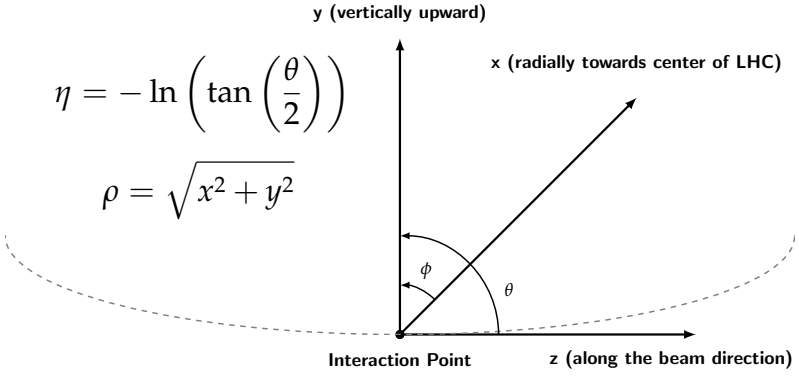

Figure 4.2: CMS detector coordinates system. The colliding beams travel in the z direction and the angular coordinates θ and ϕ range through $[-\pi, \pi]$ and $[0, 2\pi]$, respectively. ρ represents the radial coordinate in the z transverse plane (x, y), while the pseudorapidity is related to θ by $\eta = -\ln(\tan(\theta/2))$. The CMS solenoid magnetic field points in the positive z direction.

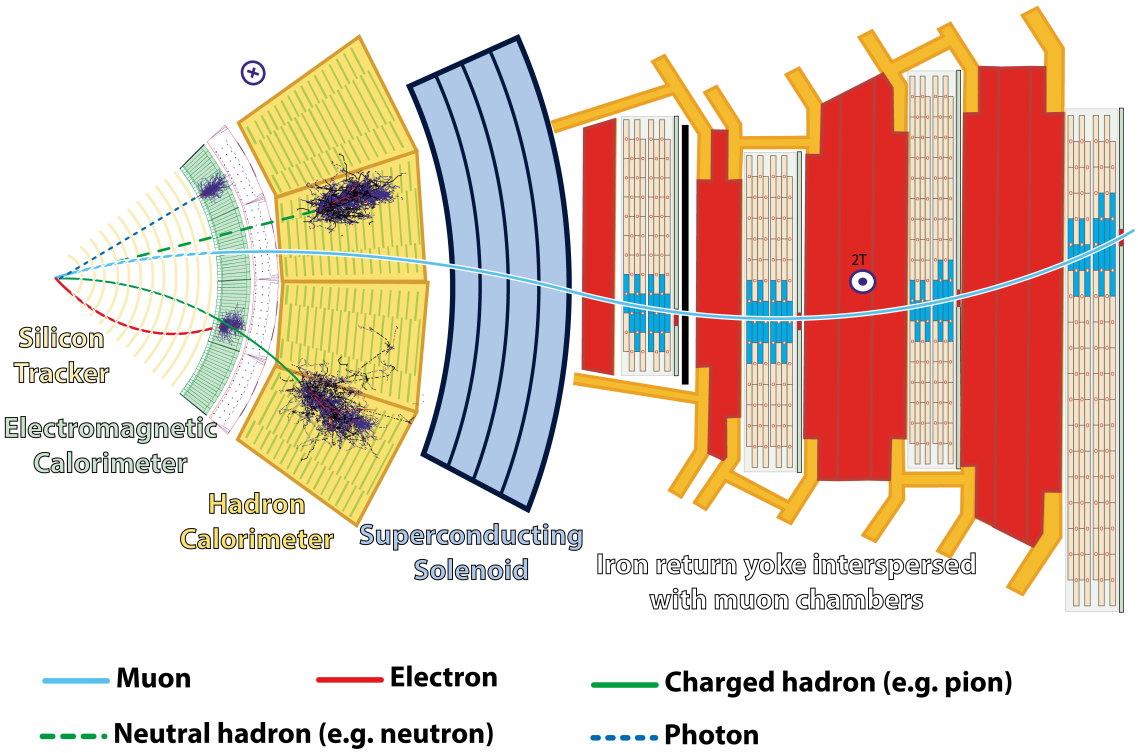

Figure 4.3: CMS detector's components design and how particles interact with them [122].

signals left in the silicon elements of the tracker, determining among other properties, the particles' momentum. Following the tracker, an *Electromagnetic Calorimeter* (ECAL) is placed to interact with charged particles and photons, measuring their energy. Surrounding the ECAL the *Hadronic Calorimeter* (HCAL) is designed to interact and measure the energy of hadrons, thus is fundamental to study apparent missing transverse energy in the collision. Finally, the *Muon Detector System* is responsible for tracking and reconstructing with high precision the charges and momenta of the muons in the entire range of the CMS detector. The detector's layout can be seen in Figure 4.3.

4.1 Tracker System

The Tracker System is the inner subdetector of CMS, it surrounds the interaction point closely and is responsible to provide reliable and precise measurements of the trajectories of charged particles from the collision in LHC, also for reconstructing production vertices. A 3.8 T homogeneous magnetic field pervades the whole detector, generated by the CMS solenoid, bending the charged particles' trajectory

that are reconstructed. The detector is divided in two main components (Figure 4.4):

- Pixel Detector: based on hybrid pixel detectors, it provides measurements with higher granularity and is placed in the inner region of the Tracker (this description of the Pixel Detector refers to its design after the Phase-I Pixel Detector upgrade, further detailed in Subsection 4.1.1). It is divided in two main regions: the Barrel Pixel Detector (BPIX), composed of four cylindrical layers, ranging radially from 2.9 cm to 16.0 cm, providing high precision position measurements. And the Forward Disks (FPIX), using three disks detectors on each end of the detector, extending from $\pm$33.8 cm to $\pm$47.9 cm in z, furnishing higher η coverage. The standard pixel size of the detector has area of $100 \times 150\,\mu\text{m}^2$ and are 285 μm thick.

- Silicon Strip Detector: using silicon micro-strip as the sensor elements it is located after the pixel detector and extends radially from 20 cm to 116 cm [119]. It is subdivided in three regions: the Tracker Inner Barrel and Disks (TIB/TID) provide 4 $r-\phi$ measurements from the cylindrical layers of the TIB and 3 from the TID, from each end, through 320 μm thick sensors. Surrounding it the Tracker Outer Barrel (TOB) is composed of six layers of silicon sensors of 500 μm thickness and supplies 6 $r-\phi$ measurements. The Tracker EndCaps (TEC+ and TEC$-$) are located in the vicinity of all other Tracker components' z, extending to $\pm$282 cm, and within each TEC 9 disks of 320 μm and 500 μm thickness furnish position measurements up to $|\eta| \sim 2.5$.

Due to the proximity with the interaction point, the radiation damage caused by the high flux of particles is an important constraint in the tracker design. At the same time the material budget – amount of material used in the detector – must be kept as low as possible to prevent as much as possible multiple scattering effects and nuclear interactions of the particles of the event with the detector's material. The temperature is also monitored and maintained around $-10\,^{\circ}$C [119] in order for the silicon sensors and electronics function properly, avoiding effects of efficiency loss such as leakage current.

4.1.1 Phase-I Pixel Detector Upgrade

At the end of 2016, during LHC Run 2, a scheduled technical shutdown took place at the accelerator, lasting until April 2017. Since in the first Long Shutdown

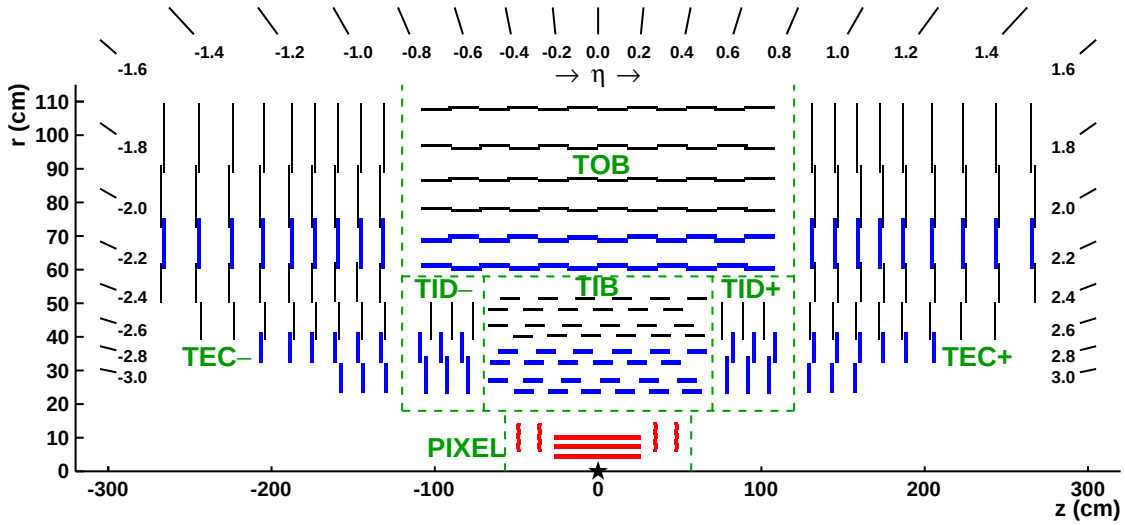

Figure 4.4: Layout of the CMS Tracker System.

(LS1) a new beam pipe was installed in the detector, with a smaller diameter, it was possible to upgrade the innermost Tracker's component, the Pixel detector [123]. The number of layers and sensor modules were increased both in the barrel pixel detector and the forward disks, the Pixel Detector's layout before and after the upgrade are shown in Figure 4.5. The material budget was decreased in some regions and the efficiency of track reconstruction was maintained or increased, event at twice the instantaneous luminosity.

After the upgrade, an additional layer was added in the BPIX, closer to the interaction point. The four layers are located, in the radial coordinate, at 29 mm, 68 mm, 109 mm and 160 mm; further characteristics of the layers are given in Table 4.1. The FPIX had its number of layers increased as well, a third layer of sensors was installed, and each ring was divided into two: the inner and outer ring, increasing the number of modules and the η coverage. This way, when reconstructing particle tracks, we can have an additional hit from the pixel detector closer to the vertex, improving our reconstruction efficiency. A side effect of the inner layer (L1) being closer to the interaction point is that it is degraded more rapidly over time and demands maintenance more frequently in order to maintain its proper function, since it receives more radiation from the collision.

With more layers in the detector, more material is used if the same material and design is used, increasing the probability of interaction and multiple scattering effects of the target particles and the detector's material, reducing the tracking and reconstruction efficiencies. To overcome these problems in the Phase-I upgrade the

BPIX			
Layer	Radius (mm)	z position (mm)	Number of modules
L1	29	-270 to +270	96
L2	68	-270 to +270	224
L3	109	-270 to +270	352
L4	160	-270 to +270	512
FPIX			
Disk	Radius (mm)	z position (mm)	Number of modules
D1 inner ring	45-110	$\pm$338	88
D1 outer ring	96-161	$\pm$309	136
D2 inner ring	45-110	$\pm$413	88
D2 outer ring	96-161	$\pm$384	136
D3 inner ring	45-110	$\pm$508	88
D3 outer ring	96-161	$\pm$479	136

Table 4.1: Dimensional parameters of the Phase-I Pixel detector components.

materials used in the Pixel detector were substituted by lower density carbon-fiber materials, and lighter cooling systems. Likewise, the electronics were placed at higher pseudorapidity, out of the Tracker acceptance region, resulting in a similar material budget for the central region, and decreasing it for $|\eta| > 1$.

Achieving higher luminosity and increasing the number of silicon sensors in the detector claims a higher demand for the electronics to process higher rates of hits. The new design of silicon sensors and the readout chips (ROCs) allowed higher rates of processing, higher radiation tolerance, faster hit transfer from pixels to the periphery while maintainig the single-pixel hit efficiency.

4.1.2 Hit Reconstruction

When dealing with track reconstruction, a fundamental component of this task is the *hit*. While in Subsection 5.1.3 the hits are treated as the outputs of the detector generated by a charged particle passing through it, the objective here is to analyze how they are reconstructed. The Pixel detectors are composed of modules containing 160×416 pixel cells, each pixel cell has a photosensor that is sensitive to electromagnetic radiation and transistors to amplify the electric signals. Silicon Strip Trackers are composed of strips through which the passage of charged particles leaves a signal, that are later on matched to singular tracks. However, the hits' acquisition process involves some intricacies, such as detector malfunctions, the interactions of the particle with the detector's material and the Lorentz drift caused by the detector's magnetic field. Concerning these complications, the *hit*

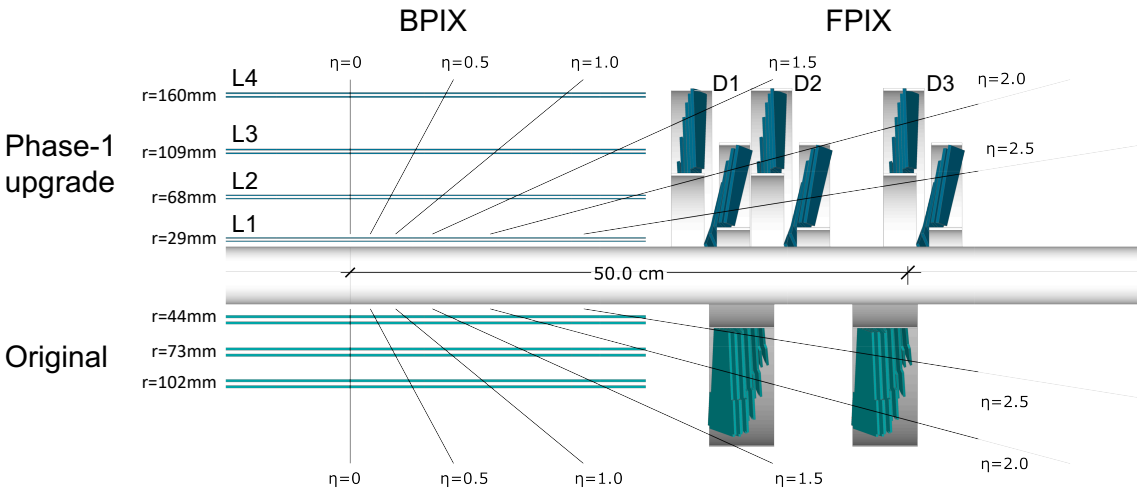

Figure 4.5: Layout of the CMS Pixel detector before and after the Phase-1 Pixel upgrade.

object in the experiment's software stores information about its acquisition, for example the detector, sub-detector, layer where the hit was reconstructed, and a classification of the hits is made [124]:

- *Valid* The detector is functioning properly, and a hit was found;
- *Missing* Detector is functioning properly, but it was expected to find a hit in the layer and there is no hit, thus based on the information from other layers a hit is created *ad hoc*;
- *Inactive* Detector is off, nothing to do about it;
- *Bad* Many bad sensors malfunctioning near it.

What is relevant to our analysis are the Valid Hits, when they were reconstructed properly in a region where the detector was functioning with no problems.

The high-density of pixel sensors in the innermost Tracker component (more than 1,800 silicon sensor modules summing up more than 10^8 pixels with di-

mensions $100 \times 150\ \mu m^2$) [123] demands a fast algorithm to determine the hits' positions while the experiment is running in order to provide it to the Tracker, crucial for the Trigger System for example. To determine a hit's position there are different approaches for the Pixel and the Silicon Strip detectors.

Pixel's Hit Reconstruction

The reconstruction of hits occurs in two steps: the *local reconstruction* when the sensors determine relative to its local coordinates (usually the height and length of the sensor) where the charged particle traversed it, and the *global reconstruction* when the track and its hits are converted to global coordinates (ρ, η, ϕ). In the local reconstruction of pixel sensors, the number of pixels fired by a passing particle are used to estimate the amount of charge deposited in the pixel layers, determining the *charge width*, and then the geometrical position of the hit. Effects such as the Lorentz drift due to the magnetic field are also taken into account when estimating the hits' positions.

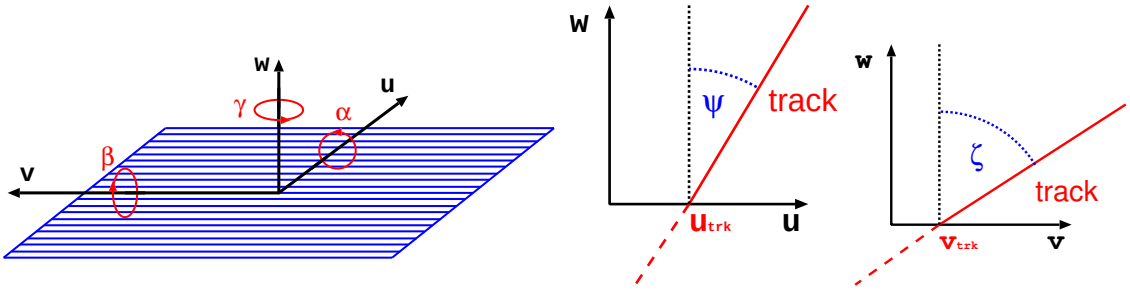

Figure 4.6: Local coordinates of a silicon element (u, v, w) with its respective rotation angles (α, β, γ) (left panel), and the illustration of local track angles (ψ, ζ) [125].

Due to the high level of radiation exposure of the inner tracker, its components are degraded over time, affecting its proper function and efficiency, leading to errors up to $50\,\mu$m in each sensor direction [126]. In order to refine the hits' reconstruction precision, in the final track fit more precise algorithms are needed, such as *template*-based hit reconstruction, in which a simulation of the sensors deterioration and the effects in the detected charges are used to better estimate hits' position [127].

The translation of the local to coordinates is crucial to the performance of the tracker, errors in this conversion propagate to all further processes of tracks reconstruction. To guarantee a reliable conversion, different methods are used: internal alignment of the components of the different subdetectors (adjusting the

relative positions and angles of the modules with each other), measurements of the TOB alignment to the beam axis (and thus the alignment of the other subdetectors to the TOB), calibration of the components of the tracker [125].

Silicon Strip's Hit Reconstruction

In the Silicon Strip Detector, strip signals are accepted as signals of hits based on the amount of charge detected exceeding the sensor's noise, also the thresholds of charge to cluster strips are made this way. Like the algorithms of the Pixel, the position of the hits are determined based on the charge distribution, *charge width*, of the clusters.

The Silicon sensors are divided between thicker sensors, with width of 500 μm which are found in more external Tracker regions (TOB and outter rings of TEC), and thinner sensors, with width of 320 μm (TIB/TID and inner rings of TEC). Beyond the correction of the positions based on the Lorentz drift, the 500 μm sensors also pass through a correction of its position in the direction perpendicular to the sensor active area due to the inefficiency of the back-plane sensor. In this sensor, the charge is poorly collected in the back-plane due to the narrow window of time in which the signals must be sent and the sensor active before the next event takes place, ~ 25 ns.

4.2 Electromagnetic Calorimeter

The Electromagnetic Calorimeter is a homogeneous subdetector, meaning that all of its volume is composed of sensitive material, responsible for detecting photons and electrons. It is composed of more than 70,000 $PbWO_4$ (lead tungstate) crystals and is divided in two components, the central barrel, in which most of the crystals are mounted, and two endcaps closing it. Using high density crystals (8.28 g/cm^3) allows the detector to have a fine granularity, be fast, compact and radiation resistant, all essential needs in this kind of environment. Preceding the ECAL endcaps preshower detectors are installed in order to avoid the misreconstruction of two photons emerging from a decaying pion with small difference in angle as a single high energy photon. The preshower detectors have much finer granularity with detector strips and thus can tag the two distinct photons.

In addition to the high density of $PbWO_4$ crystals, they present short radiation length (0.89 cm), the mean free path of a high-energy electron to lose all its energy

except $1/e$, and a small Molière radius (2.2 cm), the radius of a cylinder containing around 90% of the energy of a shower, creating a fast, efficient and compact calorimeter. Regarding the luminescence of the material it is also a fast scintillator, the crystals' scintillation decay time is around 25 ns, thus compatible with the time between the bunches crossing. The crystals emit a blue-green scintillation light, most of it around 420 nm. In order to operate properly and maintain the energy resolution of the calorimeter during the lifetime of the experiment, the temperatures are strictly monitored and kept at 12 °C in the barrel and -5 °C in the endcaps [128].

The ECAL barrel covers the pseudorapidity range up to $|\eta| < 1.48$ and 360° in ϕ. The crystals are grouped in arrays of 2×5, called submodules, then 400 or 500 submodules compose a module and finally a supermodule contains 4 modules. Each half of the barrel groups 18 supermodules, summing up to 61,200 crystals in the ECAL barrel. The endcaps cover $1.48 < |\eta| < 3.0$ and crystals are grouped in supercrystals, composed of 5×5 crystals, arranged in two halves for each endcap in a D-shaped layout, called *Dee*.

Attached to the $PbWO_4$ crystals are the photodetectors, responsible for detecting the emitted light by the crystals when particles pass through it. Moreover, the photodetectors must amplify the signals since the amount of scintillating light is small. Such detectors must tolerate high doses of radiation, be fast on the signal processing, and must operate properly under the longitudinal 3.8 T magnetic field. Due to the different levels of radiation and magnetic field, two types of photodetectors are used in the ECAL: avalanche photodiodes (APDs) in the barrel and vacuum photodiodes (VPTs) in the endcaps. APDs have an active area of 5×5 mm^2 and are mounted in pairs at each crystal. In addition to sensitivity to the scintillating light of the crystals, the photodetectors must be insensitive to particles traversing crossing them (nuclear counter effect), the APDs' sensitivity to particles traversing it is equivalent to 100 MeV deposited in the $PbWO_4$. VPTs have lower quantum efficiency and gain of the signals, but have larger active areas, 280 mm^2.

4.3 Hadronic Calorimeter

While the ECAL is an homogeneous calorimeter, meaning that all of its volume is composed of active medium sensitive to particles traversing it, the Hadronic Calorimeter (HCAL) is a sampling calorimeter. So, instead of only active medium

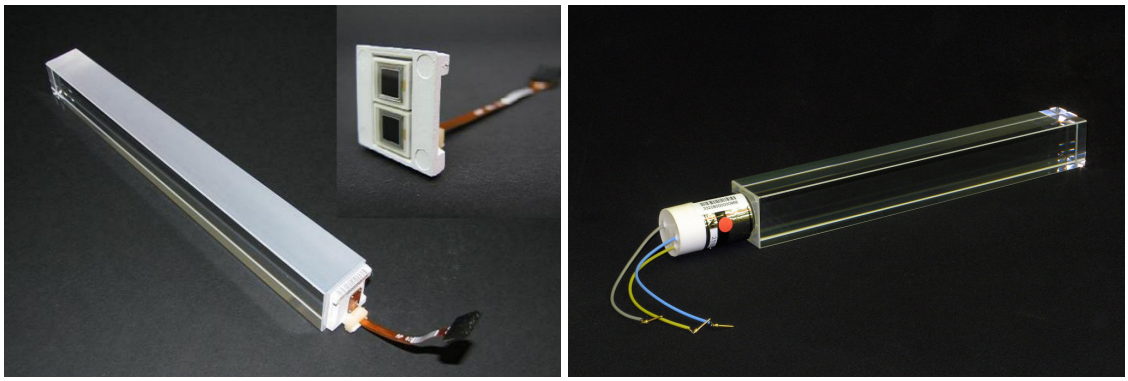

Figure 4.7: Electromagnetic calorimeter photodetectors mounted on the $PbWO_4$ crystals. In the left panel an avalanche photodiode (ADP), present in the ECAL barrel, and in the right panel a vacuum photodiode(VPD), used in the ECAL endcaps. Retrieved from [119].

it also has absorber layers, but it is important to notice that both calorimeters are hermetic. The HCAL is divided in four major sections: the HCAL Barrel (HB) covering the pseudorapidity range $|\eta| < 1.3$; both calorimeter Endcaps (HE) cover $1.3 < |\eta| < 3$; the Outer calorimeter (HO) also covers the central region, ensuring that better containment of hadron jets in $|\eta| < 1.3$ and the Forward HCAL (HF) experiences the highest particle fluxes placed in the region of $3 < |\eta| < 5$.

Sampling calorimeters are classified according to their active medium, and HCAL uses different materials for different purposes of the subdetectors [129]. HB and HE use scintillation sampling calorimeters with plastic scintillators (organic active medium) and brass plates as the absorbers. The Outer calorimeter, which has the function to detect the tail of showers escaping the HB module, uses the same active material as the HB and HE, but as the absorber it uses the steel return yoke and magnet material of the CMS [130]. HF is a Cherenkov calorimeter and uses radiation hard components, by the necessity to survive the harsh conditions of its location: steel as absorbers and quartz fibers as the active medium. It can measure hadronic jets of energies up to the TeV scale by detecting the Cherenkov light emitted by the particles in the quartz fibers.

4.4 Muon Detector System

The outermost subdetector of CMS is the Muon Detector System, a spectrometer specialized in muons detection and reconstruction due to this particle importance in the experiment. The high mass of muons – $\sim 106\,\text{MeV}$ – implies in very

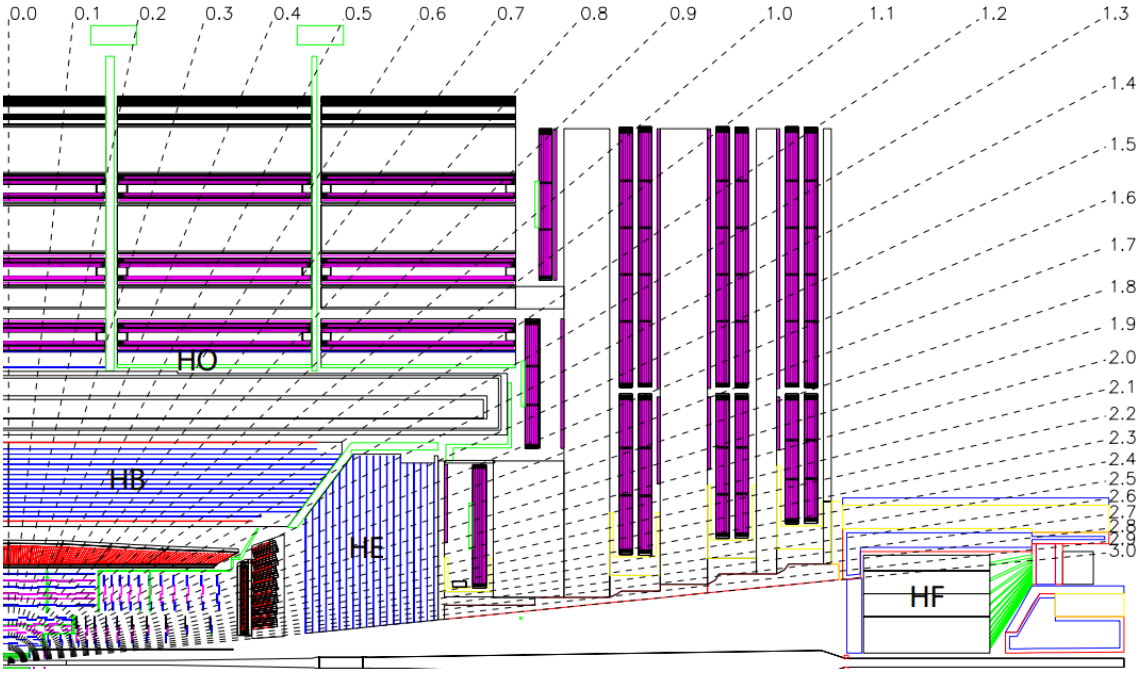

Figure 4.8: Layout of the hadron calorimeter with constant pseudorapidity lines, retrieved from [119].

low loss of energy due to Bremsstrahlung radiation, and since it is a lepton it is not stopped in the HCAL. Its mean lifetime of $\sim 2\,\mu$s allows the particle to travel enough to reach the outer layers of the CMS detector in the typical energies of the collisions. Muons play a fundamental role in the Higgs bosons detection through the decay channel $H \to ZZ/ZZ^* \to 4\mu$, known as *golden plate events*.

The detector is divided in two regions: the barrel region, covering $|\eta| < 1.2$, and two identical endcaps in $1.2 < |\eta| < 2.4$. It uses gas ionization to detect muons position and reconstruct its momentum and trajectory with three distinct detectors:

- Drift Tubes (DT): these detectors are used in the barrel region, where the magnetic field is generally uniform and below 0.4 T. The DT cells have an anode wire traversing it and cathode strips on the walls, such that when a muon travels through the ionized gas, the electrons generated are captured in the electrode strips and the position in the plane perpendicular to the wire can be determined.

- Cathode Strip Chambers (CSC): used in the endcaps, where a non-uniform magnetic field up to 3 T can be encountered. CSC are multiwire chambers, composed of 6 anode wires and 7 cathode panels interleaved [119]. When the

charged particle pass through the chamber, an avalanche is created relative to one of the wires, but charges are induced in every cathode plates, thus allowing the localization of the particle.

- Resistive Plate Chambers (RPC): RPCs are fast dedicated muon detectors, installed both on the barrel and the endcaps. These detectors can tag the time of an ionising event in less than 25 ns, the time gap between two consecutive bunches crossing, although their spatial resolution is lower than DTs and CSCs. The RPCs consist of two parallel plates made of a high resistivity material with a gaseous mixture between the plates. A passing muon creates an avalanche of electrons that are detected in metallic strips that surround the chambers.

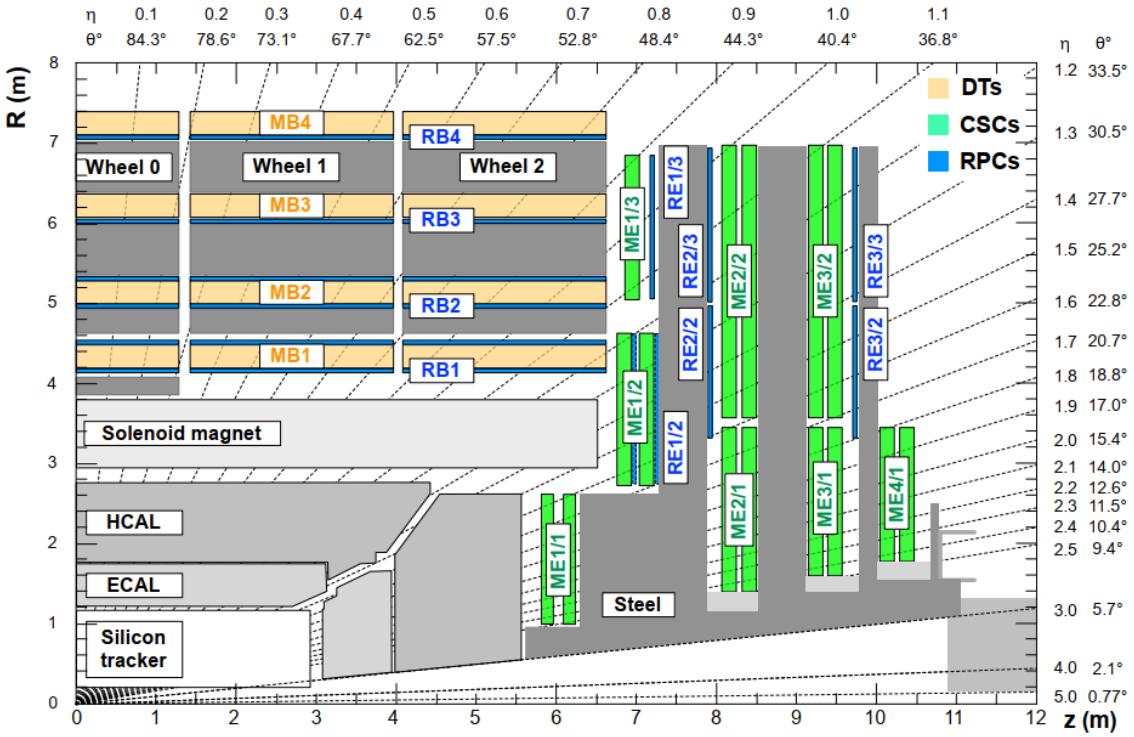

Figure 4.9: Layout of a quadrant of CMS detector, with the Muon Detector's design and location of DTs, CSCs and RPCs.

4.5 Precision Proton Spectrometer

The Precision Proton Spectrometer (PPS) [131] is, after joining with the TOTEM collaboration, a subdetector of CMS. It has been active since 2016 and searches

for central exclusive production (CEP) events, $pp \rightarrow pXp$ where X is produced at central rapidities, while the protons do not dissociate and do not leave the beam pipe, carrying a fraction of its initial momentum. In order to reconstruct such events, the magnetic spectrometers are placed in very forward regions on both sides of CMS, located at $\sim$ 210 m from the interaction point (IP5). PPS consists of proton silicon strip trackers (approximately 4 cm^2 coverage in each arm) and timing detectors (reaching a stable time resolution of 10 ps so far), allowing full kinematic reconstruction of X, by efficiently reconstructing the proton' tracks, masses and momentum, as well as the longitudinal coordinate (z) of the production vertex, aiding the pileup rejection.

The Tracker's detectors are inserted horizontally into the beam pipe in *Roman Pots* (RPs), movable devices that enable the tracker to stay a couple mm away from the beam pipe, while not interfering with other aspects of the accelerator. The layout of PPS detectors is shown in Figure 4.10, the horizontal box-shaped RPs are equipped with the Tracker's detectors at 203.8 m and 212.6 m from IP5, and its strip sensors provide spatial resolution of about 12 μm [132]. In total, PPS uses 144 pixel readout chips and $\sim$ 200 timing readout channels.

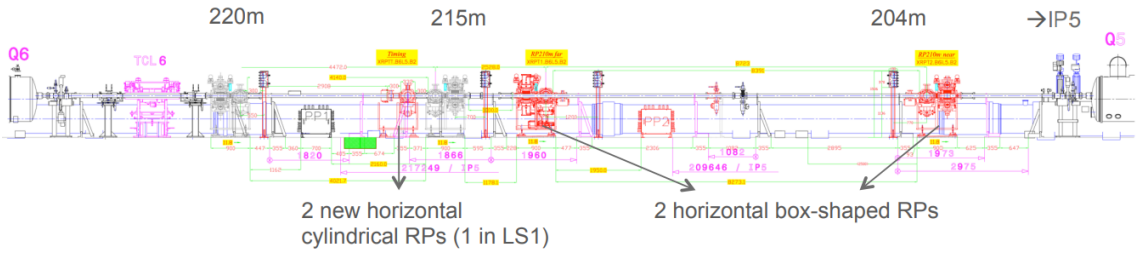

Figure 4.10: Layout of the PPS detectors in the 210 m region after it was installed in 2016 during long shutdown 1 (LS1). Timing detectors are placed in the cylindrical Roman Pots, while the box-shaped Roman Pots (RPs) are equipped with pixel detectors to reconstruct proton trajectories and measure its displacement with respect to the beam. Retrieved from [131].

PPS setting allows the search of CEP events with the invariant X mass in the range of 350 GeV to 2 TeV (an upgrade of PPS for the HL-LHC will probably extend this windows to 50 GeV until 2.7 TeV [133]) when both protons are detected in the arms. In the scope of CEP events, PPS can shed light to better understand SM processes, involving the production of jets, $W^{\pm}$ and Z^0 bosons, the Higgs boson, and also in a wide variety of direct and indirect BSM searches [133]. In particular, the use of forward protons has been proposed to perform searches of missing momentum recoiling against the protons [134], a possible direct detection

of Dark Matter production. Figure 4.11 shows schematics production channels of BSM particles that leave no signal in CMS subdetectors.

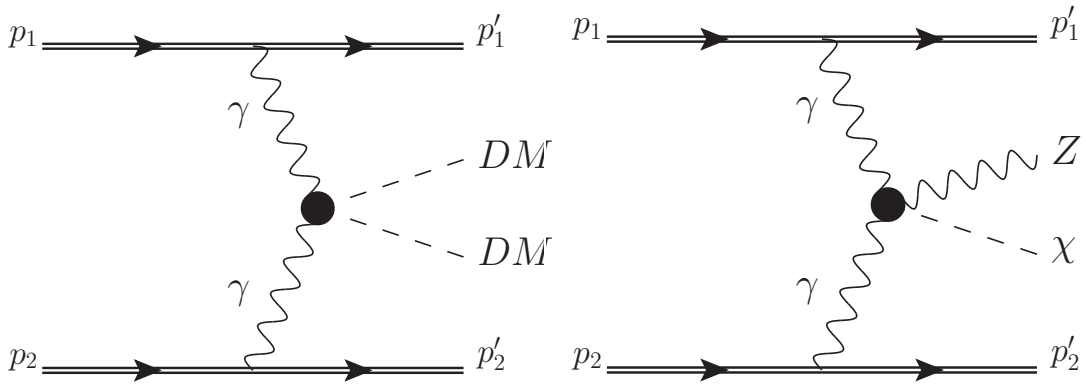

Figure 4.11: Diagrams of central exclusive production of dark matter particles (left) and a invisible particle associated with a Z boson (right).

4.6 Trigger System

With the LHC pp collisions reaching up to $\sqrt{s} = 13\,\text{TeV}$ and luminosity at the order of $2 \times 10^{34}\text{cm}^{-2}\text{s}^{-1}$, the collisions rate exceeds 1 GHz, an extremely high amount of data to be processed and stored. The *trigger system* is responsible for selecting, from all the detected pp interactions, which events are physically relevant to be stored for further analysis, reducing the rate of data acquisition from the GHz scale to kHz [135], a selection reducing 5 orders of magnitude of the frequency.

To accomplish this tremendous task, the trigger is divided in two stages: *Level-1 Trigger* (L1) and *High-Level Trigger* (HLT). The L1 Trigger is implemented in hardware using FPGA technology and reduces the output rate to a maximum of 100 kHz, a rate reduction of $\sim 10^3$, to the HLT. L1 uses energy deposits in the calorimeter trigger towers as well as hit patterns in the muon chambers to select events including objects such as electrons, photons, jets or missing transverse energy. The informations from the different subdetectors are first analyzed separately and if they pass adjustable constraints are evaluated together in the *global trigger* (GT) that decides if the event should be accepted and passed to the HLT, all this within 4 μs after each collision.

The HLT refines further the selection of events using the full precision of the data collected by the detectors and reconstruction algorithms similar to those

developed for offline usage, reaching an output rate of a maximum of 1 kHz[2] [136] for offline storage. The HLT runs in a computing center located near the CMS detector, known as *High-Level Trigger Farm*, containing approximately 13,000 CPU cores, spending about 175 ms per event [135].

4.7 Event Reconstruction

As can be seen in Figure 4.3, different types of particles interact in different way with the CMS detector. In this way, particles generate diverse signatures that are taken into account when the events are reconstructed:

- Muon: Being a charged particle, a track is expected in the Silicon Tracker and in the Muon Chambers;
- Electron: A track is expected in the Silicon Tracker, an energy deposit in the ECAL compatible with the direction of the track, with no deposits in the HCAL or tracks in the Muon Chambers;
- Charged hadron: A track associated with deposits of energy in the ECAL and HCAL is searched, but no signals in the Muon Detector;
- Neutral hadron: An energy cluster in the HCAL, but neither associated tracks in the Silicon Tracker and Muon Chambers nor energy deposits in the ECAL;
- Photon: Energy cluster in the ECAL and no more signals in the other detectors.

Neutrinos and exotic non-interacting particles are not directly detected in the CMS, their presence is inferred from the *missing transverse momentum* of the event (Section 3.4). After the event is reconstructed, since the protons have very little momentum in the $\rho - \phi$ plane, the sum of the transverse momentum after the collision must sum up to 0, with an associated uncertainty. If the sum of the transverse momenta of the reconstructed particles gives a different value, there is a missing momentum that can be attributed to neutrinos[3], as well as exotic non-interacting particles beyond the Standard Model predictions.

[2] Although the estimates were that the output of HLT should be at maximum 400 Hz, the increasing processing power of CPUs available in the market exceeded the expectations, allowing a storage rate of 1 kHz.

[3] In the case of neutrinos, statistical estimates can be calculated based on the processes detected in CMS directly to infer the amount of neutrinos are expected to be present in the event.

The events' reconstruction is performed using information from all subdetectors and is always trying to balance *background rejection*, *efficiency* and *reconstruction time*. Background rejection is important since we cannot store every event generated in the collider, requiring a selection of the most interesting ones, the role of the Trigger System. Efficiency and reconstruction time are deeply related, in principle we can reconstruct almost all particles of all events, achieving close to 100% efficiency, but it costs a lot of processing time. When analyses are performed by the CMS collaboration, the events are reconstructed offline with stored collision data. However, when the Trigger System is running online, while the experiment is taking data, the event reconstruction time is strictly limited, the latency budget at the L1 Trigger is 4 μs and at the HLT it is 175 ms, thus requiring a balance of efficiency, background rejection and reconstruction time.

To reach all these needs, all subdetectors of CMS must be fast and efficient. In particular we focus this project in studying the role of the Tracker System in event reconstruction, specifically to reconstruct and identify disappearing tracks' signatures.

Chapter 5

Track Reconstruction Basics

At particle detectors we can not detect dark matter directly, since they do not interact through electromagnetism nor by nuclear interactions. We can obtain an approximation of the expected flux of dark matter in the collider as indicated by Profumo [72]. First we find an expression for the flux of dark matter in the LHC assuming an isotropic production, at distance R, as a function of the total cross-section of the dark matter pair production $\sigma_{LHC} = \sigma\,(pp \to \chi\chi \to \text{anything})$, where χ is a dark matter particle.

Recalling the expression which relates the number of interactions per second dR/dt and the luminosity of the colliding beams[1]

$$\frac{dR}{dt} = \mathcal{L}\sigma_{LHC}, \tag{5.1}$$

where R is the number of collisions (thus dR/dt the number of collisions per unit time). Our calculation is relative to the reaction $pp \to \chi\chi \to$ anything, so for each collision we get two DM particles χ. And as we are considering an isotropic flux of DM

$$\begin{aligned}
\Phi_{\chi(LHC)} &= \frac{\#\chi}{\Delta t \cdot \Delta A} \\
\Phi_{\chi(LHC)} &= (2\mathcal{L}\sigma_{LHC})\,\frac{1}{4\pi R^2} \\
\Phi_{\chi(LHC)} &= \frac{\mathcal{L}\sigma_{LHC}}{2\pi R^2}.
\end{aligned} \tag{5.2}$$

where $\Phi_{\chi(LHC)}$ is the flux of DM at the LHC, Δt is the time interval and ΔA the area being considered to calculate the flux in the detector.

Assuming $m_\chi = 100\,\text{GeV}$, a weak-interaction cross section $\sigma_{LHC} = G_F^2 m_\chi^2$ and the expected peak instantaneous luminosity of the HL-LHC $\mathcal{L} = 5 \times 10^{34}\text{cm}^{-2}\text{s}^{-1}$

[1] Particle Colliders and Concept of Luminosity

$$\Phi_{\chi(LHC)} = \frac{\mathcal{L}\sigma_{LHC}}{2\pi R^2}(\hbar c)^2 = 4.6 \times 10^{-6}\text{cm}^{-2}\text{s}^{-1}.$$

The galactic flux of dark matter at Earth assuming its density $\rho_{DM}(r) = 0.3\,\text{GeV}/\text{cm}^3$ and $v = 220\,\text{km/s}$ the velocity at which the planet, and the Solar System, orbits around the center of our galaxy, the Milky Way:

$$\Phi_{\chi(Galactic)} = \frac{\rho_{DM}(r) \cdot v}{m_\chi} = 6.6 \times 10^{4}\text{cm}^{-2}\text{s}^{-1},$$

comparing both fluxes, we conclude that

$$\frac{\Phi_{\chi(LHC)}}{\Phi_{\chi(Galactic)}} \approx 10^{-10}$$

a negligible low flux, even if we were considering that our detector had the adequate apparatus to detect dark matter particles, would be hopeless to search for dark matter produced in our collider if the spectrum of galactic DM is similar to the collisions generated fluxes.

In the scope of this project, we search specifically for dark matter produced together with long-lived particles (LLP). One possible sign of a dark matter + charged LLP signature can be a reconstructed charged particle (a track) recoiling against undetected particles in the detector; another possible signature that can be related to dark matter + LLP is the detection of a displaced vertex, representing the decay of a neutral LLP (Figure 5.1). In the transverse plane of the collision, the beamspot (the reconstructed region where the proton beams collide throughout the Runs) is of the order of μm away from the reconstructed vertex. For smaller distances, the experimental signal becomes harder to distinguish from background b quark jets.

5.1 Kalman Filter

Tracks are reconstructed at CMS through an algorithm based on the Combinatorial Kalman Filter (CKF) called *Iterative Tracking*. The main idea of it is to reconstruct first easier to track particle trajectories such as high-p_T prompt tracks and ignore the associated hits in the next iteration. That way we reduce the complexity of reconstruction of tracks of low p_T and with displaced vertex [137].

In 1960 R.E. Kalman published a paper named *A New Approach to Linear Filtering and Prediction Problems* [138] in which he presents a recursive solution to the

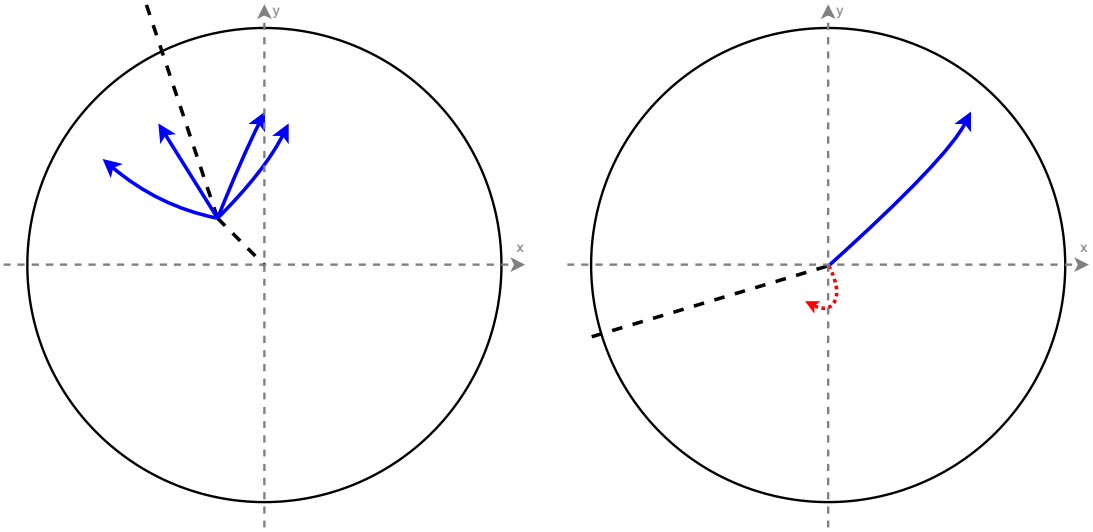

Figure 5.1: Schematic representation of signatures of long-lived particles in the CMS detector. The left panel shows a neutral LLP (dashed black) decaying to charged particles (blue), producing a displaced vertex; the right panel a charged particle (blue) recoiling against a neutral LLP (dashed black) and a low momentum charged particle (red) that is not detected.

discrete-data filtering problem. This work revolutionized the control theory field and since then has been implemented in myriad problems, from aerospace [139, 140] to finance [141], with an excellent record of successes. At the CMS experiment we have another example of Kalman filter implementation, regarding particle tracks finding and fitting problems.

In practice, we can think of the Kalman Filter as a weighted averaging procedure that has a smaller error than both our measurements and predictions separately.

5.1.1 Definition

From what follows the discussion and derivation of the Kalman Filter, I follow the structure of Gelb's book [142]. Consider a discrete linear dynamic state given by state vectors $\hat{x}_k$,

$$x_k = \mathbf{\Phi}_{k-1} x_{k-1} + v_{k-1} \tag{5.3}$$

where the subindex k indicates the time t_k being considered, $\mathbf{\Phi}_{k-1}$ indicates the matrix of our dynamic model, which relates a posterior state vector to its previous one, and v_{k-1} is a white sequence (random, uncorrelated sequence with zero mean) of covariance $\mathbf{Q}_{k-1}$.

Measurements z_k are taken as linear combination of the state vectors with intrinsic uncorrelated noise, and we write

$$z_k = \mathbf{H}_k x_k + w_k \tag{5.4}$$

where $\mathbf{H}_k$ is the measure matrix at a time t_k and $\hat{w}_k$ another uncorrelated noise variance (zero mean and covariance $\mathbf{R}_k$) corrupting the measurements.

The Kalman filter procedure takes place in two different steps. The first one is the *Prediction Step* and it will predict the forward state vector estimate $\hat{x}_{k+1}(-)$, also called the *prior* estimate; the subsequent is the *Update Step* uses the measurements to enhance the state vector prediction to $\hat{x}_{k+1}(+)$. These steps are done in the following linear recursive way

$$\hat{x}_{k+1}(+) = \mathbf{K}'_{k+1}\hat{x}_{k+1}(-) + \mathbf{K}_{k+1}\hat{z}_k$$

where the matrices $\mathbf{K}'_{k+1}$ and $\mathbf{K}_{k+1}$ are updated at every step. If we impose $\hat{v}_k$ and $\hat{w}_k$ to be gaussian the Kalman filter is *the optimal filter* to the problem. Otherwise, it is the optimal linear filter [138].

Now if we set the expected value of $\mathrm{E}[w_j v_k^T] = 0$ for all j, k it is possible to derive the Kalman filter by optimizing the assumed form of the linear estimator [142]. We can summarize the Kalman filter, under the assumptions made above, as a describing model given by Equation 5.3 and 5.4 with initial conditions given by the expected values $\mathrm{E}[x(0)] = \hat{x}_0$ and $\mathrm{E}[(x(0) - \hat{x}_0)(x(0) - \hat{x}_0)^T] = \mathrm{P}_0$, the Prediction Step is

$$\begin{aligned} \hat{x}_k(-) &= \Phi_{k-1}\hat{x}_{k-1}(+) && \text{(State Estimate Extrapolation)} \\ \mathrm{P}_k(-) &= \Phi_{k-1}P_{k-1}(+)\Phi_{k-1}^T + \mathbf{Q}_{k-1} && \text{(Error Covariance Extrapolation)} \end{aligned}$$

and the Update Step

$$\begin{aligned} \hat{x}_k(+) &= \hat{x}_k(-) + \mathrm{K}_k[z_k - \mathbf{H}_k\hat{x}_k(-)] && \text{(State Estimate Update)} \\ P_k(+) &= [1 - \mathbf{K}_k\mathbf{H}_k]P_k(-) && \text{(Error Covariance Update)} \\ \mathbf{K}_k &= P_k(-)\mathbf{H}_k^T[\mathbf{H}_k P_k(-)\mathbf{H}_k^T + \mathbf{R}_k]^{-1}. && \text{(Kalman Gain Matrix)} \end{aligned}$$

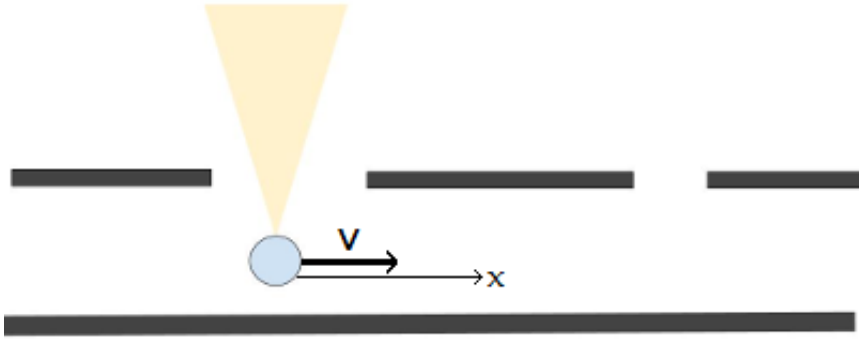

Figure 5.2: Robot travelling in a corridor taking measurements of its position.

5.1.2 Simple 1D Implementation

In order to better understand the core principles of the Kalman filter and the guidelines to implement it, consider for example a robot travelling through a straight corridor, with an approximate constant velocity $\vec{v} = (1\,\mathrm{m/s})\vec{n}$ ($\vec{n}$ is a versor in the direction of the motion). *A priori* we have a completely determined state vector representing our particle given by its position at any time t. We can write it as $\vec{x}(t) = \vec{v}(t)\Delta t$ where Δt is the elapsed time since the particle was at the origin of our coordinate system, and its constant velocity $\vec{v}(t) = \vec{v} = (1\,\mathrm{m/s})\vec{n}$. But when we are considering a real system we will always have an error associated with our description of the actual physical state and its properties.

As the robot travels in the corridor it takes measurements of its position (relative to the origin where we set its position and time equal to 0) every second, and of course they will also have an error associated with them. So, once we have gathered the measurements of the robot we can implement the Kalman Filter. What we are looking for in this problem is to obtain a function of the time that will return the position of the robot at a given time $x(t)$. From our knowledge of the experiment we construct a prediction $\hat{x}(t)$ representing what we expect to happen based on our *ansatz*: the robot starts at position $x(t = 0) = 0$ and travels at constant velocity $v = 1\,\mathrm{m/s}$. Together with our prediction remember we also have an associated error $h(t)$. And from our robot sensor we obtain measures of its position $z(t)$ with its error $r(t)$.

Using the derivation from the Prediction and Update of Subsection 5.1.1 steps can be written as follows:

Prediction

$$x_t = x_{t-1} + v\Delta t \qquad \text{(Predicted state estimate)}$$
$$h_t = h_{t-1} + \Delta t^2 \cdot h_t^v + q_t \qquad \text{(Associated uncertainty)}$$

Update

$$k_t = \frac{h_t}{h_t + r_t} \qquad \text{(Kalman gain)}$$
$$x_t' = x_t + k_t(z_t - x_t) \qquad \text{(Updated state estimate)}$$
$$q_t' = p_t(1 - k_t) \qquad \text{(Updated uncertainty of the state estimate)}$$

the subscript t represents the value of the variables at time t, meaning the same as (t) ($x(t) = x_t$), and their definitions are:

- x_t Predicted state estimate
- v_t Velocity
- Δt Time interval between two steps
- h_t Uncertainty of the predicted state estimate
- h_t^v Uncertainty of the velocity estimate
- q_t Process Noise Variance
- z_t Observation/measurement of the true state of x_t
- r_t Measurement uncertainty
- k_t Kalman gain
- x_t' Updated state estimate
- h_t' Updated variance of the state estimate

The Prediction Step is composed of two simultaneous parts. The *predicted state estimate* is simply our linear model of propagation at constant velocity, the previous position x_{t-1} plus the travelled distance until the prediction $v\Delta t$. The *associated uncertainty* sums the uncertainty to the previous position h_{t-1} with the process noise variance q_t, intrinsic uncertainties of the model [143], and the expectation of variance $\Delta t^2 \cdot h_t^v$.

To obtain the expectation of variance we use the definition and properties of the expectation E and the variance V of a random value X [144]:

$$E(X) = \mu_X \qquad V(X) = E(X^2) - \mu_X^2$$

μ_X being the mean value of X. Using the linearity of the expectation together with our model's position function $x(t) = v\Delta t$ we get to the result:

$$\begin{aligned}
E(V(x)) &= E(E(x^2) - \mu_x^2) \\
&= E(E(v^2\Delta t^2) - \mu_x^2) && (v \text{ and } \Delta t \text{ are constant}) \\
&= E(v^2\Delta t^2 - \mu_v^2\Delta t^2) && (x = v\Delta t \Leftrightarrow \mu_x = \mu_v\Delta t) \\
&= \Delta t^2(v^2 - \mu_v^2) \\
&= V(v^2)\Delta t^2 \\
E(V(x)) &= \sigma_{v^2}\Delta t^2 \equiv h_t^v \Delta t^2.
\end{aligned}$$

Moving forward to the Update Step, the *Kalman gain* acts as a weighted average of the system's prediction and measurements, which will encode the Filter's degree of "trust" in the data. $k_t \approx 1$ means less uncertainty in the prediction, $r_t \ll h_t$, therefore trusting more the measurements; on the other han $k_t \approx 0$ means less uncertainty in the measurements, $h_t \ll r_t$ and conversely the Filter trusts the predictions more. Being a weighted average implies that the Filter will always put its final state someplace between our prediction and measurement, in general being more accurate with respect to the physical state.

The last two steps of the Update step consist in implementing the average we just talked about to the position and uncertainties, respectively to *Update of the state estimate* and *Update uncertainty of the state estimate*. We can check explicitly that the Kalman gain values being 1 recovered trusting in measurements and 0 trusting the predictions.

Back to the robot, to illustrate how these concepts tie together and appear on the Kalman filter implementation let's look at how the prediction, measurement and the final updated position after using the filter behave. Since this serves only as an example to develop some intuition of what happens in a Kalman filter I will use synthetic data.

First I will define $H_t = \Delta t^2 \cdot h_t^v + q_t$ a "total" error of our prediction and give it a high value of $0.5 \rightarrow 50\%$ *error*. I will also suppose our measurements have a high noise of $r_t = 0.25 \rightarrow$ *25% error.* The output of this scenario is shown in

Figure 5.3 analyzing 5 measurements of the robot and the respective predictions and filtered results. Table 5.1 contains the data described above.

Time (s)	Prediction (m)	Measurement (m)	Kalman (m)
1	0.97 ±0.50 m	1.11 ±0.25 m	1.06 ±0.17 m
2	2.17 ±0.67 m	2.09 ±0.25 m	2.11 ±0.18 m
3	3.23 ±0.68 m	2.81 ±0.25 m	2.92 ±0.18 m
4	4.30 ±0.68 m	4.20 ±0.25 m	4.22 ±0.18 m
5	5.15 ±0.68 m	4.80 ±0.25 m	4.89 ±0.18 m

Table 5.1: Time and the respective predictions, measurements and the Kalman filtered positions.

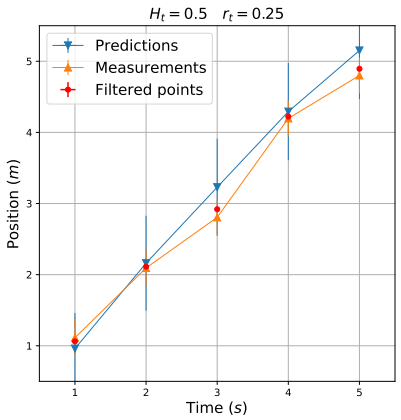

Figure 5.3: 1D Kalman filter for predictions with $H_t = 0.5$ and noisy measurements with $r_t = 0.25$. The blue points are the model predictions, the orange points are the measurements, and the red points are the filtered (prediction+measurement) results.

It can be seen explicitly in the figure that the red dots (Kalman filtered points) appear in between the predictions and the measurements, giving as result a "smoother" curve tracing the filtered points (and as already stated a more reliable description of the real physical system).

Similarly to the 1D Kalman filter implementation, we can extend it to 2D, assuming independent dynamics of the system in these dimensions, simply calculating the *prediction* and *update* steps for each coordinate.

5.1.3 Implementation for Curved Trajectories

When we are dealing with charged particles in the Tracker we willl have curved, circular trajectories in the transverse plane to the collision due to the Lorentz force.

The dynamical equations of motion are then derived as follows:

$$\begin{aligned} \frac{d\vec{P}}{dt} &= q(\vec{v}\vec{B}) && \text{(Lorentz Force)} \\ \frac{d(\gamma m\vec{v})}{dt} &= q(\vec{v}\vec{B}) \\ \frac{d\vec{v}}{dt} &= \left(\frac{q}{\gamma m}\right)(\vec{v}\vec{B}) \\ \frac{d\vec{v}}{dt} &= K(\vec{v}\vec{B}) && (K = \tfrac{q}{\gamma m}) \end{aligned}$$

where $\vec{B}$ was taken out of the time derivative since $\gamma(\vec{v}(t)) = \gamma(v^2)$ and v^2 is constant once the magnetic field only changes the particle direction. Expressing it explicitly in polar coordinates, the natural choice when dealing with the cylindrical symmetry of the CMS detector

$$\begin{aligned} \frac{d\vec{v}}{dt} &= K(\vec{v}\vec{B}) \\ (\ddot{r} - r\dot{\phi}^2)\hat{r} + (r\ddot{\phi} + 2\dot{r}\dot{\phi})\hat{\phi} &= K\left[(r\dot{\phi}B)\hat{r} - (\dot{r}B)\hat{\phi}\right]. \end{aligned}$$

When equalling both sides we end up with two differential coupled equations, the solution of which gives the dynamics of our charged particle. We solve it numerically with the *5th and 4th order Runge-Kutta* algorithm (RK-45)[2]. The equations must be written as an Initial Value Problem to do so

Master equations for particle propagation

$$\frac{d\dot{r}}{dt} = r(\dot{\phi}^2 + KB\dot{\phi}) \qquad \frac{dr}{dt} = \dot{r} \tag{5.5}$$

$$\frac{d\dot{\phi}}{dt} = (-\dot{r})\frac{(2\dot{\phi} + KB)}{r} \qquad \frac{d\phi}{dt} = \dot{\phi} \tag{5.6}$$

$$r(0) = r_0, \quad \phi(0) = \phi_0, \quad \dot{r}(0) = \dot{r}_0, \quad \dot{\phi}(0) = \dot{\phi}_0$$

where $r_0, \phi_0, \dot{r}_0, \dot{\phi}_0$ are the initial conditions of the problem. In our case we will consider it at the origin of the coordinate system, where the bunches would cross.

For the purpose of our implementation, instead of simulating the whole CMS detector, we instead consider a simplified ("toy") detector model with only cylindrical layers, and consider only motion in the transverse plane of the detector.

[2]The function scipy.integrate.RK45 from SciPy was used.

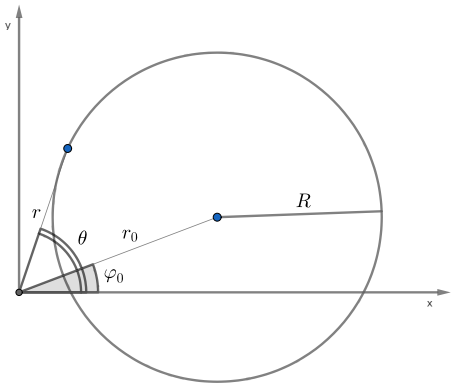

Figure 5.4: Circle of radius R with center at (r_0, φ_0) and a point of the circle at (r, θ).

Our toy detector is composed of 10 concentric layers, with distance of 1 cm from each other. To simulate the detector's uncertainty on detecting the hits, we generate the tracks, at a given ϕ, and perturb their ϕ coordinate. Figure 5.5 shows a representative set of hits after reconstruction, where initial conditions were $r(0) \approx 0, \phi(0) = \frac{\pi}{4}, \dot{r}(0) = 0.99\,\mathrm{c}, \dot{\phi}(0) = 0$ (we can not set $r_0 = 0$ – particles coming from the origin – since it is a pole of the equations of motion, so we set it to a sufficient small number).

After the Kalman filter procedure, we fit the filtered points of the track with a segment of circle passing through the origin, using the *least squares* method, and the correspondent radius of the fitted circle is plotted in the legend for each track. The general equation of a circle in polar coordinates with center at (r_0, φ_0) and radius R is given by

$$r^2 + r_0^2 - 2rr_0 \cos(\theta - \varphi_0) = R^2 \quad , \tag{5.7}$$

where (r, θ) is an arbitrary point of the circle.

Since we are working with a toy model, we use another simplification here, setting the origin of our fit in the origin. In the CMS experiment, the interaction point is reconstructed using information of all subdetectors in order to accurately determine the production vertex of the event [145].

This assumption is expressed in Equation 5.7 equaling $r_0 = R$

$$\begin{aligned} r^2 - 2Rr\cos(\theta - \varphi_0) &= 0 \\ \theta = \varphi_0 + \arccos\frac{r}{2R} \quad &. \end{aligned} \tag{5.8}$$

With Equation 5.8 we have a relation between the circle origin (R, φ_0) and the points of the circle, which are in our problem the Kalman positions (the positions calculated by the Kalman filter procedure using the measurements and predictions as inputs) of the track being fitted. In order to determine the circle origin, we used the *least squares* [3] approach, with the Kalman positions as input.

As the initial conditions, for the circle radius R, we use an approximation based on the *sagitta*. From the Pythagorean theorem, we can write

$$
\begin{aligned}
R^2 &= L^2 + (R - s)^2 \\
R &= \frac{s}{2} + \frac{L^2}{2s} \\
s \ll R \rightarrow R &\approx \frac{L^2}{2s} \quad .
\end{aligned}
$$

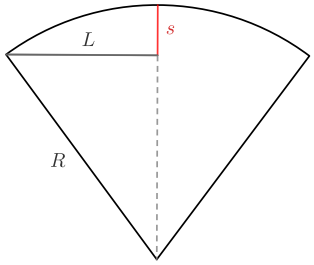

Based on the latter approximation that the track passes through the origin of our coordinate system, we set the value of s as the distance between the fifth hit and the line that passes through the origin and the last track hit.

For the angle φ_0 of the circle, we have different initial conditions depending on the track curvature - clockwise direction when it is a positively charged particle, and anticlockwise when it is a negatively charged particle. When we are fitting a positive charge particle track, the initial condition is set to $\varphi_0 = \frac{3\pi}{2}$, because the data used in this study generates only particles with initial angle in the interval $0 < \phi < \pi/2$ (Subsection 5.2). When it is a negative charge particle track, the initial condition is $\varphi_0 = \frac{3\pi}{4}$.

To test our solution, we implemented the Kalman filter with the dynamical Equations 5.5 and 5.6, and the fitting procedure, using simulated data of particles (pions) with $p_T = 0.9\,\text{GeV}, m = 0.14\,\text{GeV}, q = \pm 1$ in a magnetic field of $B = 20\,\text{T}$ transverse to the plane of collision.

5.2 Data Set

1,000 events were generated to test our implementation, containing 15 pion tracks (with $\phi \in (0, \pi/2)$ in order to simplify the fitting implementation) generated at the origin of the coordinate system each. From its production vertex the trajectory of the particle is calculated using the dynamical equations of motion.

[3] Implemented with `SciPy`'s function `scipy.optimize.least_squares`.

Since we have their trajectories determined: the positions with radius (in polar cylindrical coordinates (r, ϕ, z)) $r = 1\,\text{cm}, 2\,\text{cm}, ..., 10\,\text{cm}$, where the detectors are located, are selected.

Our interest is in the transverse plane, thus we ignore the z axis for now. With the selected positions in the (r, ϕ)-plane we perturb their ϕ coordinate to account for the uncertainty associated to the measurements of the detectors. Considering our ideal detector, with the highest granularity, calibration and alignment, we only use errors in the angular coordinate, for simplicity.

Given the values of mass and transverse momentum fixed for the pions, the radius of curvature of the particles can be calculated through the relation

$$R = \frac{p_T}{0.003qB}$$

for R in cm, p_T in GeV, q in elementary charge and B in T. Once pions have charge $q = \pm 1\,\text{e}$ their tracks should have a curvature of $R = 15\,\text{cm}$.

Implementing the fitting of curved trajectories, and testing it on the database aforementioned for 15 tracks gave the results shown in Figure 5.5. The fitting was validated considering that the fitted tracks have reconstruction radius $R_{found} \sim$ 15cm,

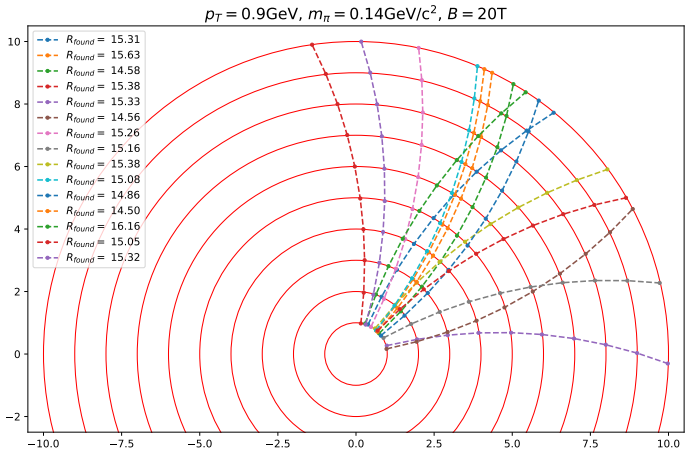

Figure 5.5: Reconstruction of 15 tracks with Kalman filter of simulated measurements with $\sigma_\phi = 0.01$. The legend gives the radius of the circle which fits the tracks and pass through the origin. Both axis and the reconstructed radius are in cm.

5.3 Implementation of Combinatorial Kalman Filter (CKF)

Hitherto, the Kalman filter technique was applied to a set of measurements we had the prior knowledge of knowing to which track each hit belonged. However, assigning hits to its respective particle (track) is part of the event reconstruction at CMS. For instance, the Trigger System (Subsection 4.6) performs a fast tracking of particles, using the events' data acquired by the subdetectors, in order to select interesting events to be stored.

The initial conditions of our problem now will be the positions and associated errors of measurements of all the hits of an event. Our task is to assign correctly the hits that belong to the same particle, thus properly reconstructing the track's parameters. The data used will maintain our previous constraint of the initial angle of the particle tracks between $[0, \pi/2]$, in order to simplify technical issues, and there will be exactly 15 charged particle tracks per event.

Our approach to the problem consists of first: generate *seeds* of positions and velocities, since we write the particle dynamics as an Initial Value Problem, thus requiring initial conditions. In the CMS detector, the Pixel Tracking System, together with information from the Calorimeters, are used to construct track seeds.

Using the seeds as inputs in the dynamical equations, we can calculate the particles' trajectories, predicting in which points it would be detected in the detector's layers. From the tracks generated through this procedure, we expect a subset of them to be the correctly reconstructed particle tracks. Figure 5.6 shows schematically the seed, particle and track in the detector.

5.3.1 Seeds

To create seeds of positions and velocities given the hits of the event, we adopt a procedure inspired by the seed generator, using the first two layer hits, while CMS uses all hits from the pixel tracker. For each hit in the first, and innermost, layer, we trace a straight line passing through the origin and the hit. We then extrapolate the line to the second layer and search for hits near it. In this way, with two hits we define the velocity vector and have the positions to input in the equations of motion.

However, when we extrapolate the line to the second layer, we do not expect that a hit will be found exactly, since we know that charged particles have a curved

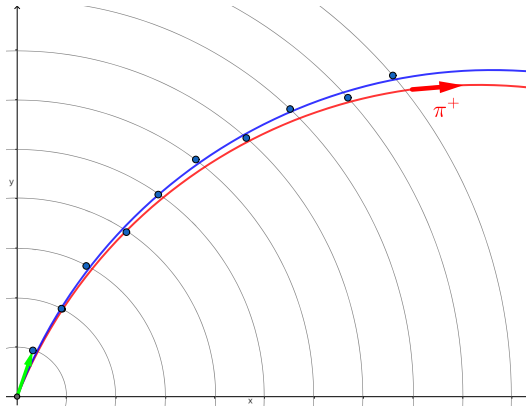

Figure 5.6: In red we have the *particle* (π^+) trajectory which we want to reconstruct, in blue the reconstructed *track*, where the blue dots are the filtered measurements, and in green the *seed*, used as initial condition to generate the particle track.

trajectory inside the detector, and we need to account for the uncertainties both of our prediction and the detector. The way we work around this issue is by defining a tolerance distance from the prediction on the second layer, where it is probable that the hit associated to the same track as the first hit will be encountered. To define properly the tolerance distance, we first calculate the distance between our prediction and the real second layer hits for a dataset of 15,000 tracks. Based on Figure 5.7 the tolerance distance was defined as 0.13 cm, under which the vast majority of the correct hits will be assigned, although in many cases not uniquely the correct ones. Thus, to generate the seeds, the projection to the second layer is made, for each hit on the first layer, and the hits with distance equal or less than 0.13 cm from the projection are used to create seeds and construct tracks.

5.3.2 Propagation and Hits Assignment

Once we have chosen the seeds, using them as inputs to the Equations 5.5, 5.6 we obtain the propagation of the candidate particle throughout the detector, and consequently predictions of where it will hit the detector's layers. The procedure to find hits on subsequent layers is similar to the aforementioned in order to construct tracks' seeds. We set a tolerance distance from the prediction in which we expect to find the correct hit related to the seed. When we proceed to layers further away from the origin, the arc of length of the tolerance interval must be incremented, in order to preserve the accuracy of finding promising hits in such interval. If we do not implement this increment, rarely we find hits up until the final layers of the detector. An increment of 0.05 cm per layer showed an adequate

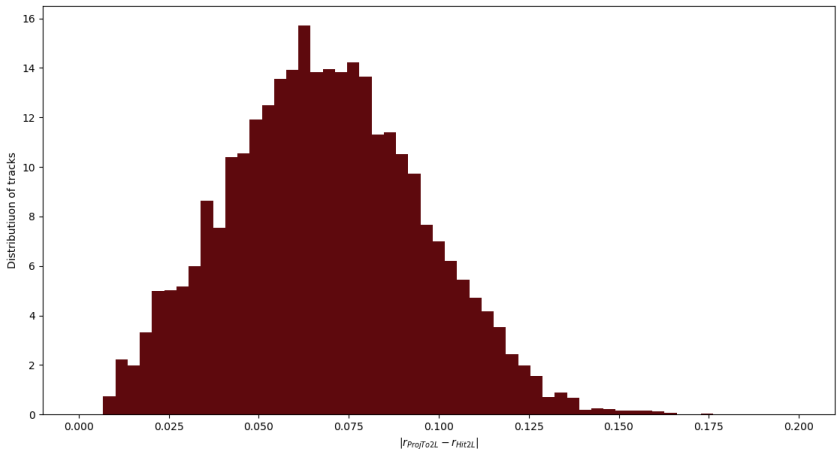

Figure 5.7: Histogram of the distance in cm between the extrapolated position on the second layer and the true hit.

balance of finding hits while not being broad enough to assign wrong hits often.

Another crucial point of the implementation is finding out the charge of the particle, since we do not have this information from the seeds, and the charge determines the curvature of the track. We address this intricacy considering both cases, positive and negative particle tracks. If in one of them the algorithm ceases to find hits before assigning 10 hits, we discard it, assuming that the particle has the opposite charge. If both cases do not find 10 consecutive hits we discard the seed, assuming it is probably a fake seed. In the case where both charges manage to construct a 10-hit track, they are both stored for the time being, but later it will be shown how we select the most promising track based on the track quality.

5.3.3 Tracks Selection

Once we manage to reconstruct tracks with the initial hits of the event, we need to verify that they indeed represent accurately the particle tracks of the event. In order to evaluate the implementation described up to this point, we do so with 1,000 events generated as described in Subsection 5.3. Each event contains 15 pion tracks, summing up to a total of 15,000 pions. Our goal is to reconstruct as many "correct" tracks as possible; a working definition of correctness will be given later in this section.

The set of all reconstructed tracks by our algorithm is denominated *general tracks*, and is composed of 42,444 tracks in our test sample. Our goal is to refine

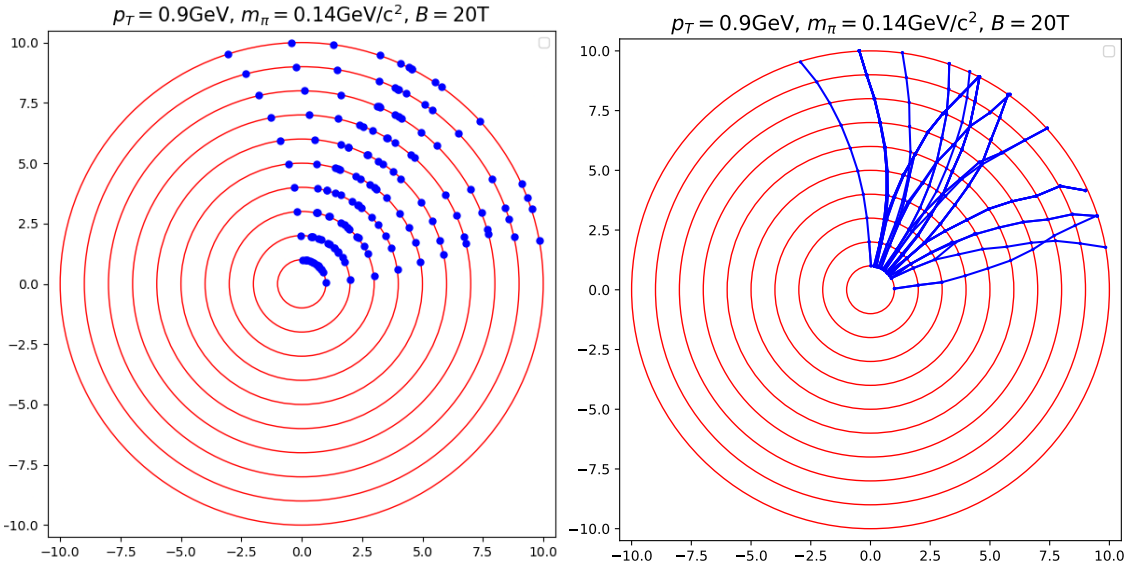

Figure 5.8: The left panel contains the detected hits of the event, input of the CKF algorithm, while in the right panel the reconstructed tracks of the event, the output of the CKF algorithm. Both figures' axis are in cm unit.

this set of tracks, ideally selecting the 15,000 tracks that correspond to the real tracks, achieving 100% of reconstruction efficiency.

To give us an initial estimate of the average number of tracks in an event, and thus guide us in developing a method to refine our selection accordingly, Figure 5.9 shows how many tracks were generated by our implementation of CKF. We can identify a peak of the distribution close to 40 tracks/event, representing roughly three times more reconstructed tracks than the number of real tracks in the event. In this scope, we develop throughout this subsection a procedure to classify and choose the most promising tracks.

A characteristic of the particle tracks that we can use to aid in the evaluation of the χ^2 of the fit. The χ^2 variable is commonly used to verify the agreement between a theoretical hypothesis with experimental data, and is defined as a sum based on the number of degrees of freedom f of the problem as follows

$$\chi^2 = \sum_{i=1}^{f} \frac{x_i^2}{\sigma_i^2}$$

where x_i follows a normal distribution with mean 0 and variance σ_i.

Applying it to the CKF picture, for each track we identify its degrees of freedom with the 10 hits which compose the track. The x_i are then written as the difference between the Kalman positions and the track fit, and thus the variance will be

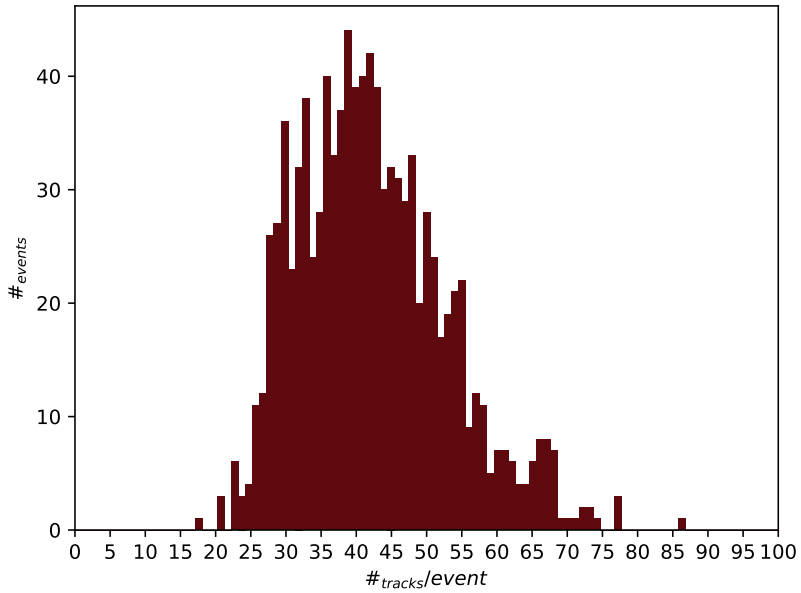

Figure 5.9: Distribution of the number of reconstructed tracks per event, for 1,000 events with 15 pion tracks each. In total 42,444 tracks were generated.

the same as the Kalman positions'. Kalman positions are used since they are better approximations to the particle trajectory than the measurements alone, x_i^{Kalman} averages between the predictions based on our previous knowledge and the measurements made of the trajectory by the detector.

$$\chi^2 = \sum_{i=\text{hits}=1}^{10} \frac{(x_i^{Kalman} - x_i^{Fit})^2}{(\sigma_i^{Kalman})^2} \quad . \tag{5.9}$$

Figure 5.10 shows the χ^2 distribution per track.

In order to verify that the χ^2 variable can be used to tag correct tracks, we can study its correlation with a variable that is intrinsically measuring the quality of the reconstruction. One such variable is the difference in between the angle at which the tracks start from the origin and the fitted track at the same point: $\Delta\phi = |\phi_{Particle} - \phi_{Track}|$. The $\phi_{Particle}$ angle is the true angle of production of the particle in question, and as such is not available to our algorithm while reconstructing tracks through CKF. The $\Delta\phi$ distribution of tracks is shown in Figure 5.11.

One way to visualize the correlation between the two variables is through a 2D histogram with one variable in each axis, as in Figure 5.12. Further, we can calculate the Pearson coefficient, a measure of the correlation between two variables. The coefficient ranges from 1, indicating a linear relation between the

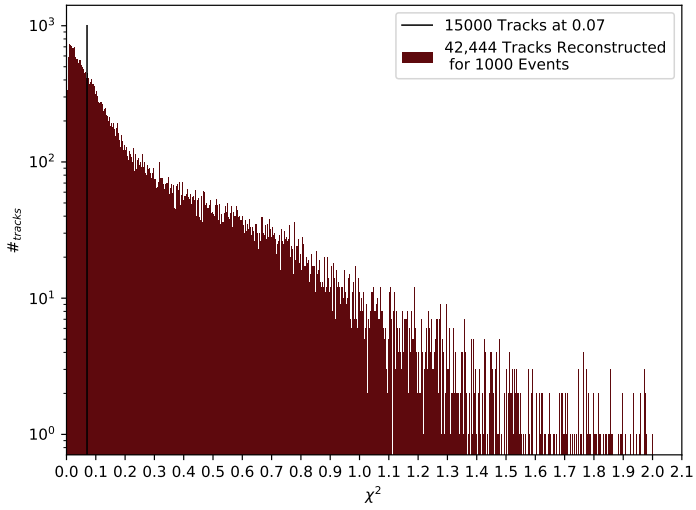

Figure 5.10: Distribution of χ^2 of each track of the total dataset. The vertical black line indicates the first bin (~ 0.07) at which the sum of the previous bins is greater or equal to 15,000 tracks, the total number of particles in the events.

variables, to -1, when the variables are anti-linear, and when it is 0, no linear relation exist between the variables. The Pearson coefficient for two variables A and B is defined as

$$\rho(A,B) = \frac{\text{cov}(A,B)}{\sigma_A \sigma_B} \tag{5.10}$$

where $\text{cov}(A,B)$ stands for the correlation between variables A and B, and σ is the variance of each variable. Calculating the Pearson correlation coefficient for our case, we obtain $\rho(\chi^2, \Delta\phi) = 0.567$, indicating that there is a linear component linking the two variables.

Given this relation, it is reasonable to use the fact that lower values of χ^2 have a tendency of having lower values of $\Delta\phi$, and thus express a more accurately reconstructed track. In this way, we can start developing a simple track selection algorithm based on the χ^2 variable of the tracks. A threshold value in $\chi^2 \sim 0.07$ reflects, in average, a selection of the lowest $\Delta\phi$ tracks generated.

Our first cut in the *general tracks* is related to Figure 5.12 and the discussion above, in which we found out a certain linear correlation between values of $\Delta\phi$ and χ^2. Thus, selecting the 15,000 tracks with lowest χ^2 ($\chi^2 < 0.07$), we call the remaining tracks *High-Purity (HP) tracks*. With this cut we expect to, in general, select tracks with lower values of $\Delta\phi$, and consequently better reconstructed tracks,

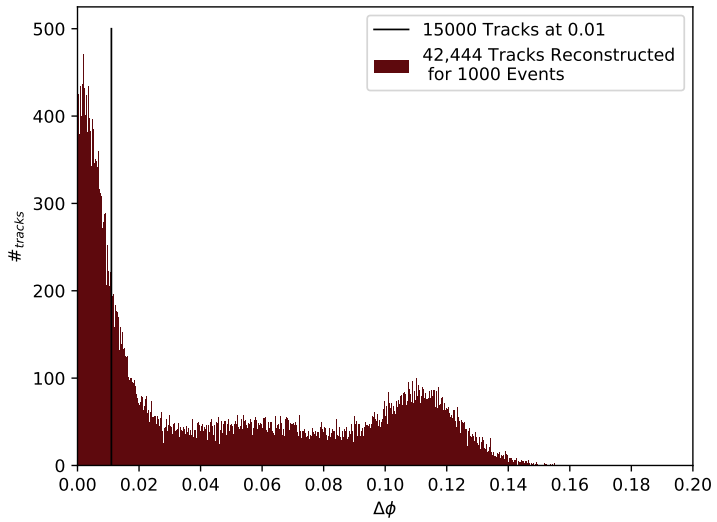

Figure 5.11: Distribution of $\Delta\phi$ of each track of the total dataset. The vertical black line indicates the first bin (~ 0.01) at which the sum of the previous bins is greater or equal to 15,000 tracks, the total number of particles in the events.

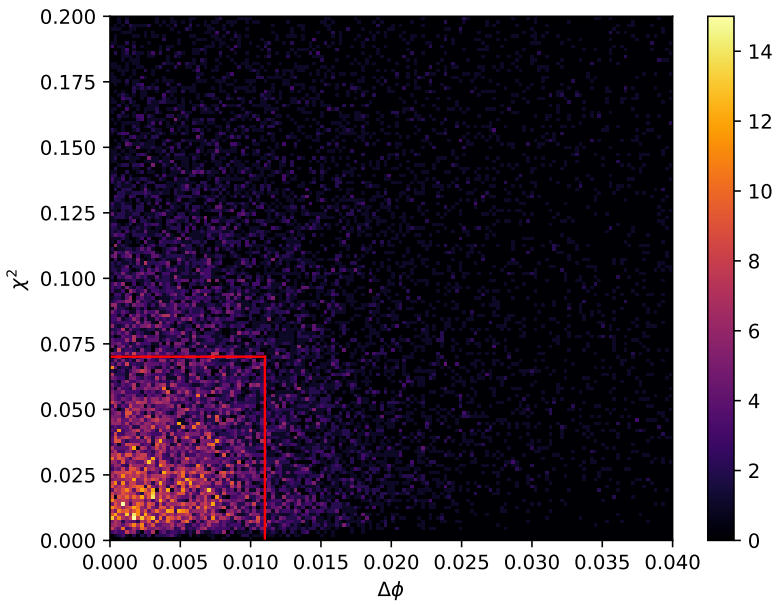

Figure 5.12: 2D histogram of χ^2 and $\Delta\phi$ for all tracks in the dataset. The red lines indicate, separately for each axis, the first bin at which the sum of the previous bins is greater or equal to 15,000 tracks, the total number of particles in the events.

with more correct hits assigned. Beyond that, after this cut we now are analyzing a collection of tracks with roughly a third of tracks, saving processing power and reconstruction time.

Cuts based on χ^2 can have various physical meanings in the context of particle colliders, and are usually linked to eliminating *fake tracks* of the collection of reconstructed tracks. *Fake tracks* are usually associated with tracks reconstructed using spurious hits: reconstructed hits that were not originated by the particles of interest in the collision, or resulting from malfunctioning of one component of the detector, hits created by the passage of cosmic rays. In this case, since these hits are not related to the process being investigated, they tend to increase the value of the track's χ^2, making the cut on the variable value efficient to get rid of such tracks.

In our case, *fake tracks* are defined as tracks that use hits generated by different particles, as we do not have spurious hits in the simulation. The cut applied on χ^2 will remove tracks which vertex of origin is not located at the origin, based on our track fitting and definition in Equation 5.9, thus eliminating at least a fraction of the fake tracks created in the CKF algorithm.

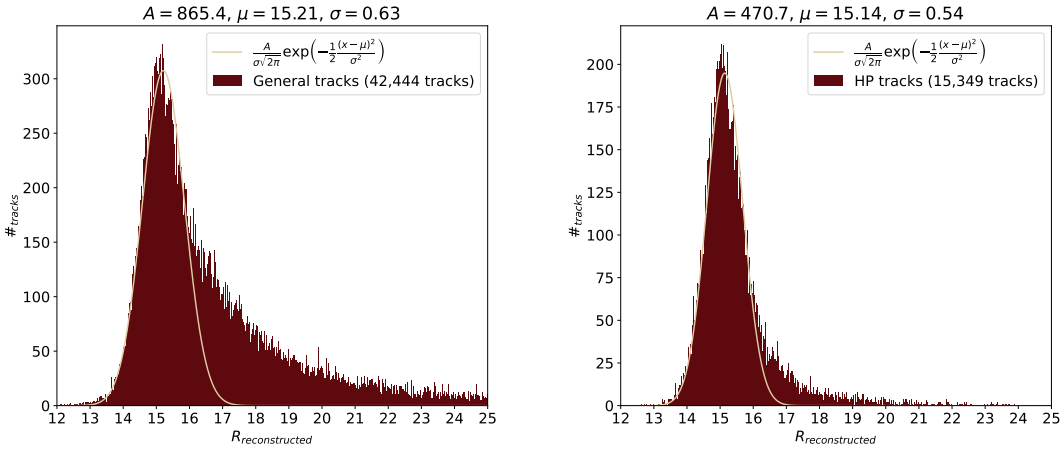

Figure 5.13: Distribution of the tracks reconstructed radius for *general tracks*, left, and *HP tracks*, right. The gaussian function was fitted only in the interval 14 cm < $R_{reconstructed}$ < 16 cm for the purpose of locate the peak of the distribution.

From Figure 5.13 we can see how the cut on χ^2 reduces considerably the number of tracks with reconstructed radii much different from 15 cm, the radius of the particles' tracks we are reconstructing. Another interesting feature of the tracks' radius distribution is that it is right-skewed: the number of tracks with $R_{reconstructed}$ below 15 cm rapidly decreases, with the distribution disappearing

around 12 cm. On the other hand, the *general tracks* have a much higher number of tracks with radius ranging to 25 cm and more. This follows directly from the algorithm used to find track hits layer by layer. When propagating the hits to further layers we defined a tolerance distance from our propagated state in which we search for nearby hits. This tolerance will then limit the curvature of the track to the propagated state $\pm\Delta\phi$, where $\Delta\phi$ stands for the allowed angular difference dictated by the tolerance distance, imposing, therefore, a minimum reconstruction radius of the track. But theoretically there is no upper limit to the reconstructed radius of the track, it grows asymptotically as the track approximates to a straight line; the opposite of the inferior limit, which is 0. Thus, when setting a symmetric tolerance in the ϕ-coordinate to reconstruct tracks, because the limits of inferior and upper values are asymmetrical the distribution of possible reconstructed radius will also be asymmetrical, in this case represented by the right-skewed distribution.

Further improving our selection, we can tackle a common issue concerning CKF: tracks sharing the same hits. Predominantly when dealing with particles that come from the event production vertex in similar directions, it is not trivial to find out which hits belong to each track. The usual outcome of a track-finding algorithm is the reconstruction of additional tracks combining hits of more than one particle, with directions close to those of the original particles. That is why the constraint applied in χ^2 is not sufficient to select only the best track candidate for each event particle, when there are particles with similar directions the algorithm tends to create more tracks than the number of particles combining hits of both, and still having a low χ^2 due to the particles' proximity.

To work around this problem, we create a separate collection of tracks called *unique tracks* to which the lowest χ^2 tracks are iteratively added, following the algorithm we now describe.

1. Initially the *Unique tracks* set is empty.
2. In ascending order of χ^2 we check for every member of the *HP tracks* set if it shares any of its hits with any member of the *Unique tracks* set.
    - If it shares, discard that track.
    - If it doesn't, add that track to the *Unique tracks* set.

Therefore, the track with the lowest χ^2 is always added to the *Unique tracks* set. The first iteration will check if the second lowest χ^2 track shares any hit the lowest

one; if they have all distinct hits the former is added to the *Unique tracks* collection.

The *Unique tracks* set is our final choice of reconstructed track of the event. To check the efficiency of our reconstruction and selection of events, we verify how many reconstructed tracks correctly correspond to the ground truth particles that were generated in the event. In order to examine it, a criterion of analysis must be adopted. We based our metric in a challenge created by a partnership between CERN, and Kaggle[4], an online platform where various data sets can be accessed and data science and machine learning techniques can be applied in order to study these.

In 2018 a Kaggle challenge was created by machine learning engineers and physicists from CERN concerning the application of machine learning techniques to particle tracking in high-energy physics colliders[5] in order to identify rare particle signatures, since the amount of data generated in such experiments is enormous. The data set was based on a toy model of a particle tracking system, although the algorithms developed to solve the challenge have a crucial importance in the CERN detectors particle reconstruction systems, and searches for new phenomena in the experiment. To evaluate the submitted solutions, a score was calculated attributing different weights to the hits of the event, according to which layer and track it belongs, and checking for each track how many hits were correctly assigned. Adapting this evaluation method to our analysis, we defined our metric score as follows:

- Each hit of the track is assigned a value of 0 if it does not belong to the particle being reconstructed, and 1 if it does. All hits have the same weight, due to our simplified toy model with equally spaced detector layers.
- A score of the track is calculated, averaging its hits values. The criterion of matching between tracks and particles is simply absolute majority, or a score greater than 0.5, implying in 6 or more correct hits assigned to a track.

The tracks satisfying the above requirements are called *matched tracks*.

Considering the whole set of 1,000 events, we managed to reconstruct 5,889 tracks, $\sim$ 40% of the total 15,000 $\pi^{\pm}$ generated. The distribution of the tracks' reconstructed radius are shown in Figure 5.14. The number of correctly assigned hits per *matched track*, as well as the number of *matched track* per event are shown in Figure 5.15.

[4]More information about the platform can be found in Kaggle's website.
[5]TrackML Particle Tracking Challenge.

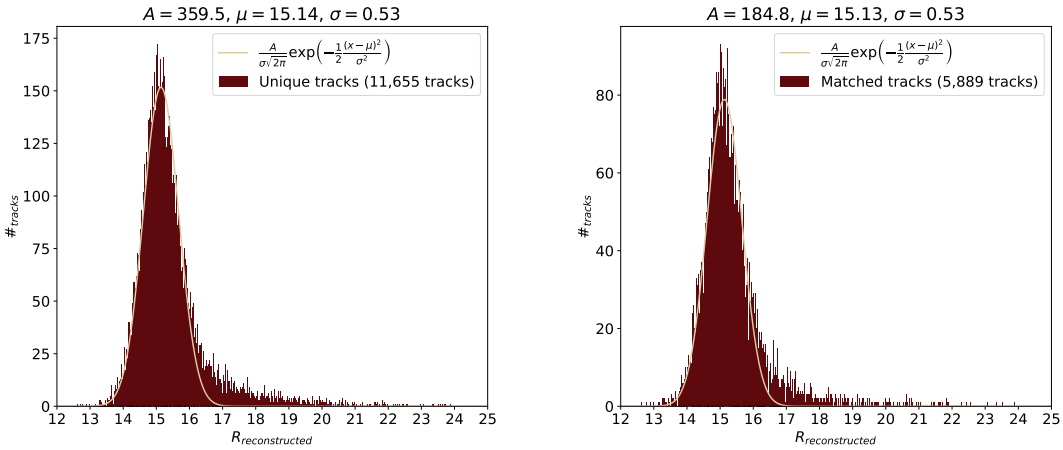

Figure 5.14: Distribution of the tracks reconstructed radius for *unique tracks*, left, and *matched tracks*, right. The gaussian function was fitted only in the interval 14 cm < $R_{reconstructed}$ < 16 cm for the purpose of locate the peak of the distribution.

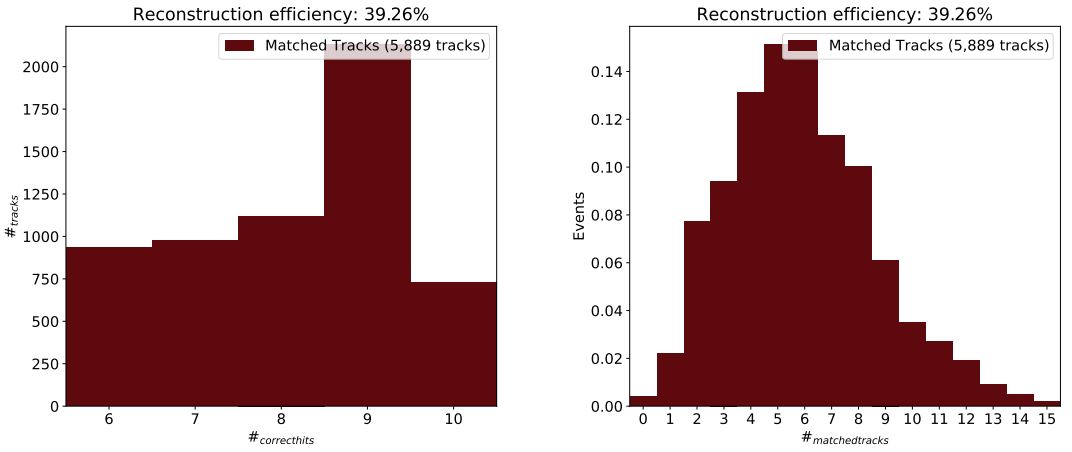

Figure 5.15: On the left panel is shown the distribution of correctly assigned hits per *matched track*. The right panel contains the normalized distribution of *matched tracks* per event.

Concerning the matter of particle tracking, we were able to implement a CKF algorithm reconstructing roughly 40% of the generated particles when dealing with the toy model described in this section. Table 5.2 contains all selections applied in the whole set of tracks generated by the CKF algorithm.

Summarizing the whole CKF algorithm implemented, we have:

- *Seed generation*: Initial positions and velocities (seeds) are defined with the hits of the first two layers.

Selection's name	Requirements	Number of Tracks
General tracks	All generated tracks by CKF	42,444
High-Purity tracks	$\chi^2 < 0.07$	15,349
Unique tracks	Tracks that do not share similar hits	11,655
Matched tracks	Correctly reconstructed tracks	5,889

Table 5.2: Selections and its respective requirements, filtering higher quality tracks.

- *Trajectory bulding*: Using the hits of the seed, we define a *track* and propagate it with Kalman filter formalism to subsequent layers, searching for near hits until the last layer.
- *Final track fit* Considering only the tracks that managed to be reconstructed with 10 hits, they are fitted to a helicoidal trajectory, segment of circle in the plane (r, ϕ)
- χ^2*-cut*: In order to refine the *general tracks*, we constrain our selection to the lowest χ^2 tracks (*HP tracks*).
- *Unique tracks*: Tracks that share common hits are excluded from the selection, remaining the lowest χ^2 one (*unique tracks*).
- *Evaluation*: It is checked how many of the *unique tracks* were correctly reconstructed, meaning if it found 6 or more correct hits of the particle.

The toy model of the detector, the Kalman filter procedure, the fitting of the tracks, the CKF algorithm and the classification of quality of tracks were all implemented from scratch[6]. However, this simplified model lacks many important aspects of the collisions that are reconstructed by the CMS detector, thus we chose to use the CMS' software package `CMSSW` to perform an analysis of disappearing tracks, since it works with 3 dimensions, allows the study of real events, is able to simulate the full detector components and its interaction with particles, study fundamental parameters of particles such as p_t and η. In this way, we are able to perform a richer and more realistic analysis of the disappearing tracks reconstruction by the CMS experiment.

[6]The repositories containing the Kalman Filter implementation and the analysis presented in the following Chapter can be consulted on my GitHub profile.

Chapter 6

Track Reconstruction in the CMS Experiment

6.1 Overview of CMS' Software

In order to compare our implementation with the tracking system used in the CMS experiment, we proceed to analyze the reconstruction of events with the collection of software called `CMSSW` [146] , a software package with numerous tools and libraries available focused on simulation and study of particle collisions in the CMS detector. `CMSSW` produces Monte Carlo events, gathers calibration and alignment, generation of events , simulation tools and services to the experiment's researchers in a unified Framework. It is constantly maintained by a large community of physicists and developers in order to have faster and more efficient and accurate detector simulations while keeping it up to date to the detector upgrades.

The processing model of `CMSSW` is built around one executable, `cmsRun`, and the usage of the available tools is configured in `cmsRun` setup file. Monte Carlo simulations, reconstruction algorithms, event generation are all defined in modules that are called in the `cmsRun` setup, including the order in which they must be executed, the parameters of each module, files that will be used. All the information concerning the collisions are stored in a `C++` object called *Event*, the RAW data from the detector electronics, the reconstruction of particles, state of the detector components. It is through the Event, exclusively, that data is processed and communicated between the modules. Data of the Event are stored in ROOT files, thus can be accessed through ROOT in all steps through the modules individually. To generate events and simulate them in the CMS detector, `CMSSW` integrates other software dedicated to deal with different parts of the particle collision and its detection. Thus, instead of using different tools separately, the software Framework provides a straightforward approach to study such events, allowing the researchers to create and analyze different physical scenarios without

having to spend a large amount of time dedicated to the computational details of the simulation and integration of different programs. Beyond performance, CMSSW is developed assuring flexibility, modularity, documentation, ease of use, making it widely used by the CMS community and a fundamental research tool.

6.1.1 Events Generation

The data of the events in this study used are not from real collisions taken place in the CMS detector, they are generated through Monte Carlo simulations with multiple software packages. This allows us to create events with BSM physics models to study and predict how the events' detection could occur in such scenarios, aiding phenomenologists to test its models and further develop them. Also, for experimental physicists they have great utility to design adequate colliders and detectors to investigate interesting phenomena.

In pp collisions with high p_T, it is usually described theoretically through the hard scattering of partons and the subsequent fragmentation of the partons in the hadrons, or hadronization. To deal with hard scattering of the protons, *partition distribution functions* (PDFs) are used to describe the collisions through the constituents of hadrons: quarks and gluons. In the hard scattering process, rare particles are produced, such as the Higgs boson and the LLP of the FIMP and AMSB model, charginos in this project. But in general, such particles live very short time, rapidly proceeding to the fragmentation in the parton shower and lastly hadronizing in the detected particles. Figure 6.1 represents this process, the inner black circle indicates the hard scattering, above this circle the fragmentation in parton showers is shown in red, and at the top in green the hadronization. The lower half of the figure is a diagram of the multi-parton interactions, that may happen in the proton.

The generation of the hard process are made with MadGraph5_aMC@NLO (MG5)[147], a framework dedicated to calculate hard processes events generation, cross sections and other important variables of SM and BSM phenomenology. Processes of both leading order (LO) and next to leading order (NLO) can be generated in QED and QCD.

The events were generated through MG5 [1], in which we included charginos of $m_{\tilde{\chi}=700\,\text{GeV}}$ and $c\tau$ distribution centered at $c\tau \sim 50\,\text{cm}$ production. To study tracking of LLP charged particles that decay to non-observables in the CMS detector,

[1] MG5's version 3.1.1, documentation at MadGraph5_aMC@NLO's website

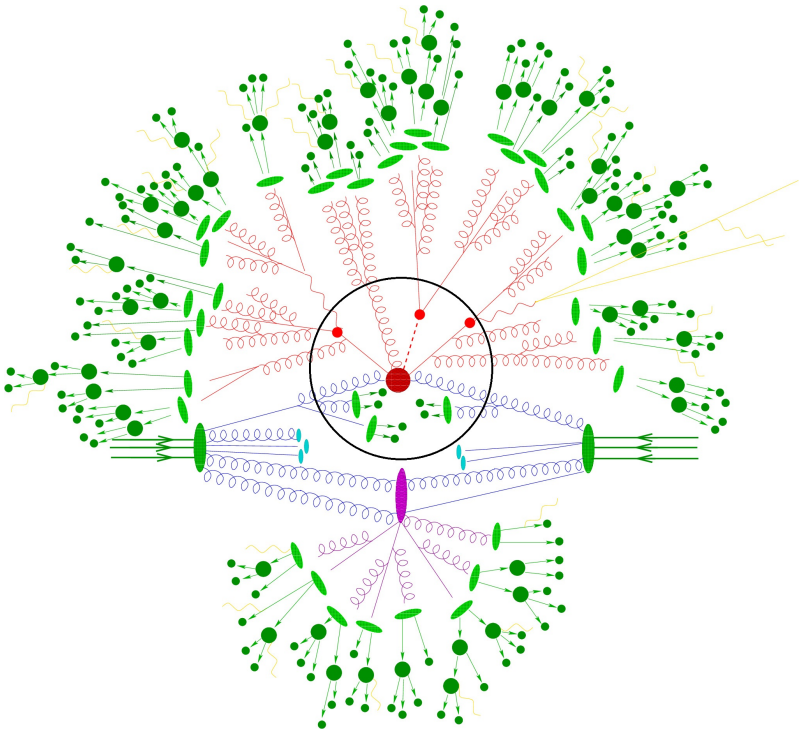

Figure 6.1: Diagram of a high energy hadron collision. Circled in black the representation of the hard process, treated with perturbative QCD, above the circle the fragmentation in parton showers in red and further the hadronization in green. Below the circle the multiparton interaction is represented, treated with non-perturbative QCD, and its consequent hadronization process as well.

we use the AMSB framework, that has a signature similar to the FIMP model. We use a data set of 10,000 events, in which we include the production of $\tilde{\chi}^{\pm}$, to study the tracking of charginos, particularly its efficiency as function of the charginos' characteristics.

Our data set of events were generated as pp collisions with energy at the center of mass of 13 TeV. Two channels of $\tilde{\chi}^{\pm}$ production are included:

$$pp \to \tilde{\chi}^{\pm} + \tilde{q}_0$$
$$pp \to \tilde{\chi}^{\pm} + \tilde{q}_0 + \text{jet}$$

where $\tilde{q}_0$ stands for the wino-like neutralino of the AMSB model [65, 66, 67].

After the hard process is simulated, using the output of the MG5, `Pythia 8`[2][148] is used to calculate the hadronization of particles. Pythia's libraries provide models of parton showers, multiparton interaction, matching and merging of hard

[2]Pythia's version 8.243, documentation at Pythia's website.

processes and parton showers. Therefore, we can calculate the whole collision processes of interest involved using MG5 and Pythia.

Lastly, using `Geant4`[3][149] the whole CMS detector geometry, its material components, the interaction of the particles of the event with the detector's components can be simulated. With `CMSSW`'s tools, we can also model the detector's electronics and the process of digitization (a simulação de um circuito ACD). With the collision processes and the outputs of the detector's electronics simulated, we can then study and analyze the tracking systems. With the generation of the collision processes completed, we use the generated events as input to implement the tracking of particles and develop further the analysis.

In total, 10,000 charginos were created in the events, of which 6,947 were matched to tracks, representing a reconstruction efficiency of $\sim 71\%$. In order to be matched, the reconstructed chargino must meet two requirements: $p_T > 10\,\text{GeV}$ (all satisfied this condition) and it must have a distance to one of the reconstructed tracks of $\Delta R < 0.1\,\text{cm}$. The efficiency is calculated as the fraction

$$\text{eff} = \frac{\#\tilde{\chi}^{\pm} \text{ matched to tracks}}{\#\text{Generated } \tilde{\chi}^{\pm}} \quad .$$

On account of the charginos' mass being large, the momentum distribution of the particles ranges significantly, consequently the particles' decay length - defined as the distance travelled from the production vertex until its decay in the laboratory reference frame - varies correspondingly.

Although the decay length (l) is the quantity observed in the experiment, using the particles' $|\vec{p}|$, consequently β and γ, we obtain its $c\tau$

$$\begin{aligned}\left(\frac{1}{\beta\gamma}\right) l &= \frac{1}{\beta}\frac{l}{\gamma} \\ &= \frac{c}{v} l' \\ &= c\tau\end{aligned}$$

where the factor $\frac{1}{\beta\gamma}$ is a *boost* to the particle's reference frame.

In Figure 6.3 it can be seen that in fact the decay length is correlated with the particles' momentum, as it should be, since the relativity boost increases its travelled distance in the laboratory's reference frame. On the other hand, the low value of the Pearson correlation coefficient, $r = -0.10$, between $c\tau$ and β endorses

[3]Geant4's version 10.4.3, documentation at `Geant4's website`

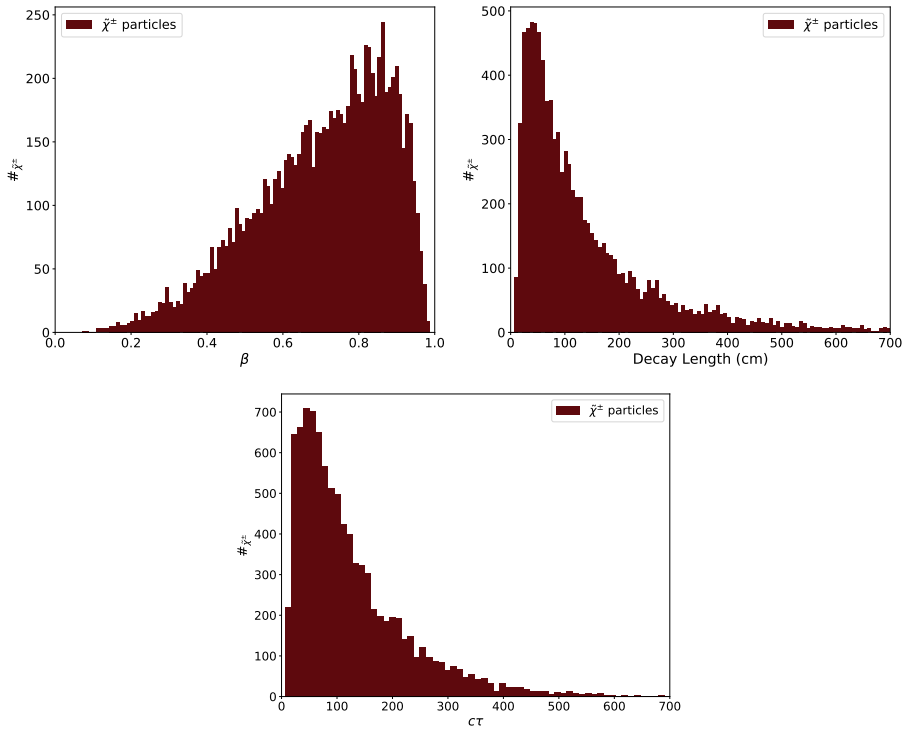

Figure 6.2: In the upper left panel it is shown the distribution of $\beta = \frac{v}{c}$ of the reconstructed chargino particles; the upper right panel displays the decay length of such particles. The lower panel shows the $c\tau$ distribution in cm.

that they are independent quantities. $c\tau$ is the mean lifetime of the particle at rest, in its inertial reference frame, thus should not be correlated to the observed β in the laboratory's reference frame.

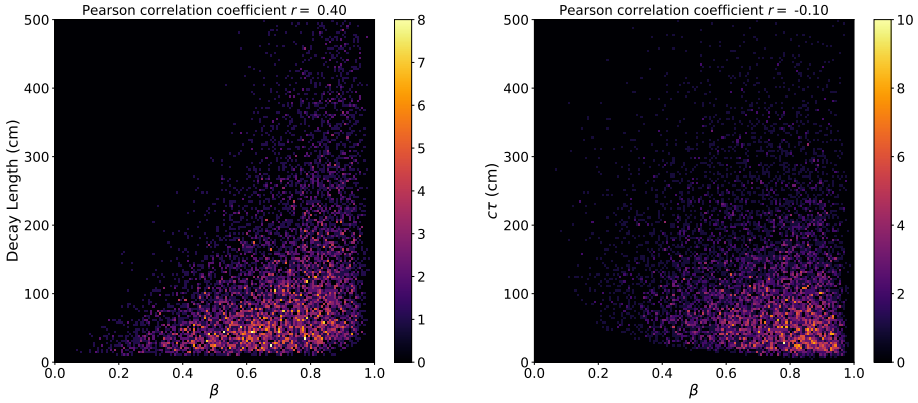

Figure 6.3: 2D histograms correlating the decay length (left) and $c\tau$ (right) with the particles' β.

6.2 Track Reconstruction in CMSSW

Figure 6.4 shows the behavior of Valid Hits of matched tracks when varying the charginos' mean lifetime. The distribution of $c\tau$ is centered in 10 cm, and at least three Valid Hits are necessary to construct a track and match it to the particle. Hence, it is needed that the $\tilde{\chi}^{\pm}$ travels at least so far as the first three layers of the detector before decaying, meaning that its Decay Length has a threshold value below which no track will be reconstructed nor matched to the particle.

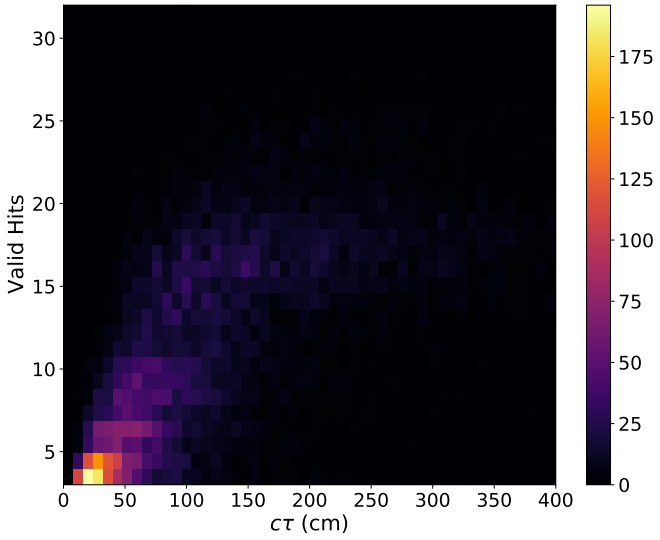

Figure 6.4: 2D histogram of the particles' $c\tau$ and the number of Valid Hits of the matched tracks associated with the tracked $\tilde{\chi}^{\pm}$.

Sorting the matched tracks of all the events by the associated particle Decay Length, Table 6.1, we see that at Decay Length ~ 11 cm tracks begin to be found and matched to particles. On the other hand, if we notice the design of the barrel pixel detector in Figure 4.5, the innermost subdetector of CMS, the third layer (L3) is located at radius $r = 10.9$ cm (Subsection 4.1.1), in agreement with the observed threshold effect. Also, the η values in Table 6.1 are near 0, as expected, since they are equivalent to $\theta = \pm\frac{\pi}{2}$, the shortest path to the subdetector. The fact that they describe curved trajectories increases as well the needed Decay Length to reach the first three layers.

Another expected behavior shown in Figure 6.5 is the increasing number of Valid Hits with the respective increase of mean lifetime of the particles between $11\,\text{cm} < c\tau < 150\,\text{cm}$. Higher mean lifetime implies a longer travelled distance,

Index	Charge (e)	p_T (GeV)	ϕ	η	Decay Length (cm)
7501	1	914.2	-2.09	0.06	11.004
3989	1	386.1	1.33	-0.14	11.005
11005	-1	227.4	-1.72	-0.19	11.107
7985	-1	489.6	-0.36	-0.10	11.138
11690	-1	613.0	-2.63	-0.16	11.172

Table 6.1: Matched $\tilde{\chi}$ with the five shortest Decay Length from our whole data set. The Index column is relative to the *DataFrame* index, and has no physical meaning.

allowing the particle to interact with more layers of the detector, thus increasing the number of Valid Hits of its track. After $\sim 150\,\text{cm}$ the distribution of Valid Hits becomes roughly constant. That happens because for those large values of $c\tau$ the particle lives long enough to cross all the detector layers. The Tracker Outer Barrel (TOB) and Tracker EndCaps (TEC), the outermost components of the Silicon strip tracker, range up to $\sim 115\,\text{cm}$ (Figure 4.4), again in agreement with the results obtained.

In Figure 6.5 we observe the foreseen increase of Valid Hits until a point that it stagnates. Also, it is shown that the Decay Length follows the same behavior as $c\tau$ with respect to Valid Hits.

Another important parameter to study in the analysis of the Tracking System is the p_T resolution, since it gives us knowledge of how well the p_T reconstruction is being done. Specially in the case of CKF, to reconstruct with great accuracy the transverse momentum is directly related to finding the correct track of the particle, Subsection 5.2.

By definition, the p_T resolution is

$$\frac{\Delta p_T}{p_T} = \frac{p_T^{Track} - p_T^{Particle}}{p_T^{Particle}} \quad , \tag{6.1}$$

thus in view of the value of p_T being limited to non-negative values, the resolution has the lowest possible value being -1, when $p_T^{Track} = 0$ and $p_T^{Particle} > 0$. But it is not limited from above.

Figure 6.6 shows all the $\tilde{\chi}$'s matched tracks' p_T resolution and an estimation of the distribution peak and dispersion. The mean of the distribution is located at $\mu = -0.02$ with $\sigma = 0.008$, an indicative that a great fraction of the tracks are being reconstructed with a high accuracy, 2% error. On the other hand, it is clear that there is an excess of events with negative resolution, which is considered to be a natural consequence of the asymmetric codomain of the p_T resolution function,

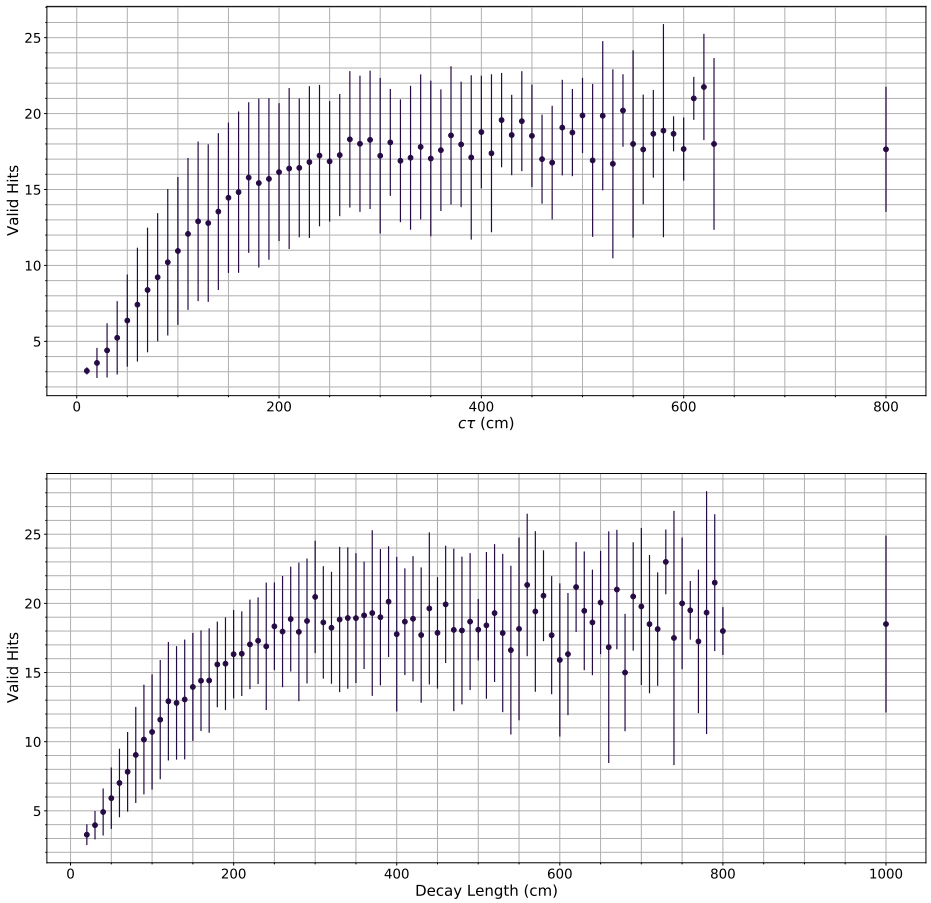

Figure 6.5: Plot of the mean Valid Hits of $\tilde{\chi}^{\pm}$ tracks contained in intervals of 10 cm of $c\tau$ and Decay Length. In the upper (lower) plot the last point, $c\tau = 800$ cm (Decay Length = 1000 cm), represents all tracks with $c\tau > 640$ cm (Decay Length > 800 cm), considering that there are fewer charginos in this range, commonly resulting in intervals with only one chargino or none of them.

$[-1, +\infty)$.

We checked how $\frac{\Delta p_T}{p_T}$ behaves with other particles' properties such as the p_T itself, η, ϕ as shown in Figure 6.7. However, the distributions of η and ϕ have centered peaks of distribution near 0 and elsewhere an homogeneous profile. The $\frac{\Delta p_T}{p_T} \times p_T$ histogram has its distribution centered near 0 and a slight excess in the left region due to the limited codomain of the p_T resolution function.

Another property that can be analyzed is the particle Decay Length, shown in

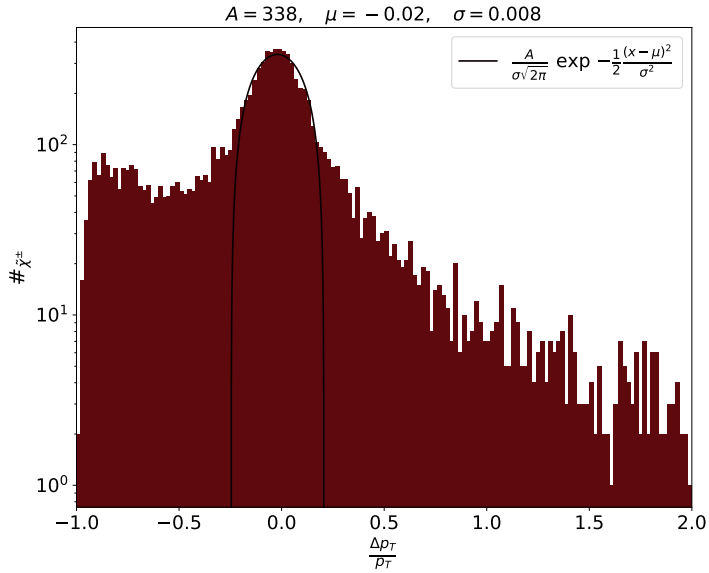

Figure 6.6: Histogram of the resolution of all tracked in the events. The gaussian (when plotted in log the y-axis becomes a parabola) was fitted in the range of $-0.5 < x < 0.5$ to estimate the peak of the distribution and its dispersion.

Figure 6.8. It becomes evident the shift of distribution of $\frac{\Delta p_T}{p_T}$ in the left panel,in which we can see that for lower values of Decay Length the resulting resolution is biased to negative values. For increasing values of Decay Length up to $\sim 75\,\text{cm}$ the distribution peak shifts from $\frac{\Delta p_T}{p_T} \sim -0.9$ to ~ 0, where it stays stable for higher values of Decay Length. This thinks to imply that the Tracking System has difficulties reconstructing lower Decay Length particles, estimating lower values than the actual ones of the particles' p_T. This is a reasonable correlation, since if the particle decays too fast, it leaves fewer hits in the Tracking Systems, which turns the problem of reconstructing the tracks even harder, increasing considerably the margin of error.

6.2.1 Track Reconstruction Efficiency

The track reconstruction efficiency measures the probability of a track that passing through the detector signaling more than 3 hits being reconstructed. It is highly important to study the Tracker performance with simulated events for the sake of guaranteeing that the simulations are in accordance with the detector performance and thus to know the limits and usual behavior of it. Comparison between the simulated events and real data are made to ensure the reliability of

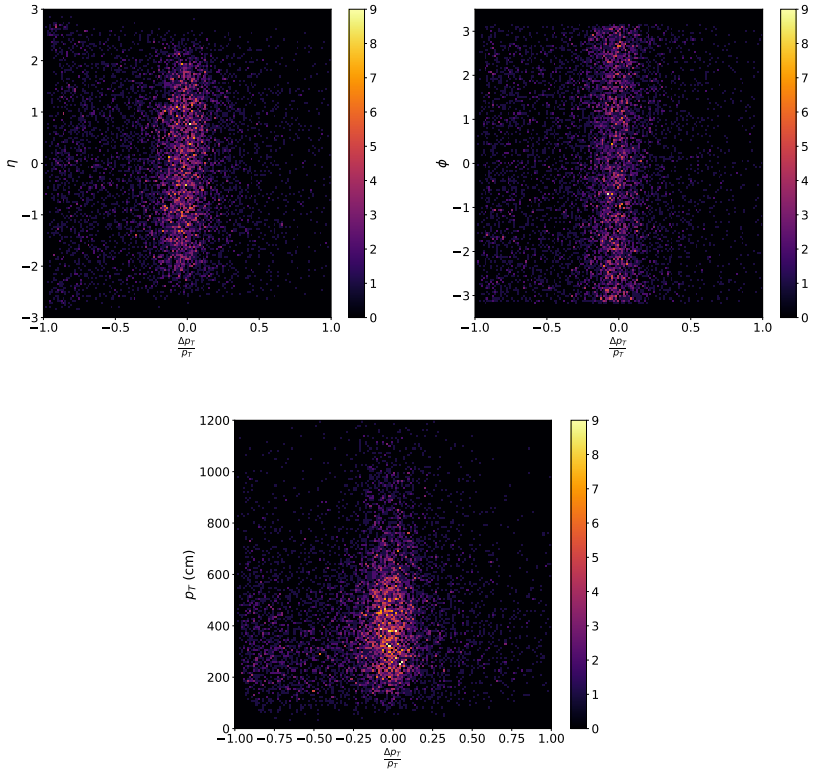

Figure 6.7: 2D histograms exploring the relation between p_T resolution and particles' properties. In the upper left panel resolution and η, upper right ϕ and resolution and the lower panel p_T and its resolution.

our simulations.

Naively, we could define the efficiency as

$$\text{eff} = \frac{\#\tilde{\chi}_{\text{Tracked}}}{\#\tilde{\chi}_{\text{Generated}}} \quad ,$$

however, in order to be reconstructed by `CMSSW`, the track must satisfy a few requirements. Hence, the denominator, instead of being all generated $\tilde{\chi}$, must be the generated particles that satisfy the tracking system requirements.

One fundamental constraint that must be applied to the denominator is that the generated particles must pass through the detector. Due to the cylindrical geometry of the detector there are restrictions in the η coordinate. The Tracking system covers the region of $|\eta| < 2.5$, so we must restrict our calculations to $\tilde{\chi}$s generated in this range. Thus, we have our efficiency defined as

$$\text{eff} = \frac{\#\tilde{\chi}_{\text{Tracked}}}{\#\tilde{\chi}_{\text{Generated}_{|\eta|<2.5}}} \quad . \tag{6.2}$$

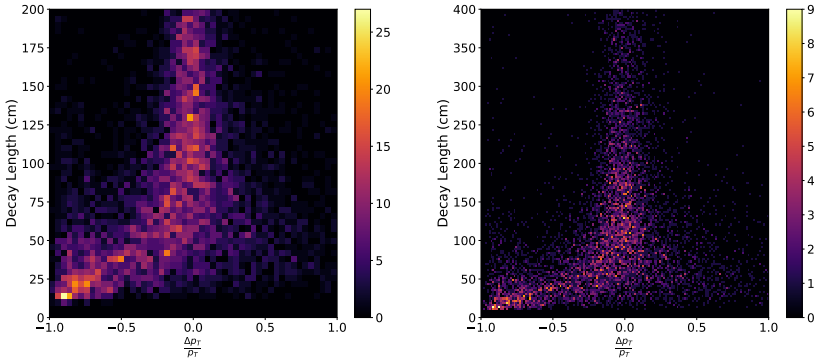

Figure 6.8: 2D histograms of the tracked charginos and its p_T resolution. The left panel shows more clearly the tendency of low Decay Length particles to have negative p_T resolution.

To calculate the efficiency based on particle and track's properties, ranges of values of the variables were defined in which we used Equation 6.2. Figure 6.9 shows the efficiency as function of the Decay Length and $c\tau$. Once more it can be seen that both variables behave similarly to each other, the reconstruction efficiency rising up as the variables increase, as expected since for low values of $c\tau$ and Decay Length the probability of a particle reaching the extension of the detector leaving at least 3 hits is reduced. The subsequent stable behavior is reasonable as well, due to the increasing probability of leaving more hits in the detector, leading to a greater chance of being correctly reconstructed. The subsequent stable behavior of the efficiency is also expected, since higher Decay Length and $c\tau$ values imply in a greater chance that more hits will be generated, thus increasing the probability of a successful track reconstruction.

The last entries in the plots display greater uncertainties since they have progressively fewer entries, as seen in Figure 6.2. In order to estimate the error bars values, we used `ROOT`'s framework in which the *Wilson's procedure for asymmetric error bars* is implemented [150].

When analyzing the efficiencies with respect to the angular coordinates (η, ϕ), similar behaviors are perceived, with low variations from the mean reconstruction efficiency, Figure 6.10. Since the detectors are designed to have no favored direction of performance, due to the symmetry of the particle distribution in the collision, the results are satisfactory. Analyses as this one are fundamental in the experiment to spot possible regions of malfunctioning in the detector, misbehavior of the reconstruction algorithm, alignment of the detector's components. As already mentioned, the efficiencies for η are restricted to $|\eta| < 2.5$. For $\eta \sim 2.5$ a reduction

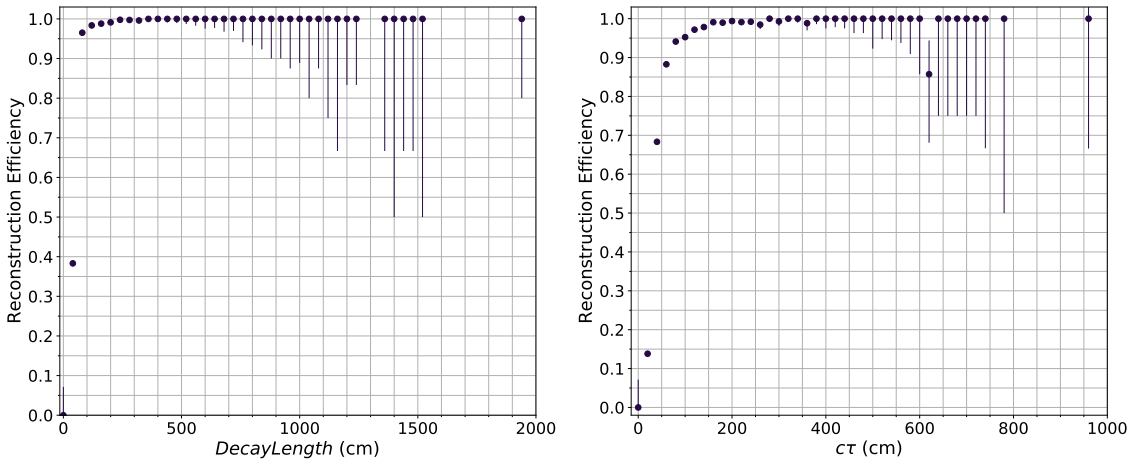

Figure 6.9: Track reconstruction efficiency as function of the Decay Length and $c\tau$ of the charginos. The left plot uses intervals of 40 cm of Decay Length to calculate the efficiency, while the right plot 20 cm for $c\tau$. The Last entry in both panels represents all particles with greater variable values than the entry before it.

in the efficiency can be seen, which is reasonable considering that fewer hits are left near the extremities, the particle trajectory travels through fewer pixel and silicon strip sensors.

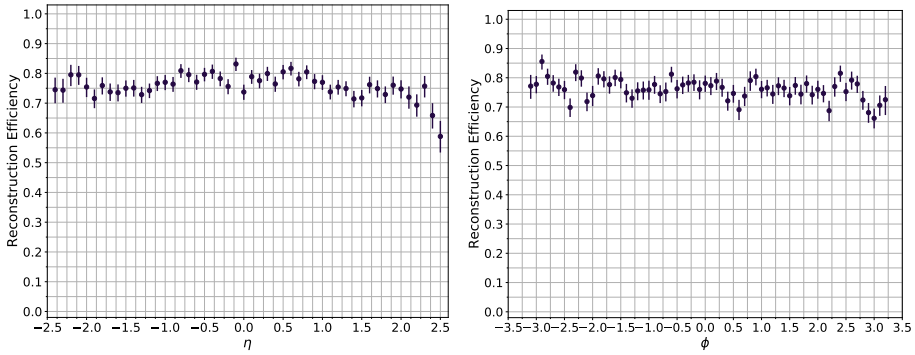

Figure 6.10: efficiencies of $\tilde{\chi}$ track reconstruction as function of η, in the left panel, and ϕ, right panel, coordinates. Due to the detector's geometry, only $|\eta| < 2.5$ are considered.

The particle's p_T reconstruction plays a fundamental role in tracking algorithms, it is directly related to the performance of the radius of curvature of the track reconstruction. In Figure 6.11 we can observe the increasing efficiency as the particles' p_T increases, reaching the mean efficiency at $p_T \sim 300$ GeV. Considering the usually faster rate at which the efficiency increases, we analyze in deeper details its behavior for the lower values of p_T.

An important difference between our analysis and the CMS' collaboration

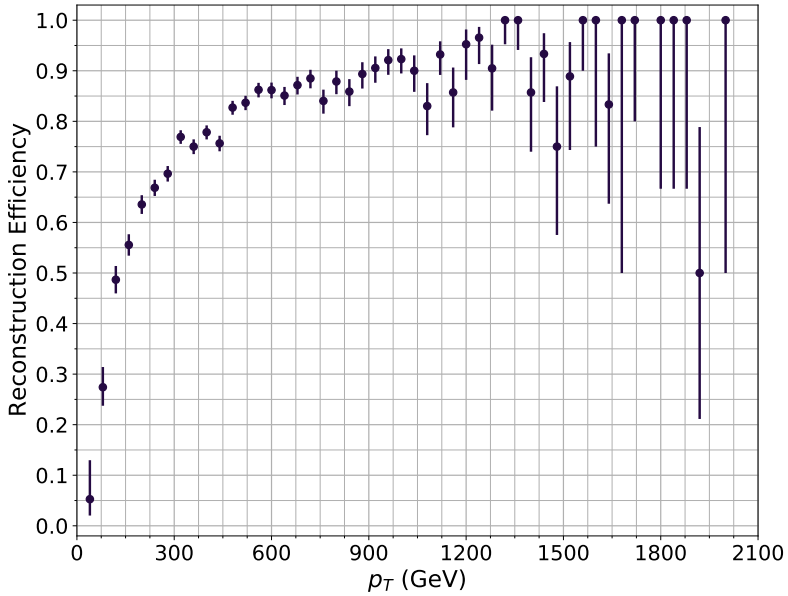

Figure 6.11: Track reconstruction efficiency of the particles' p_T.

[126] (detailed in Section 6.3) is the mass of the particles being tracked. In the latter, electrons, muons and pions are considered, thus the masses up to order of a hundred MeV ($m_e \sim 0.511\,\text{MeV}, m_\mu \sim 106\,\text{MeV}, m_{\pi^\pm} \sim 140\,\text{MeV}$), while the charginos we are tracking have $\sim 700\,\text{GeV}$. Having a greater rest energy, the charginos demand more energy to boost them at the same speed as lighter particles, implying in our case that to travel enough distance to reach the detector's Tracker layers more energy, thus greater p_T, are required. This way, a consequence of the higher mass value of $\tilde{\chi}$ will be a shift in the turn-on curve of the efficiency to higher values of transverse momentum, on account of the surplus energy necessary to achieve the same hit pattern in the detector.

Another relevant difference between the analysis, is the mean lifetime of the particles, while the charginos and pions have similar lifetimes ($c\tau \sim 10\,\text{cm}$), the muon is considerably greater ($c\tau \sim 600\,\text{cm}$) and the electron is stable. Shorter mean lifetime implies as well in the turn-on curve shifting to greater values of p_T, for the same reason as explained above.

Based on this discussion, I proceeded investigating the possible effects of the mean lifetime in the p_T reconstruction efficiency. Applying tighter constraints in the $c\tau$ progressively of the $\tilde{\chi}$ we obtain the plots shown in Figure 6.12. From the first plot (left panel) it is already noticeable the steeper turn-on curve compared to Figure 6.11, achieving the mean reconstruction efficiency for $p_T \sim 100\,\text{GeV}$. The two other plots accentuates this behavior furthermore, shifting the turn-on curve

to lower values of p_T and making it more abrupt.

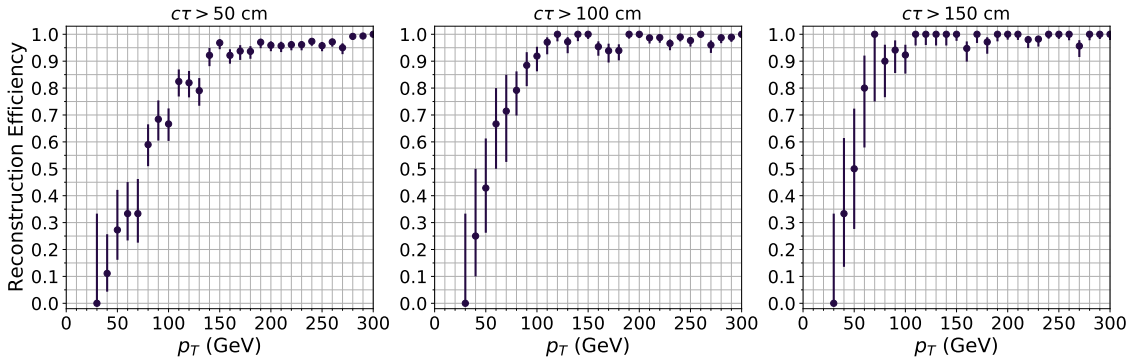

.

Figure 6.12: Track reconstruction efficiencies of p_T with applied thresholds on the particles $c\tau$, from left to right, of 50 cm, 100 cm and 150 cm

At last, in Figure 6.13 are represented the efficiencies of the charginos without cuts applied on the mean lifetime together with the results of applying a threshold on $c\tau$ of data set of particles. It is evident the dependence of the turn-on curve, hence in the track reconstruction efficiency, on the charginos mean lifetime.

6.3 Comparison with Published Results

In order to validate the results obtained concerning particle track reconstruction, we compare them with an analysis performed by the CMS collaboration studying the performance of tracks and primary-vertex reconstruction in the detector[126]. However, this analysis was developed based on data from the first run of the LHC (2009-2013), while our study is in the scope of the second run (2015-2018). Between the two runs, upgrades were made in the detectors (Section 4.1.1), in particular in the Tracking system of the CMS, the discrepancies will be explained, although we argue in favor that conclusions and comparisons can be made relating both analysis.

6.3.1 Simulated Events

In the cited analysis, simulated events are used instead of data taken at CMS detector, allowing us to study how the geometry of the detector, tracking algorithm, events' configuration alter the track reconstruction performance. The results obtained can be compared with CMS data to verify that the simulations are realistic.

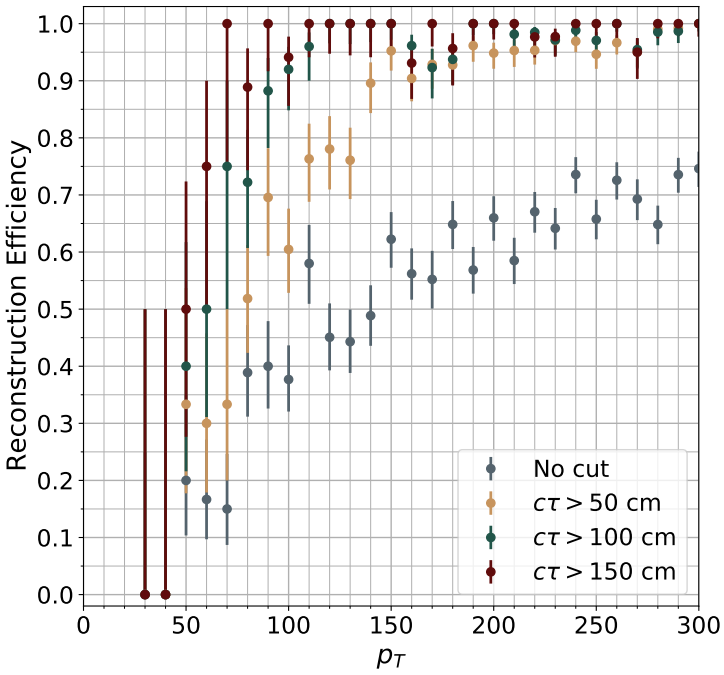

Figure 6.13: Track reconstruction efficiencies of p_T with and without restrictions on the particles' $c\tau$. The gray points represent efficiencies with no cuts applied, in yellow a threshold of $c\tau > 50$ cm was set, in green $c\tau > 100$ cm and the red points $c\tau > 150$ cm.

The generated events have single particles being produced, although secondary particles can be present due to interaction with the detector's material, and can have fixed transverse momentum of 1, 10 and 100 GeV or a flat distribution given by $\ln p_T$. The latter data set is used to study the tracking performance as function of the particles' p_T, while the former the performance with different η values. As already discussed, the acceptance tracking region of the detector is constrained to $|\eta| < 2.5$, thus the particles were generated in this range.

The pp collisions were simulated with `Pythia` 6[151] with or without pile up. An event pile up depends on the collider luminosity and the amount of time in which data was taken, thus in the simulation a Poisson distribution of mean $\mu = 8$[4], the average of the whole year of 2011 delivered in LHC, was used to set the pile up in the events.

In order to calculate the track reconstruction efficiency and *fake rate*, the generated particles' information are used and compared with the reconstructed tracks.

[4] A low value of pile up compared with present values.

A track is considered correctly reconstructed, *matched*, if 75% of its hits were from the same generated particle, and so the reconstruction efficiency is defined as the ratio of tracks successfully reconstructed divided by the total number of particles (remember that all particles are in the tracking system acceptance region). On the other hand, the fake rate is the ratio of the tracks that were not matched to any particle over the total number of generated particles, representing tracks that were badly reconstructed by association of multiple particle hits, or the inclusion of spurious hits in the track.

6.3.2 Tracking Algorithm

The tracking algorithm of the Tracker System was also updated in order to exploit the advances of the hardware upgrade of the Tracker System, such as the extra pixel layer in the PIB. As implemented in Subsection 5.3, the tracking in CMS detector is divided into steps: seed generation, trajectory building, ambiguity resolution (deciding between tracks that share common hits) and final track fit. This pattern is minimally changed between the two runs, although they are implemented in different manners through *iterative tracking* (Subsection 5.1). Before the Phase-1 pixel upgrade, the iterative strategy used in HLT to reconstruct tracks used 4 iterations through each of them the requirements are progressively loosened.

Generating seeds in the CKF can be costful in terms of processing power since if the constraints are not well defined we can end up with a task combinatorial on the number of hits, a gigantic problem for future upgrades with increasing pile-up and luminosity. On this wise, different seed generating algorithms are implemented and available to be used appropriately in different steps o the tracking. For Run 1, *Pixel triplets* were the stricter seed generating algorithm, in which it first created pairs of hits using the BPIX and FPIX layers, and after that searches for a third hit compatible with the hit pair. It is relevant to note that with a hit pair we can not estimate the track p_T, hence no threshold can be applied to aid in the constraints of the seeds generation. Thus it used a vertex estimate, or if not available the center of the beam spot, to build the track trajectory or search a third hit for the seed.

Mixed seeding on the other hand is not restricted to use only pixel hits as seeds, it allows hits from the silicon detector as well to be used. These two seeding algorithms have different purposes in selecting which particles are wanted to be reconstructed using each of them. When looking for prompt tracks, from the

primary vertex, using Pixel triplets is more adequate because it will mitigate possible seeds from the secondary vertex that do not leave three consecutive hits in the pixel layers, for example.

In the tracks' reconstruction process, once we generated the seeds, propagated, found tracks, we can continue refining our selection placing thresholds on its p_T. When working with iterative tracking this is another useful parameter to take into account, considering the distribution of charged particles transverse momentum, the number of such particles with high p_T is considerably smaller than low p_T ones. Likewise, particles with higher transverse momentum tend to leave more hits in the detector, thus these are reconstructed first in the iterative tracking strategy. This way we can in the first iteration use a stricter seed algorithm, demanding a higher number of hits from the pixel layers, higher number of hits in the track and use a threshold on p_T, to work with fewer particles, thus faster than using the whole set of possible seeds. In the subsequent iterations, the already reconstructed track hits are ignored, reducing the number of seeds and tracks to be selected.

Beyond the cut on p_T, a set of tracks can be further cleaned based on the compatibility of the track with the reconstructed vertex[5]. In the scope of CMS tracking reconstruction, we define a track with five parameters: $\mathrm{d}_0, z_0, \phi, \cot\theta$ and p_T, all defined in the point of closest approach to the reconstructed beam axis, the *impact point*. The point coordinates are d_0 and z_0, d_0 are the transverse coordinates of the impact point ($\mathrm{d}_0 = x_0 \sin\phi - y_0 \cos\phi$), where ϕ stands for the azimuthal angle and θ the polar angle of the vector of the track.

In the transverse plane a threshold can be set on the transverse impact parameter (d_0), while in the longitudinal plane the constraint can be made in the difference between the reconstructed vertex and the track's closest approach to the beam line (z_0). If no reconstructed vertex is available, the vertex of the leading reconstructed track is used, and a further filter on χ^2 is applied at the end.

Table 6.2 shows the main parameters used in the iteration steps of iterative tracking implemented during Run 1. As pointed before, the first iterations use more restrict constraints, reducing the number of fake rates and consequently the time spent tracking particles, fundamental for Trigger processes.

The results concerning the iterative tracking description adopted throughout Run 2 were not yet published, thus we can not make a direct comparison between the iteration steps used in both Runs. Although, searching the records of colli-

[5] If there exists a reconstructed vertex already in this stage of reconstruction.

Iteration	$\text{Algo}_{\text{seed}}$	Target track	p_T^{Min} (GeV)	d_0 cut	z_0 cut
0	Pixel Triplet	Prompt, High pt	0.6	0.03	4.0σ
1	Pixel Triplet	Prompt, Low pt	0.2	0.03	4.0σ
2	Pixel Pair	High pt Recovery	0.6	0.01	0.09σ
3	Pixel Triplet	Displaced	0.2	1.0	4.0σ
4	Pixel + Strip Triplet	Displaced	0.35-0.5	2.0	10.0cm
5	Strip Pair	Displaced	0.6	2.0	10.0cm
6	Strip Pair	Displaced	0.6	2.0	30.0cm

Table 6.2: Parameters of the iteration steps of the tracking reconstruction in 2012, Run 1 of LHC. σ represents the beam spot size along z axis. From left to right: Seed generation algorithm, target tracks of the iteration, p_T threshold, compatibility with beam spot in the transversal plane (x, y), compatibility with vertex in the longitudinal direction[152].

sions of 2018[6] we find a trigger path used to search Disappearing Tracks signals with MET$>$ 105 GeV and an isolated track with $p_T > 50$ GeV that exhibits some differences with the Run 1 algorithm.

With the additional layers in the Pixel detector, *Pixel Quadruplets* seeding algorithm is used in the first iterations, generating seeds with 4 hits in the BPIX and FPIX. The tracking of the HLT path consists of three iterations: the first two iterations reconstruct tracks with seeds of four pixel hits, being the first one targeting high p_T tracks and the second one low p_T in the full volume of the Pixel detector. The third iteration requires only three pixel hits to its seeds and reconstructs tracks in the neighboring regions of jet candidates (based on information from the calorimeter) and the previous reconstructed tracks.

Due to problems in the Phase-1 Pixel upgrade in 2017 a significant number of pixel modules were inactive, leading to a decrease in the tracking reconstruction performance [153]. Between during the technical stop of the LHC in the end of 2017 the issues were fixed, and in 2018 the detector performance was restored at its expected efficiency. But, to prevent similar problems occurring in the following Runs an additional recovery iteration was added to the HLT tracking system. It required seeds with only two pixel hits in regions where two inactive sensor modules overlapped, taking the interaction point as reference, although due to the limited HLT's CPU processing time a restriction to tracks with $p_T > 1.2$ GeV was set.

[6]The trigger path used for Disappearing Tracks searches was `HLT_MET105_IsoTrk50`, available in several HLT menus in 2018, including in `/online/collisions/2018/2e34/v3.5/HLT/V10`.

6.3.3 Track Reconstruction Efficiency

As mentioned in Subsection 6.3.1 the generated particles are restricted to $|\eta| < 2.5$, to calculate the efficiency of reconstruction constraints on the distance from the interaction point to the center of the beam spot are applied in order to select prompt particles. The efficiencies are defined as the fraction of reconstructed tracks with 75% or more hits correctly assigned, but restricted only to high-purity tracks (tracks that satisfies the tightest requirements on compatibility of the track with the interaction point and the number of detector layers containing hits [126]). CMS's analysis also calculated the fake tracks rate, the fraction of reconstructed high-purity tracks that assigned less than 75% of correct hits, thus not being matched to none of the generated particles. The radial and longitudinal distance thresholds are $< 3\,\text{cm}$ and $< 30\,\text{cm}$ for r and $|z|$ coordinates, respectively. The particles' transverse momentum are also limited to $p_T > 0.9\,\text{GeV}$ for the study of performance as function of η, and $p_T > 0.1\,\text{GeV}$ when studying the efficiency as function of p_T. When considering the performance's dependence on η three fixed p_T samples are considered: $p_T = 1, 10, 100\,\text{GeV}$, while when the dependence is on p_T a flat distribution in $\ln p_T$ is used. A similar criterion was applied in our analysis, Subsection 6.2.1, when matching tracks to $p_T > 10\,\text{GeV}$.

The study we are using as the guideline for comparison investigated the tracking performance of two different categories of samples: isolated particle and pp collisions events, the former containing only one single particle being generated and the latter simulated inclusive $t\bar{t}$ events with and without imposed pileup. A complication of using $t\bar{t}$ events for our comparison is that the Leading-order decay channel $t\bar{t} \to W^+W^-b\bar{b}$, and the further decay of the $W^\pm$ bosons, generates "dirtier" events, containing particles that we are not interested in. Such events perform worse in the final product particles reconstruction, thus we chose not to use them. Since our samples generated only isolated charginos, the comparisons will be made with the isolated particle events. Further, in the paper three particles' samples were studies separately: electrons, muons and charged pions, while we are generating charginos.

Pions are hadrons and interact through elastic and inelastic nuclear interaction with the detectors' material, dispersing the angles of the scattering angles significantly more than the dispersion due to Coulomb scattering only. Being charged also introduces energy loss of the particles as it travels through the volume detector, such as the muon and electron. Electrons, on the other hand, lose a large

fraction of its energy through Bremsstrahlung radiation before reaching the outer layers of the silicon strips, introducing a mechanism of energy loss similar to the nuclear interactions of the charged pions. Furthermore, if the electron induces a magnetic shower or a radiated photon, from the Bremsstrahlung radiation, creates an electron-positron pair, the secondary particles can be detected in the tracker' sensors, creating spurious hits. These factors reduce the reconstruction efficiencies of electrons and pions significantly and increase the fake rate of the reconstructed tracks.

Muons are not affected by the nuclear interactions like the charged pions and lose considerably less energy due to Bremsstrahlung radiation than electrons - since the energy radiated depends inversely on the particle mass and $\frac{m_\mu}{m_e} \sim 200$. Its energy loss is mostly due to Coulomb scattering, ionizing the silicon sensor's medium, and the great majority of muons tends to cross the entire tracker volume, producing several hits in the sensors' layers, thus making its reconstruction efficiency higher than any other charged particle. Considering that the charginos do not interact through nuclear interactions as well, nor lose energy through the electromagnetic interactions such as the electron, we used the muons' analysis to compare with the results we obtained.

The reasons cited above contribute to the high reconstruction efficiency of muons, such that its fake rate in CMS's analysis was negligible. Figure 6.14 shows the efficiencies as function of η and p_T. In both, the high efficiency of reconstruction can be seen, the behavior relative to η shows little difference throughout its range, falling very near the limit of detection $\eta \sim 2.5$, similar to the results we obtained in Figure 6.10. The dependence on p_T also shows coherent results from both analysis (Figures 6.11 and 6.13), lower efficiencies for low p_T values and the increasing behavior until it reaches a stable value near 1.

6.3.4 Tracks' p_T Resolution

Good parameters resolution is required for the proper reconstruction of particles properties, for example for determining a particle mass (p_T resolution), primary vertices of a pp interaction and identify b-quark jets (energy resolution). The paper defines the parameters' resolution through the distribution of *track residuals* (the difference between the reconstructed parameter value and the value of the generated particle) as the half-width of the interval, at each bin, satisfying:

- The width encloses 68% of all entries in the track residuals' distribution,

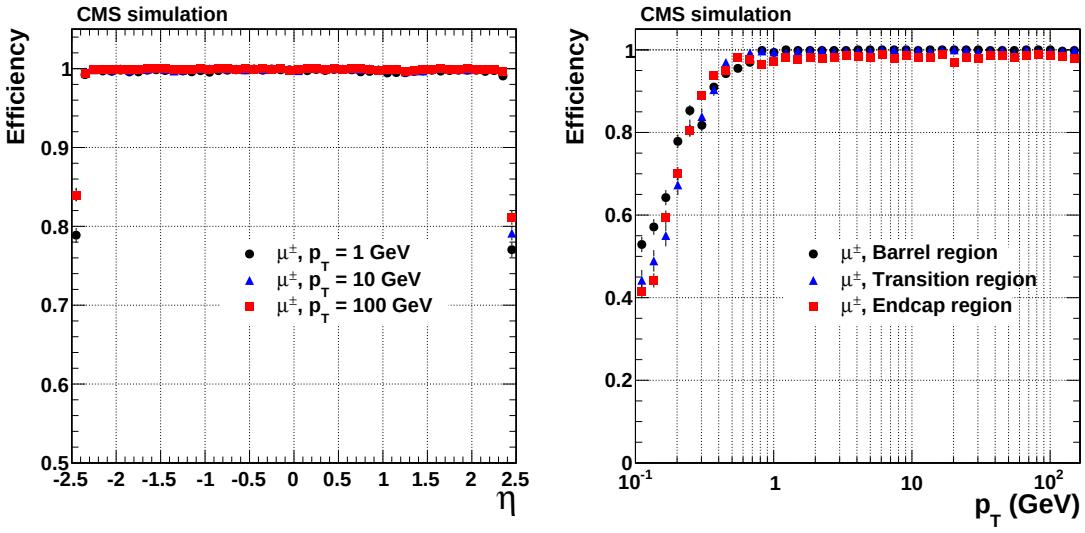

Figure 6.14: Reconstruction efficiencies of high-purity muon tracks. The efficiencies are plotted as function of η (left panel), for fixed $p_T = 1, 10, 100\,\text{GeV}$, and p_T (right panel) for different regions of the tracker: Barrel ($|\eta| < 0.9$), Transition ($0.9 < |\eta| < 1.4$) and Endcap ($1.4 < |\eta| < 2.5$) [126]

- The distribution is fitted with a double-tailed Crystal Ball function at the mode of the distribution.

It was also included in the plots the resolution with the requirement that the half-width contains 90% of the interval entries in order to see the effects of including extreme values in the resolution.

The resolution p_T of single-events muons is shown in Figure 6.15, in the left panel multiple scattering accounts for about 20 to 30% of the resolution for high transverse momentum ($\sim 100\,\text{GeV}$), while for lower values the material in the tracker dominates the resolution. High values of muons' transverse momentum implies in a track trajectory with very small curvature, hindering a precise determination of the momentum. The right panel, showing the behavior of momentum resolution relative to η for fixed momentum, displays again the effect of increasing momentum in the resolution. The bump at $|\eta| \sim 1$ reflects the transition of TOB to the TECs, and the resolution is degraded for higher values of η due to the inferior resolution of the outermost layers of the endcaps compared to the outer barrel ones.

Linking back to our analysis, the p_T resolution was calculated through the distribution of the ratio of track residuals by p_T, Equation 6.1, in each interval of the variables, η and p_T. A gaussian function is fitted in the distribution and the mean value is used as the p_T *Resolution*. For low values of charginos' p_T, $\lesssim 200\,\text{GeV}$,

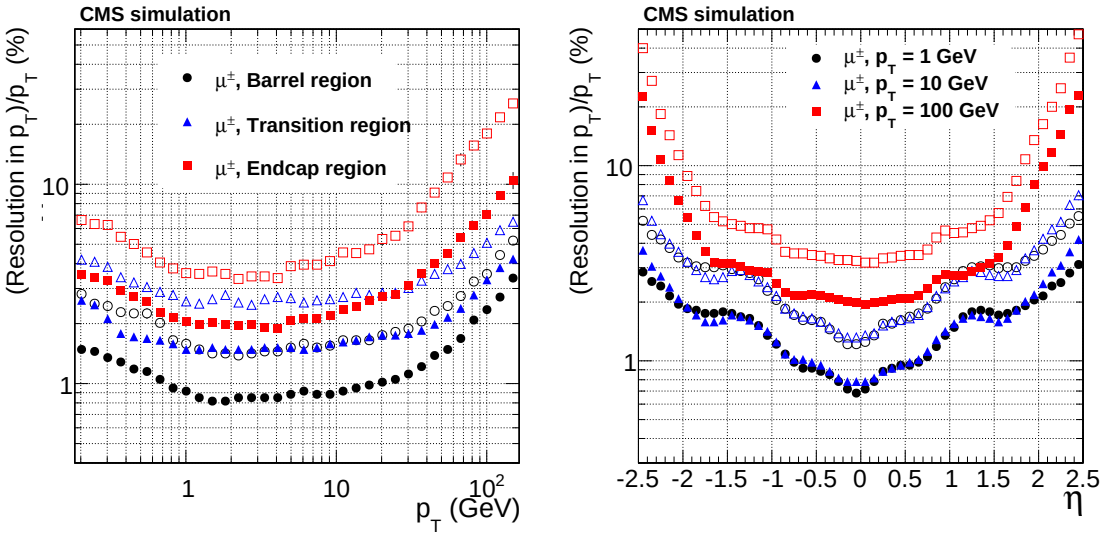

Figure 6.15: Resolution of muon tracks' transverse momentum, the solid symbols represent half-width for 68% intervals and open symbols 90%. The transverse momentum's resolution behavior relative to p_T (left panel) in three regions of the Tracker: Barrel, Transition and Endcap, while the η (right panel) plot shows three fixed momentum samples: 1, 10, 100 GeV.

Figure 6.16 (left panel) shows high values of resolution, probably related to lower Decay Lengths, since with lower transverse momentum the particle will travel less in the tracking before decaying, signaling less silicon layers and thus deteriorate the p_T resolution. In the range of 200 GeV $\lesssim p_T \lesssim$ 1.000 GeV, the resolution is stable at around $\sim 7\%$ before increasing again for higher transverse momentum values, as already discussed before, as the p_T reaches higher values the trajectory approximates a straight line, difficulties a precise p_T reconstruction. This result is in accordance with CMS's analysis, although in average we obtain higher values of the resolution.

In the right panel of Figure 6.16 the resolution is plotted as a function of η. Its behavior is stable is almost all the η range, with p_T resolution $\sim 7\%$, besides an uprising at $|\eta| \sim 2.5$, expected due to the loss of precision of p_T reconstruction near the endcaps of the tracker. A similar behavior is seen in Figure 6.15, showing the agreement between the results. Factors such as the decaying of charginos, fewer statistics to analyze than the article's serving as comparison, a less sophisticated fitting of the p_T resolution contribute to higher values of resolution and more fluctuation. Nevertheless, the behavior of the parameters with the p_T resolution agrees with the observed results of the paper.

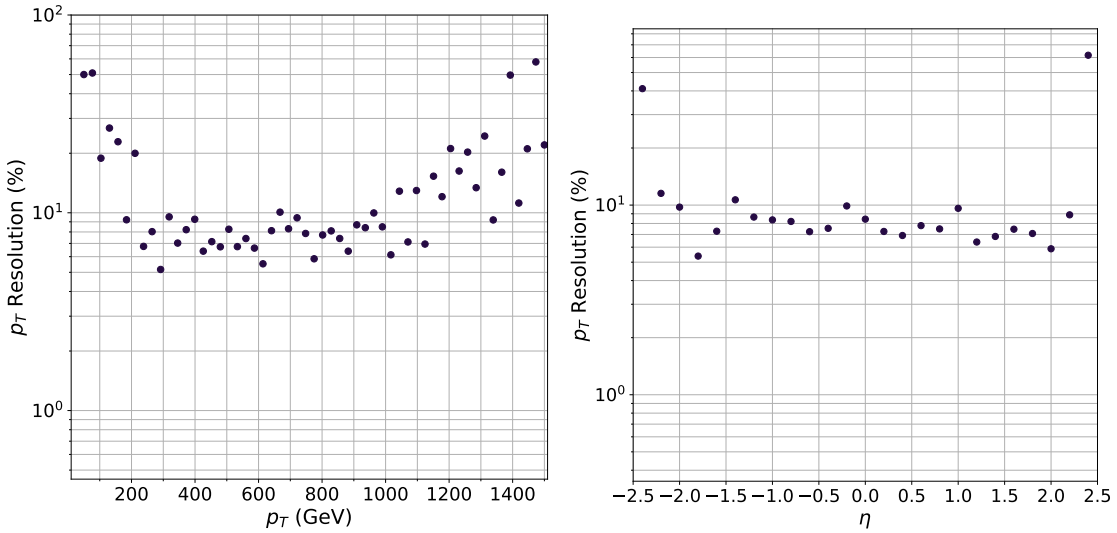

Figure 6.16: Resolution of charginos track's transverse momentum as function of p_T (left panel) and η (right panel). The p_T Resolution is calculated in each interval as the expected value of a gaussian fitting the $\Delta p_T / p_T$ (Equation 6.1) distribution.

Chapter 7

Conclusion

Initially, to understand how the tracking reconstruction is performed, a widely implemented algorithm in the CMS' Tracker System was studied, the Combinatorial Kalman Filter. A toy model detector of 10 concentric, equally spaced layers was considered, events containing 15 $\pi^{\pm}$s were used, and a CKF track reconstruction algorithm was implemented from scratch, resulting in 40% of the tracks of the events being correctly reconstructed by it.

Following the CKF implementation, a study of CMS' reconstruction of possible disappearing tracks was performed through the `CMSSW`'s framework. 10,000 events containing charginos decaying to untracked particles were generated, and the $\tilde{\chi}^{\pm}$'s tracking reconstruction efficiency (the percentage of trackable charginos that were reconstructed correctly) was analyzed. A 70% reconstruction efficiency was obtained, indicating that it may be possible to identify such signals in data from the upcoming Runs of LHC. Background rejection is one of the parameters yet to be analyzed by future avenues of research, as well as investigating other possible signatures of disappearing tracks, involving other BSM particles decaying to SM and DM. Further improving such studies could be one possible way of pioneering detection of dark matter in high energy particle colliders.

Bibliography

[1] S. Weinberg, "The Making of the standard model," *Eur. Phys. J. C*, vol. 34, pp. 5–13, 2004.

[2] E. Dudas, "Top-down Beyond the Standard Model Review," in *48th Rencontres de Moriond on Electroweak Interactions and Unified Theories*, 2013, pp. 427–434.

[3] F. Zwicky, "The redshift of extragalactic nebulae," *Helvetica Physica Acta*, vol. 6, pp. 110–127, 1933.

[4] V. C. Rubin, N. Thonnard, and W. K. Ford, Jr., "Rotational properties of 21 SC galaxies with a large range of luminosities and radii, from NGC 4605 /R = 4kpc/ to UGC 2885 /R = 122 kpc/," *Astrophys. J.*, vol. 238, p. 471, 1980.

[5] M. Markevitch, "Chandra observation of the most interesting cluster in the universe," *ESA Spec. Publ.*, vol. 604, p. 723, 2006.

[6] A. Boveia and C. Doglioni, "Dark Matter Searches at Colliders," *Ann. Rev. Nucl. Part. Sci.*, vol. 68, pp. 429–459, 2018.

[7] G. 't Hooft, "GAUGE THEORIES OF THE FORCES BETWEEN ELEMENTARY PARTICLES," *Sci. Am.*, vol. 242N6, pp. 90–116, 1980.

[8] M. Gell-Mann, "A Schematic Model of Baryons and Mesons," *Phys. Lett.*, vol. 8, pp. 214–215, 1964.

[9] G. Zweig, "An SU(3) model for strong interaction symmetry and its breaking. Version 1," 1 1964.

[10] E. Fermi and C.-N. Yang, "ARE MESONS ELEMENTARY PARTICLES?" *Phys. Rev.*, vol. 76, pp. 1739–1743, 1949.

[11] S. Sakata, "On a Composite Model for the New Particles," *Prog. Theor. Phys.*, vol. 16, pp. 686–688, 1956.

[12] M. Ikeda, S. Ogawa, and Y. Ohnuki, "A Possible Symmetry in Sakata's Model for Bosons-Baryons System," *Prog. Theor. Phys.*, vol. 22, pp. 715–724, 1959.

[13] J. D. Bjorken, "Asymptotic Sum Rules at Infinite Momentum," *Phys. Rev.*, vol. 179, pp. 1547–1553, 1969.

[14] R. P. Feynman, "Very high-energy collisions of hadrons," *Phys. Rev. Lett.*, vol. 23, pp. 1415–1417, 1969.

[15] E. Rutherford, "Collision of α particles with light atoms. IV. An anomalous effect in nitrogen," *Phil. Mag. Ser. 6*, vol. 37, pp. 581–587, 1919.

[16] C.-N. Yang and R. L. Mills, "Conservation of Isotopic Spin and Isotopic Gauge Invariance," *Phys. Rev.*, vol. 96, pp. 191–195, 1954.

[17] P. Z. Skands, "QCD for Collider Physics," in *2010 European School of High Energy Physics*, 4 2011.

[18] S. Weinberg, "A Model of Leptons," *Phys. Rev. Lett.*, vol. 19, pp. 1264–1266, 1967.

[19] S. L. Glashow, "Model of Weak Interactions with CP Violation," *Phys. Rev. Lett.*, vol. 14, pp. 35–38, 1965.

[20] A. Salam, "Weak and Electromagnetic Interactions," *Conf. Proc. C*, vol. 680519, pp. 367–377, 1968.

[21] P. W. Higgs, "Broken Symmetries and the Masses of Gauge Bosons," *Phys. Rev. Lett.*, vol. 13, pp. 508–509, 1964.

[22] S. L. Glashow, "Partial Symmetries of Weak Interactions," *Nucl. Phys.*, vol. 22, pp. 579–588, 1961.

[23] E. Fermi, "An attempt of a theory of beta radiation. 1." *Z. Phys.*, vol. 88, pp. 161–177, 1934.

[24] W. B. Rolnick, *The Fundamental particles and their interactions*, 1994.

[25] E. Noether, "Invariant Variation Problems," *Gott. Nachr.*, vol. 1918, pp. 235–257, 1918.

[26] S. F. Novaes, "Standard model: An Introduction," in *10th Jorge Andre Swieca Summer School: Particle and Fields*, 1 1999, pp. 5–102.

[27] C. Quigg, *GAUGE THEORIES OF THE STRONG, WEAK AND ELECTROMAGNETIC INTERACTIONS*, 1983, vol. 56.

[28] A. Pich, "The Standard Model of Electroweak Interactions," in *2010 European School of High Energy Physics*, 1 2012, pp. 1–50.

[29] Y. Nambu, "Quasiparticles and Gauge Invariance in the Theory of Superconductivity," *Phys. Rev.*, vol. 117, pp. 648–663, 1960.

[30] J. Goldstone, "Field Theories with Superconductor Solutions," *Nuovo Cim.*, vol. 19, pp. 154–164, 1961.

[31] J. Goldstone, A. Salam, and S. Weinberg, "Broken Symmetries," *Phys. Rev.*, vol. 127, pp. 965–970, 1962.

[32] P. A. Zyla *et al.*, "Review of Particle Physics," *PTEP*, vol. 2020, no. 8, p. 083C01, 2020.

[33] G. Aad *et al.*, "The ATLAS Experiment at the CERN Large Hadron Collider," *JINST*, vol. 3, p. S08003, 2008.

[34] S. Chatrchyan *et al.*, "Observation of a New Boson at a Mass of 125 GeV with the CMS Experiment at the LHC," *Phys. Lett. B*, vol. 716, pp. 30–61, 2012.

[35] F. Reines and C. L. Cowan, "Detection of the free neutrino," *Phys. Rev.*, vol. 92, pp. 830–831, 1953.

[36] G. Gamow and M. Schoenberg, "The Possible Role of Neutrinos in Stellar Evolution," *Phys. Rev.*, vol. 58, no. 12, p. 1117, 1940.

[37] ——, "Neutrino Theory of Stellar Collapse," *Phys. Rev.*, vol. 59, no. 7, p. 539, 1941.

[38] C. M. G. Lattes, G. P. S. Occhialini, and C. F. Powell, "Observations on the Tracks of Slow Mesons in Photographic Emulsions. 1," *Nature*, vol. 160, pp. 453–456, 1947.

[39] A. Salam, "On parity conservation and neutrino mass," *Nuovo Cim.*, vol. 5, pp. 299–301, 1957.

[40] T. D. Lee and C. N. Yang, "Many-Body Problem in Quantum Mechanics and Quantum Statistical Mechanics," *Phys. Rev.*, vol. 105, pp. 1119–1120, 1957.

[41] L. D. Landau, "On the conservation laws for weak interactions," *Nucl. Phys.*, vol. 3, pp. 127–131, 1957.

[42] J. Leite Lopes, "A model of the universal fermi interaction," *Nucl. Phys.*, vol. 8, pp. 234–236, 1958.

[43] F. Englert and R. Brout, "Broken Symmetry and the Mass of Gauge Vector Mesons," *Phys. Rev. Lett.*, vol. 13, pp. 321–323, 1964.

[44] T. W. B. Kibble, "Symmetry breaking in nonAbelian gauge theories," *Phys. Rev.*, vol. 155, pp. 1554–1561, 1967.

[45] D. J. Gross and F. Wilczek, "Asymptotically Free Gauge Theories - I," *Phys. Rev. D*, vol. 8, pp. 3633–3652, 1973.

[46] H. Fritzsch, M. Gell-Mann, and H. Leutwyler, "Advantages of the Color Octet Gluon Picture," *Phys. Lett. B*, vol. 47, pp. 365–368, 1973.

[47] J. J. Aubert *et al.*, "Experimental Observation of a Heavy Particle J," *Phys. Rev. Lett.*, vol. 33, pp. 1404–1406, 1974.

[48] J. E. Augustin *et al.*, "Discovery of a Narrow Resonance in e^+e^- Annihilation," *Phys. Rev. Lett.*, vol. 33, pp. 1406–1408, 1974.

[49] M. L. Perl *et al.*, "Evidence for Anomalous Lepton Production in e+ - e- Annihilation," *Phys. Rev. Lett.*, vol. 35, pp. 1489–1492, 1975.

[50] S. W. Herb *et al.*, "Observation of a Dimuon Resonance at 9.5-GeV in 400-GeV Proton-Nucleus Collisions," *Phys. Rev. Lett.*, vol. 39, pp. 252–255, 1977.

[51] D. P. Barber *et al.*, "Discovery of Three Jet Events and a Test of Quantum Chromodynamics at PETRA Energies," *Phys. Rev. Lett.*, vol. 43, p. 830, 1979.

[52] G. Arnison *et al.*, "Experimental Observation of Isolated Large Transverse Energy Electrons with Associated Missing Energy at $\sqrt{s} = 540$ GeV," *Phys. Lett. B*, vol. 122, pp. 103–116, 1983.

[53] ——, "Experimental Observation of Lepton Pairs of Invariant Mass Around 95-GeV/c**2 at the CERN SPS Collider," *Phys. Lett. B*, vol. 126, pp. 398–410, 1983.

[54] R. Stock, "Search for the quark - gluon plasma: The NA35 experiment at the CERN SPS," in *International School of Physics 'Enrico Fermi': Trends in Nuclear Physics*, 1987, pp. 15–33.

[55] P. Yepes *et al.*, "NA36 SETUP AND FIRST RESULTS FROM THE S-32 ION BEAMS," 1987.

[56] G. Graziani, "Measurement of direct CP violation with the NA48 experiment at CERN," Ph.D. dissertation, Florence U., 1999.

[57] G. Brianti, "Large hadron collider in the LEP tunnel," in *6th Topical Workshop on Proton Antiproton Collider Physics*, 1987.

[58] D. Bogert *et al.*, "Determination of the Nucleon Structure Using the Weak Neutral Current," *Phys. Rev. Lett.*, vol. 55, pp. 574–577, 1985.

[59] "The D0 Experiment - Physics at 2 TeV," 10 1983.

[60] J. Orear *et al.*, "Physics at E0 for the 1991 - 92 Collider Run: Fermilab Proposal 811," 3 1990.

[61] S. Abachi *et al.*, "Observation of the top quark," *Phys. Rev. Lett.*, vol. 74, pp. 2632–2637, 1995.

[62] F. Abe *et al.*, "Observation of top quark production in $\bar{p}p$ collisions," *Phys. Rev. Lett.*, vol. 74, pp. 2626–2631, 1995.

[63] A. M. Sirunyan *et al.*, "Combined search for supersymmetry with photons in proton-proton collisions at $\sqrt{s} = 13$ TeV," *Phys. Lett. B*, vol. 801, p. 135183, 2020.

[64] A. Djouadi, "Impact of the SUSY decays on the search for the MSSM Higgs bosons at the LHC," *Mod. Phys. Lett. A*, vol. 14, pp. 359–368, 1999.

[65] J. L. Feng, V. Rentala, and Z. Surujon, "WIMPless Dark Matter in Anomaly-Mediated Supersymmetry Breaking with Hidden QED," *Phys. Rev. D*, vol. 84, p. 095033, 2011.

[66] L. Randall and R. Sundrum, "Out of this world supersymmetry breaking," *Nucl. Phys. B*, vol. 557, pp. 79–118, 1999.

[67] G. F. Giudice, M. A. Luty, H. Murayama, and R. Rattazzi, "Gaugino mass without singlets," *JHEP*, vol. 12, p. 027, 1998.

[68] C. H. Chen, M. Drees, and J. F. Gunion, "A Nonstandard string / SUSY scenario and its phenomenological implications," *Phys. Rev. D*, vol. 55, pp. 330–347, 1997, [Erratum: Phys.Rev.D 60, 039901 (1999)].

[69] G. R. Farrar and P. Fayet, "Phenomenology of the Production, Decay, and Detection of New Hadronic States Associated with Supersymmetry," *Phys. Lett. B*, vol. 76, pp. 575–579, 1978.

[70] G. Bertone and D. Hooper, "History of dark matter," *Rev. Mod. Phys.*, vol. 90, no. 4, p. 045002, 2018.

[71] G. Arcadi, M. Dutra, P. Ghosh, M. Lindner, Y. Mambrini, M. Pierre, S. Profumo, and F. S. Queiroz, "The waning of the WIMP? A review of models, searches, and constraints," *Eur. Phys. J. C*, vol. 78, no. 3, p. 203, 2018.

[72] S. Profumo, L. Giani, and O. F. Piattella, "An Introduction to Particle Dark Matter," *Universe*, vol. 5, no. 10, p. 213, 2019.

[73] D. Akerib, C. Akerlof, D. Y. Akimov, A. Alquahtani, S. Alsum, T. Anderson, N. Angelides, H. Araújo, A. Arbuckle, J. Armstrong *et al.*, "The lux-zeplin (lz) experiment," *Nuclear Instruments and Methods in Physics Research Section A: Accelerators, Spectrometers, Detectors and Associated Equipment*, vol. 953, p. 163047, 2020.

[74] Z. Ahmed, D. Akerib, S. Arrenberg, M. Attisha, C. Bailey, L. Baudis, D. Bauer, J. Beaty, P. Brink, T. Bruch *et al.*, "Search for weakly interacting massive particles with the first five-tower data from the cryogenic dark matter search at the soudan underground laboratory," *Physical Review Letters*, vol. 102, no. 1, p. 011301, 2009.

[75] N. Du, N. Force, R. Khatiwada, E. Lentz, R. Ottens, L. Rosenberg, G. Rybka, G. Carosi, N. Woollett, D. Bowring *et al.*, "Search for invisible axion dark matter with the axion dark matter experiment," *Physical review letters*, vol. 120, no. 15, p. 151301, 2018.

[76] A. Bosma, "21-cm line studies of spiral galaxies. 2. The distribution and kinematics of neutral hydrogen in spiral galaxies of various morphological types." *Astron. J.*, vol. 86, p. 1825, 1981.

[77] E. Athanassoula and A. Bosma, "Shells and rings around galaxies," *Ann. Rev. Astron. Astrophys.*, vol. 23, pp. 147–168, 1985.

[78] J. P. Ostriker and P. J. E. Peebles, "A Numerical Study of the Stability of Flattened Galaxies: or, can Cold Galaxies Survive?" *Astrophys. J.*, vol. 186, pp. 467–480, 1973.

[79] T. S. van Albada, J. N. Bahcall, K. Begeman, and R. Sancisi, "The Distribution of Dark Matter in the Spiral Galaxy NGC-3198," *Astrophys. J.*, vol. 295, pp. 305–313, 1985.

[80] W. Tucker, P. Blanco, S. Rappoport, L. David, D. Fabricant, E. E. Falco, W. Forman, A. Dressler, and M. Ramella, "1e0657-56: a contender for the hottest known cluster of galaxies," *Astrophys. J. Lett.*, vol. 496, p. L5, 1998.

[81] S. Frittelli and E. T. Newman, "An Exact universal gravitational lensing equation," *Phys. Rev. D*, vol. 59, p. 124001, 1999.

[82] J. Wambsganss, "Gravitational lensing in astronomy," *Living Rev. Rel.*, vol. 1, p. 12, 1998.

[83] R. Adam *et al.*, "Planck 2015 results. I. Overview of products and scientific results," *Astron. Astrophys.*, vol. 594, p. A1, 2016.

[84] D. S. Akerib *et al.*, "Results from a search for dark matter in the complete LUX exposure," *Phys. Rev. Lett.*, vol. 118, no. 2, p. 021303, 2017.

[85] E. Aprile *et al.*, "Dark Matter Search Results from a One Ton-Year Exposure of XENON1T," *Phys. Rev. Lett.*, vol. 121, no. 11, p. 111302, 2018.

[86] L. Bergstrom, T. Bringmann, I. Cholis, D. Hooper, and C. Weniger, "New Limits on Dark Matter Annihilation from AMS Cosmic Ray Positron Data," *Phys. Rev. Lett.*, vol. 111, p. 171101, 2013.

[87] N. Aghanim *et al.*, "Planck 2018 results. VI. Cosmological parameters," *Astron. Astrophys.*, vol. 641, p. A6, 2020, [Erratum: Astron.Astrophys. 652, C4 (2021)].

[88] C. L. Bennett *et al.*, "Nine-Year Wilkinson Microwave Anisotropy Probe (WMAP) Observations: Final Maps and Results," *Astrophys. J. Suppl.*, vol. 208, p. 20, 2013.

[89] B. F. Schutz, *A FIRST COURSE IN GENERAL RELATIVITY*. Cambridge, UK: Cambridge Univ. Pr., 1985.

[90] D. N. Spergel *et al.*, "First year Wilkinson Microwave Anisotropy Probe (WMAP) observations: Determination of cosmological parameters," *Astrophys. J. Suppl.*, vol. 148, pp. 175–194, 2003.

[91] Simulations were performed at the National Center for Supercomputer Applications by Andrey Kravtsov (The University of Chicago) and Anatoly Klypin (New Mexico State University). Visualizations by Andrey Kravtsov. http://cosmicweb.uchicago.edu/filaments.html, visited on 02.06.2021.

[92] M. Klasen, M. Pohl, and G. Sigl, "Indirect and direct search for dark matter," *Progress in Particle and Nuclear Physics*, vol. 85, pp. 1–32, 2015.

[93] S. Gentile, "The Alpha Magnetic Spectrometer on the International Space Station," in *28th International Cosmic Ray Conference*, 7 2003, pp. 2145–2148.

[94] C. Meurer, "Dark matter searches with the Fermi Large Area Telescope," *AIP Conf. Proc.*, vol. 1085, no. 1, pp. 719–722, 2009.

[95] E. Aprile *et al.*, "The XENON1T Dark Matter Experiment," *Eur. Phys. J. C*, vol. 77, no. 12, p. 881, 2017.

[96] D. N. McKinsey *et al.*, "The LUX dark matter search," *J. Phys. Conf. Ser.*, vol. 203, p. 012026, 2010.

[97] G. Steigman and M. S. Turner, "Cosmological Constraints on the Properties of Weakly Interacting Massive Particles," *Nucl. Phys. B*, vol. 253, pp. 375–386, 1985.

[98] J. L. Feng and J. Kumar, "The WIMPless Miracle: Dark-Matter Particles without Weak-Scale Masses or Weak Interactions," *Phys. Rev. Lett.*, vol. 101, p. 231301, 2008.

[99] K. Griest and D. Seckel, "Three exceptions in the calculation of relic abundances," *Phys. Rev. D*, vol. 43, pp. 3191–3203, 1991.

[100] P. Gondolo and G. Gelmini, "Cosmic abundances of stable particles: Improved analysis," *Nucl. Phys. B*, vol. 360, pp. 145–179, 1991.

[101] E. W. Kolb and M. S. Turner, *The Early Universe*, 1990, vol. 69.

[102] J. Bernstein, *KINETIC THEORY IN THE EXPANDING UNIVERSE*, ser. Cambridge Monographs on Mathematical Physics. Cambridge, U.K.: Cambridge University Press, 1988.

[103] B. Grządkowski, "Thermal relics from the big bang," Lecture notes, 2009/2010, part of the course *Cosmology: An Introduction to Particle Cosmology* offered by the Institute of Theoretical Physics, University of Warsaw.

[104] S. R. De Groot, *Relativistic Kinetic Theory. Principles and Applications*, W. A. Van Leeuwen and C. G. Van Weert, Eds., 1980.

[105] T. W. B. Kibble, "Topology of Cosmic Domains and Strings," *J. Phys. A*, vol. 9, pp. 1387–1398, 1976.

[106] E. Witten, "Cosmic Separation of Phases," *Phys. Rev. D*, vol. 30, pp. 272–285, 1984.

[107] E. W. Kolb and R. Slansky, "Dimensional Reduction in the Early Universe: Where Have the Massive Particles Gone?" *Phys. Lett. B*, vol. 135, p. 378, 1984.

[108] M. Dine, A. E. Nelson, and Y. Shirman, "Low-energy dynamical supersymmetry breaking simplified," *Phys. Rev. D*, vol. 51, pp. 1362–1370, 1995.

[109] M. Dine, A. E. Nelson, Y. Nir, and Y. Shirman, "New tools for low-energy dynamical supersymmetry breaking," *Phys. Rev. D*, vol. 53, pp. 2658–2669, 1996.

[110] Y. Hochberg, E. Kuflik, T. Volansky, and J. G. Wacker, "Mechanism for Thermal Relic Dark Matter of Strongly Interacting Massive Particles," *Phys. Rev. Lett.*, vol. 113, p. 171301, 2014.

[111] E. Kuflik, M. Perelstein, N. R.-L. Lorier, and Y.-D. Tsai, "Elastically Decoupling Dark Matter," *Phys. Rev. Lett.*, vol. 116, no. 22, p. 221302, 2016.

[112] L. J. Hall, K. Jedamzik, J. March-Russell, and S. M. West, "Freeze-In Production of FIMP Dark Matter," *JHEP*, vol. 03, p. 080, 2010.

[113] G. Bélanger *et al.*, "LHC-friendly minimal freeze-in models," *JHEP*, vol. 02, p. 186, 2019.

[114] O. Buchmueller, M. J. Dolan, S. A. Malik, and C. McCabe, "Characterising dark matter searches at colliders and direct detection experiments: Vector mediators," *JHEP*, vol. 01, p. 037, 2015.

[115] V. Khachatryan *et al.*, "Search for dark matter, extra dimensions, and unparticles in monojet events in proton–proton collisions at $\sqrt{s} = 8$ TeV," *Eur. Phys. J. C*, vol. 75, no. 5, p. 235, 2015.

[116] A. M. Sirunyan *et al.*, "Search for new physics in final states with an energetic jet or a hadronically decaying W or Z boson and transverse momentum imbalance at $\sqrt{s} = 13$ TeV," *Phys. Rev. D*, vol. 97, no. 9, p. 092005, 2018.

[117] ——, "Search for dark matter produced in association with a leptonically decaying Z boson in proton-proton collisions at $\sqrt{s} = 13$ TeV," *Eur. Phys. J. C*, vol. 81, no. 1, p. 13, 2021, [Erratum: Eur.Phys.J.C 81, 333 (2021)].

[118] ——, "Search for new physics in the monophoton final state in proton-proton collisions at $\sqrt{s} = 13$ TeV," *JHEP*, vol. 10, p. 073, 2017.

[119] S. Chatrchyan *et al.*, "The CMS Experiment at the CERN LHC," *JINST*, vol. 3, p. S08004, 2008.

[120] K. Aamodt *et al.*, "The ALICE experiment at the CERN LHC," *JINST*, vol. 3, p. S08002, 2008.

[121] A. A. Alves, Jr. *et al.*, "The LHCb Detector at the LHC," *JINST*, vol. 3, p. S08005, 2008.

[122] D. Barney, "CMS Detector Slice," Jan 2016, cMS Collection. [Online]. Available: https://cds.cern.ch/record/2120661

[123] W. Adam *et al.*, "The CMS Phase-1 Pixel Detector Upgrade," *JINST*, vol. 16, no. 02, p. P02027, 2021.

[124] CMS Collaboration, "`HitPattern` object documentation," 2016, https://github.com/cms-sw/cmssw/blob/CMSSW_9_2_X/DataFormats/TrackReco/interface/HitPattern.h, last accessed in 09.12.2021.

[125] S. Chatrchyan *et al.*, "Alignment of the CMS tracker with LHC and cosmic ray data," *JINST*, vol. 9, p. P06009, 2014.

[126] ——, "Description and performance of track and primary-vertex reconstruction with the CMS tracker," *JINST*, vol. 9, no. 10, p. P10009, 2014.

[127] M. Swartz, "CMS pixel simulations," *Nucl. Instrum. Meth. A*, vol. 511, pp. 88–91, 2003.

[128] "The CMS electromagnetic calorimeter project: Technical Design Report," 1997.

[129] "CMS Technical Design Report for the Phase 1 Upgrade of the Hadron Calorimeter," 9 2012.

[130] S. Abdullin *et al.*, "Design, performance, and calibration of the CMS Hadron-outer calorimeter," *Eur. Phys. J. C*, vol. 57, pp. 653–663, 2008.

[131] M. Albrow, M. Arneodo, V. Avati, J. Baechler, N. Cartiglia, M. Deile, M. Gallinaro, J. Hollar, M. Lo Vetere, K. Oesterberg, N. Turini, J. Varela, D. Wright, and C. CMS-TOTEM, "CMS-TOTEM Precision Proton Spectrometer," Tech. Rep., Sep 2014. [Online]. Available: https://cds.cern.ch/record/1753795

[132] A. M. Sirunyan *et al.*, "Observation of proton-tagged, central (semi)exclusive production of high-mass lepton pairs in pp collisions at 13 TeV with the CMS-TOTEM precision proton spectrometer," *JHEP*, vol. 07, p. 153, 2018.

[133] "The CMS Precision Proton Spectrometer at the HL-LHC – Expression of Interest," 3 2021.

[134] V. A. Khoze, A. D. Martin, and M. G. Ryskin, "Can invisible objects be 'seen' via forward proton detectors at the LHC?" *J. Phys. G*, vol. 44, no. 5, p. 055002, 2017.

[135] V. Khachatryan *et al.*, "The CMS trigger system," *JINST*, vol. 12, no. 01, p. P01020, 2017.

[136] A. Zabi, J. W. Berryhill, E. Perez, and A. D. Tapper, "The Phase-2 Upgrade of the CMS Level-1 Trigger," 2020.

[137] A. M. Sirunyan *et al.*, "Search for disappearing tracks as a signature of new long-lived particles in proton-proton collisions at $\sqrt{s} = 13$ TeV," *JHEP*, vol. 08, p. 016, 2018.

[138] R. E. Kalman, "A new approach to linear filtering and prediction problems," 1960.

[139] L. C. Hun, O. L. Yeng, L. T. Sze, K. V. Chet, and K. Jian, "Kalman filtering and its real-time applications," *Real-time Systems*, 2016.

[140] M. S. Grewal and A. P. Andrews, "Applications of kalman filtering in aerospace 1960 to the present [historical perspectives]," *IEEE Control Systems Magazine*, vol. 30, no. 3, pp. 69–78, 2010.

[141] F.-É. Racicot and R. Théoret, "Forecasting stochastic volatility using the kalman filter: an application to canadian interest rates and price-earnings ratio," *Aestimatio: The IEB International Journal of Finance*, no. 1, pp. 28–47, 2010.

[142] A. Gelb, *Applied optimal estimation*. MIT press, 1974.

[143] A. K. Singh and B. C. Pal, "Chapter 4 - decentralized dynamic estimation using pmus," in *Dynamic Estimation and Control of Power Systems*, A. K. Singh and B. C. Pal, Eds. Academic Press, 2019, pp. 61–91. [Online]. Available: https://www.sciencedirect.com/science/article/pii/B9780128140055000157

[144] A. Becker, "Expectation of variance derivation," https://www.kalmanfilter.net/expectationOfVariance.html, visited on 31.05.2021.

[145] A. Tumasyan *et al.*, "Strategies and performance of the CMS silicon tracker alignment during LHC Run 2," 11 2021.

[146] CMS Collaboration, "CMS Software components." [Online]. Available: https://github.com/cms-sw/cmssw

[147] J. Alwall, R. Frederix, S. Frixione, V. Hirschi, F. Maltoni, O. Mattelaer, H. S. Shao, T. Stelzer, P. Torrielli, and M. Zaro, "The automated computation of tree-level and next-to-leading order differential cross sections, and their matching to parton shower simulations," *JHEP*, vol. 07, p. 079, 2014.

[148] T. Sjöstrand, S. Ask, J. R. Christiansen, R. Corke, N. Desai, P. Ilten, S. Mrenna, S. Prestel, C. O. Rasmussen, and P. Z. Skands, "An introduction to PYTHIA 8.2," *Comput. Phys. Commun.*, vol. 191, pp. 159–177, 2015.

[149] S. Agostinelli *et al.*, "GEANT4–a simulation toolkit," *Nucl. Instrum. Meth. A*, vol. 506, pp. 250–303, 2003.

[150] E. B. Wilson, "Probable inference, the law of succession, and statistical inference," *Journal of the American Statistical Association*, vol. 22, no. 158, pp.

209–212, 1927. [Online]. Available: https://www.tandfonline.com/doi/abs/10.1080/01621459.1927.10502953

[151] T. Sjostrand, S. Mrenna, and P. Z. Skands, "PYTHIA 6.4 Physics and Manual," *JHEP*, vol. 05, p. 026, 2006.

[152] G. Sguazzoni, "Track reconstruction in CMS high luminosity environment," *Nucl. Part. Phys. Proc.*, vol. 273-275, pp. 2497–2499, 2016.

[153] "Tracking Performance in the CMS High Level Trigger - June 2018," Jul 2018. [Online]. Available: https://cds.cern.ch/record/2629370